SOLID STATE PHYSICS

PART III

Magnetic Properties of Solids

M. S. Dresselhaus

Contents

Chapter 1

Review of Topics in Angular Momentum

References

- Sakurai, *Modern Quantum Mechanics*, Chapter 3.

- Schiff, *Quantum Mechanics*, Chapter 7.

- Shankar, *Principles of Quantum Mechanics*, Chapter 12.

- Jackson, *Classical Electrodynamics*, 2nd Ed., Chapter 5.

1.1 Introduction

In this chapter we review some topics in quantum mechanics that we will apply to our discussion of magnetism. The major topic under discussion here is angular momentum.

1.1.1 Angular Momentum, Definitions and Commutation Relations

In classical mechanics, as in quantum mechanics, angular momentum is defined by

$$\vec{L} = \vec{r} \times \vec{p}. \tag{1.1}$$

Since the position operator $\vec{r}$ and momentum operator $\vec{p}$ do not commute, the components of the angular momentum do not commute. We note first that the position and momentum operators do not commute:

$$(x p_x - p_x x) f(\vec{r}) = \frac{\hbar}{i} x \frac{\partial}{\partial x} f(\vec{r}) - \frac{\hbar}{i} \frac{\partial}{\partial x} [x f(\vec{r})] = i\hbar f(\vec{r}). \tag{1.2}$$

The result of Eq. 1.2 is conveniently written in terms of the commutator defined by $[r_j, p_k] \equiv r_j p_k - p_k r_j$ using the relation

$$[r_j, p_k] = i\hbar \delta_{jk}, \tag{1.3}$$

where δ_{jk} is a delta function having the value unity if $j = k$, and zero otherwise. Equation 1.3 says that different components of $\vec{r}$ and $\vec{p}$ commute, and it is only the same components of

$\vec{r}$ and $\vec{p}$ that fail to commute. If we now apply these commutation relations to the angular momentum we get:

$$[L_x, L_y] = L_x L_y - L_y L_x = (y p_z - z p_y)(z p_x - x p_z) - (z p_x - x p_z)(y p_z - z p_y)$$

$$= -i\hbar y p_x + i\hbar x p_y = i\hbar L_z.$$

(1.4)

Similarly, the commutation relations for the other components are:

$$[L_y, L_z] = i\hbar L_x \qquad [L_z, L_x] = i\hbar L_y.$$

(1.5)

The commutation relations in Eqs. 1.4 and 1.5 are conveniently summarized in the symbolic statement

$$\vec{L} \times \vec{L} = i\hbar \vec{L}.$$

(1.6)

These commutation relations are basic to the properties of the angular momentum in quantum mechanics.

Since no two components of the angular momentum commute, it is not possible to find a representation that simultaneously diagonalizes more than one component of $\vec{L}$. That is, there is no wavefunction that is both an eigenfunction of L_x and L_y, for if there were, we could then write

$$L_x \Psi = \ell_x \Psi$$

(1.7)

and

$$L_y \Psi = \ell_y \Psi.$$

(1.8)

Equations 1.7 and 1.8 would then imply that

$$L_x L_y \Psi = L_x \ell_y \Psi = \ell_x \ell_y \Psi$$

(1.9)

and also

$$L_y L_x \Psi = \ell_y \ell_x \Psi$$

(1.10)

so that if L_x and L_y could be diagonalized simultaneously, then L_x and L_y would have to commute. However, we know that they do not commute; therefore, they cannot be simultaneously diagonalized.

On the other hand, all three components of angular momentum, L_x, L_y, and L_z commute with L^2 where

$$L^2 = L_x^2 + L_y^2 + L_z^2.$$

(1.11)

For example

$$\begin{aligned}[L_z, L^2] = & \ L_z L_x^2 - L_x^2 L_z + L_z L_y^2 - L_y^2 L_z \\ = & \ L_x L_z L_x + i\hbar L_y L_x - L_x L_z L_x + i\hbar L_x L_y \\ & + L_y L_z L_y - i\hbar L_x L_y - L_y L_z L_y - i\hbar L_y L_x = 0\end{aligned}$$

(1.12)

and similarly for $[L_x, L^2] = 0$ and $[L_y, L^2] = 0$. Since L_x, L_y and L_z do not commute with each other, it is convenient to select one component (e.g., L_z) as the component that is simultaneously diagonalized with L^2.

2

It is convenient to introduce raising and lowering operators

$$L_{\pm} = L_x \pm iL_y \tag{1.13}$$

so that we can write

$$L^2 = L_z^2 + \frac{1}{2}(L_+L_- + L_-L_+). \tag{1.14}$$

From Eq. 1.13 we know that L_+ and L_- are non-hermitian operators, because L_x and L_y are both Hermitian operators and have real eigenvalues. Since L_x and L_y individually commute with L^2, we have the commutation relations:

$$[L^2, L_+] = 0 \qquad \text{and} \qquad [L^2, L_-] = 0. \tag{1.15}$$

Furthermore, L_+ does not commute with L_z but rather

$$[L_z, L_+] = [L_z, (L_x + iL_y)] = i\hbar(L_y - iL_x) = \hbar L_+ \tag{1.16}$$

and likewise

$$[L_z, L_-] = -\hbar L_-. \tag{1.17}$$

By the same procedure we obtain

$$[L_+, L_-] = [(L_x + iL_y), (L_x - iL_y)] = 2\hbar L_z \tag{1.18}$$

and

$$L_x = \frac{1}{2}(L_+ + L_-) \qquad L_y = -\frac{i}{2}(L_+ - L_-) \tag{1.19}$$

1.1.2 Angular momentum Eigenvalues

We will now use the commutation relations in §1.1.1 to find the eigenvalues of the angular momentum matrices. Let us choose as our representation, one that diagonalizes both L_z and L^2 and we will use quantum numbers m and ℓ to designate the representation. For, example, if Ψ is an eigenfunction of L_z we can write

$$L_z\Psi = m\hbar\Psi \tag{1.20}$$

where the eigenvalue of L_z is $m\hbar$. From Eq. 1.20 we can then write the matrix element of L_z in the $|m\ell\rangle$ representation as

$$\langle m\ell|L_z|m\ell\rangle = m\hbar \tag{1.21}$$

where m is a dimensionless real integer denoting the magnitude of L_z, while ℓ is the maximum value of m and $\hbar$ has the dimension of angular momentum. Physically, we can think of m as telling how many units of angular momentum there are along the z direction. Since L_z has only diagonal matrix elements, the above relation can be written more generally as

$$\langle m'\ell'|L_z|m\ell\rangle = m\hbar\delta_{mm'}\delta_{\ell\ell'}. \tag{1.22}$$

We will now compute the matrix elements of L_+, L_-, and L^2 in the $|m\ell\rangle$ representation.

3

From the commutation relation

$$[L^2, L_+] = 0 \tag{1.23}$$

we obtain

$$\langle m'\ell'|L^2 L_+ - L_+ L^2|m''\ell''\rangle = 0 \tag{1.24}$$

for all $|m\ell\rangle$ states. But L^2 is diagonal in the $|m\ell\rangle$ representation by hypothesis and therefore is specified by some function of ℓ, the quantum number associated with L^2. We thus obtain

$$L^2|m''\ell''\rangle = (L^2)_{\ell''}|m''\ell''\rangle \tag{1.25}$$

where we have written the eigenvalue of the operator L^2 using the notation $(L^2)_{\ell''}$. We will now show that

$$(L^2)_{\ell''} = \hbar^2 \ell''(\ell'' + 1). \tag{1.26}$$

From Eqs. 1.24 and 1.25 we write

$$[(L^2)_{\ell'} - (L^2)_{\ell''}]\langle m'\ell'|L_+|m''\ell''\rangle = 0. \tag{1.27}$$

For Eq. 1.27 to be satisfied, we see that the matrix elements of L_+ must vanish unless $\ell' = \ell''$ which implies that L_+ must be diagonal in ℓ.

The commutation relation $[L_z, L_+] = \hbar L_+$ given by Eq. 1.16 then yields

$$\langle m'\ell|L_z L_+ - L_+ L_z|m''\ell\rangle = \hbar\langle m'\ell|L_+|m''\ell\rangle \tag{1.28}$$

Now exploiting the eigenvalue relation in Eq. 1.22 $L_z|m''\ell\rangle = m''\hbar|m''\ell\rangle$ we get:

$$(m' - m'')\hbar\langle m'\ell|L_+|m''\ell\rangle = \hbar\langle m'\ell|L_+|m''\ell\rangle \tag{1.29}$$

so that $(m' - m'' - 1)\hbar\langle m'\ell|L_+|m''\ell\rangle = 0$ which is conveniently expressed as

$$\hbar\langle m'\ell'|L_+|m''\ell''\rangle = \delta_{\ell'\ell''}\delta_{m',m''+1}\, \lambda_{m'}\hbar \tag{1.30}$$

where $\lambda_{m'}$ is a dimensionless number. Thus, not only are the matrix elements of L_+ in the $|m\ell\rangle$ representation diagonal in ℓ, but they are non-vanishing only on off-diagonal positions of m (that is where the index of m' exceeds the index m'' by unity). The matrix element for L_+ furthermore implies the matrix element of L_- since these matrix elements are related by the Hermitian transpose

$$\langle m'\ell'|L_-|m''\ell''\rangle = \delta_{\ell'\ell''}\delta_{m',m''-1}\lambda_{m'}^*\hbar. \tag{1.31}$$

We can evaluate $\lambda_{m'}$ explicitly by using the commutation relation $[L_+, L_-] = 2\hbar L_z$ from Eq. 1.18, so that in taking matrix elements of $[L_+, L_-]$, we need only consider wholly diagonal matrix elements of

$$\langle m\ell|[L_+, L_-]|m\ell\rangle = 2\hbar m\hbar = 2m\hbar^2 \tag{1.32}$$

because L_z is diagonal in both m and ℓ. Since the matrix element of a product of two operators $\mathcal{O}_1$ and $\mathcal{O}_2$ in general can be written as

$$\langle n|\mathcal{O}_1\mathcal{O}_2|n'\rangle = \Sigma_{n''}\langle n|\mathcal{O}_1|n''\rangle\langle n''|\mathcal{O}_2|n'\rangle \tag{1.33}$$

4

Eq. 1.32 implies a sum over all possible m'' and ℓ'' values. But since L_+ is diagonal in ℓ and has only one non-vanishing matrix element in m, then Eq. 1.32 only has the terms

$$\langle m\ell|L_+|m-1,\ell\rangle\langle m-1,\ell|L_-|m,\ell\rangle - \langle m,\ell|L_-|m+1,\ell\rangle\langle m+1,\ell|L_+|m,\ell\rangle$$

$$= |\lambda_{m-1}|^2\hbar^2 - |\lambda_m|^2\hbar^2 = 2m\hbar^2 \tag{1.34}$$

which has a solution

$$|\lambda_m|^2 = -m(m+1) \tag{1.35}$$

so that $-(m-1)m + m(m+1) = 2m$ is satisfied. Clearly we can add any constant C to the solution of Eq. 1.34 and obtain another equally valid solution

$$|\lambda_m|^2 = C - m(m+1). \tag{1.36}$$

Since $|\lambda_m|^2$ is positive, definite, we require that C be chosen to guarantee that requirement. This means that m must be restricted to the range from $-\ell$ to $+\ell$ and $C = \ell(\ell+1)$ or

$$|\lambda_m|^2 = \ell(\ell+1) - m(m+1). \tag{1.37}$$

This then means that the raising operator acts on the state $|m,\ell\rangle$ to produce a state $|m+1,\ell\rangle$

$$L_+|m,\ell\rangle = \hbar\lambda_{m+1}|m+1,\ell\rangle. \tag{1.38}$$

Starting with the lowest state $m = -\ell$, the raising operator L_+ produces a physical state until $m = \ell$ is reached at which time $L_+|\ell,\ell\rangle$ produces a non-existent or null state.

With these restrictions on possible values of m, we can evaluate the matrix element of L^2 in the m,ℓ representation:

$$\langle m,\ell|L^2|m,\ell\rangle = \langle m,\ell|\tfrac{1}{2}(L_+L_- + L_-L_+) + L_z^2|m,\ell\rangle$$

$$= \left[\tfrac{1}{2}(\ell(\ell+1) - (m-1)m) + \tfrac{1}{2}\left(\ell(\ell+1) - m(m+1)\right) + m^2\right]\hbar^2 \tag{1.39}$$

$$= \ell(\ell+1)\hbar^2$$

and from Eq. 1.38 we can write

$$\langle m+1,\ell|L_+|m,\ell\rangle = \hbar|\lambda_m| = \hbar\sqrt{\ell(\ell+1) - m(m+1)} \equiv \hbar\sqrt{(\ell-m)(\ell+m+1)} \tag{1.40}$$

which also implies

$$\langle m-1,\ell|L_-|m,\ell\rangle = \hbar\sqrt{(\ell+m)(\ell-m+1)}. \tag{1.41}$$

The restrictions on the values of m are thus:

1. The raising operator L_+ raises the m index by 1, while the lowering operator L_- lowers m by 1.

2. The difference between the minimum and maximum values of m must be an integer. This condition requires that ℓ be either integral or half-integral. Orbital angular momentum always involves integral values of ℓ and spin angular momentum may involve either half-integral or integral values of the unit of angular momentum $\hbar$.

In matrix form, the matrix elements of L_z are:

$$L_z = \begin{pmatrix} \ell & 0 & 0 & \dots & 0 \\ 0 & \ell-1 & 0 & \dots & 0 \\ 0 & 0 & \ell-2 & \dots & 0 \\ \vdots & \vdots & \vdots & \vdots & \vdots \\ 0 & 0 & 0 & \dots & -\ell \end{pmatrix} \tag{1.42}$$

For L_+ we have only off-diagonal elements to the right of the diagonal. We will give here some matrix elements for specific values of ℓ. For half integral spin $s = 1/2$ we have

$$S_x = \hbar/2 \begin{pmatrix} 0 & 1 \\ 1 & 0 \end{pmatrix}, \qquad S_y = \hbar/2 \begin{pmatrix} 0 & -i \\ i & 0 \end{pmatrix}, \qquad S_z = \hbar/2 \begin{pmatrix} 1 & 0 \\ 0 & -1 \end{pmatrix} \tag{1.43}$$

and

$$S_+ = \hbar \begin{pmatrix} 0 & 1 \\ 0 & 0 \end{pmatrix}, \qquad S_- = \hbar \begin{pmatrix} 0 & 0 \\ 1 & 0 \end{pmatrix}, \qquad S^2 = 3\hbar^2/4 \begin{pmatrix} 1 & 0 \\ 0 & 1 \end{pmatrix} \tag{1.44}$$

(Note: We use ℓ to denote orbital angular momentum where $\ell =$ integer and we use s when discussing half-integral values of angular momentum.) The four matrices

$$\begin{pmatrix} 1 & 0 \\ 0 & 1 \end{pmatrix}, \qquad \begin{pmatrix} 0 & 1 \\ 1 & 0 \end{pmatrix}, \qquad \begin{pmatrix} 0 & -1 \\ 1 & 0 \end{pmatrix}, \qquad \begin{pmatrix} 1 & 0 \\ 0 & -1 \end{pmatrix} \tag{1.45}$$

span the vector space and can be used to expand any arbitrary (2×2) matrix. Similarly, we can write the matrices for $\ell = 1$ as

$$L_x = \frac{\hbar}{\sqrt{2}} \begin{pmatrix} 0 & 1 & 0 \\ 1 & 0 & 1 \\ 0 & 1 & 0 \end{pmatrix} \tag{1.46}$$

$$L_y = \frac{\hbar}{\sqrt{2}} \begin{pmatrix} 0 & -i & 0 \\ i & 0 & -i \\ 0 & i & 0 \end{pmatrix} \tag{1.47}$$

$$L_z = \hbar \begin{pmatrix} 1 & 0 & 0 \\ 0 & 0 & 0 \\ 0 & 0 & -1 \end{pmatrix} \tag{1.48}$$

$$L_+ = \hbar \begin{pmatrix} 0 & \sqrt{2} & 0 \\ 0 & 0 & \sqrt{2} \\ 0 & 0 & 0 \end{pmatrix} \tag{1.49}$$

$$L_- = \hbar \begin{pmatrix} 0 & 0 & 0 \\ \sqrt{2} & 0 & 0 \\ 0 & \sqrt{2} & 0 \end{pmatrix} \tag{1.50}$$

$$L^2 = 2\hbar^2 \begin{pmatrix} 1 & 0 & 0 \\ 0 & 1 & 0 \\ 0 & 0 & 1 \end{pmatrix}. \tag{1.51}$$

6
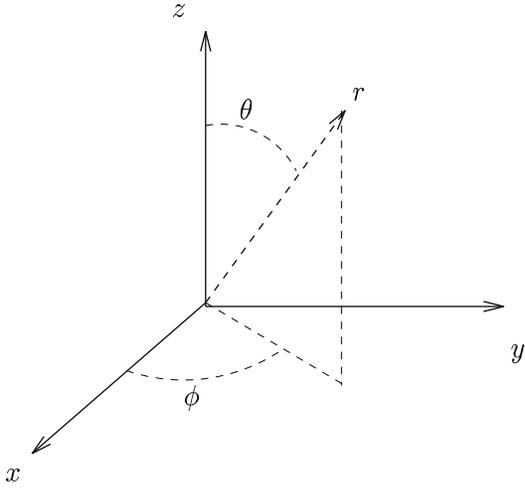
Figure 1.1: Cartesian and polar coordinate system used in wave mechanics.

The matrix element expressions

$$\langle m\ell|L^2|m'\ell'\rangle = \delta_{\ell,\ell'}\,\delta_{m,m'}\,\ell(\ell+1)\hbar^2, \tag{1.52}$$

$$\langle m\ell|L_z|m'\ell'\rangle = \delta_{\ell,\ell'}\,\delta_{m,m'}\,m\hbar, \tag{1.53}$$

$$\langle m\ell|L_+|m'\ell'\rangle = \delta_{\ell,\ell'}\,\delta_{m,m'+1}\,\sqrt{(\ell-m')(\ell+m'+1)}, \tag{1.54}$$

and

$$\langle m\ell|L_-|m'\ell'\rangle = \delta_{\ell,\ell'}\,\delta_{m,m'-1}\,\sqrt{(\ell+m')(\ell-m'+1)} \tag{1.55}$$

allow us to write explicit matrices for the angular momentum operators for all ℓ values.

1.2 Angular Momentum in Wave Mechanics

By definition

$$L_x = yp_z - zp_y = \frac{\hbar}{i}\left[y\left(\frac{\partial}{\partial z}\right) - z\left(\frac{\partial}{\partial y}\right)\right] \tag{1.56}$$

$$L_y = zp_x - xp_z = \frac{\hbar}{i}\left[z\left(\frac{\partial}{\partial x}\right) - x\left(\frac{\partial}{\partial z}\right)\right] \tag{1.57}$$

$$L_z = xp_y - yp_x = \frac{\hbar}{i}\left[x\left(\frac{\partial}{\partial y}\right) - y\left(\frac{\partial}{\partial x}\right)\right] \tag{1.58}$$

Using polar coordinates shown in Fig. 1.1, we can write

$$x = r\cos\phi\sin\theta \qquad y = r\sin\phi\sin\theta \qquad z = r\cos\theta. \tag{1.59}$$

In spherical coordinates, the components of the angular momentum become

$$L_x = i\hbar\left[\sin\phi\left(\frac{\partial}{\partial\theta}\right) + \cot\theta\cos\phi\left(\frac{\partial}{\partial\phi}\right)\right] \tag{1.60}$$

$$L_y = i\hbar\left[-\cos\phi\left(\frac{\partial}{\partial\theta}\right) + \cot\theta\sin\phi\left(\frac{\partial}{\partial\phi}\right)\right] \tag{1.61}$$

$$L_z = \frac{\hbar}{i}\left(\frac{\partial}{\partial\phi}\right) \tag{1.62}$$

and

$$L^2 = L_x^2 + L_y^2 + L_z^2 = -\hbar^2\left[\frac{1}{\sin\theta}\frac{\partial}{\partial\theta}\left(\sin\theta\frac{\partial}{\partial\phi}\right) + \frac{1}{\sin^2\theta}\left(\frac{\partial^2}{\partial\phi^2}\right)\right]. \tag{1.63}$$

In wave mechanics, the eigenfunctions of L_z and L^2 are the spherical harmonics $Y_{\ell m}(\theta,\phi)$:

$$L^2 Y_{\ell m}(\theta,\phi) = \ell(\ell+1)\hbar^2 Y_{\ell m}(\theta,\phi) \tag{1.64}$$

and

$$L_z Y_{\ell m}(\theta,\phi) = m\hbar Y_{\ell m}(\theta,\phi) \tag{1.65}$$

where the spherical harmonics are explicitly given by

$$Y_{\ell m}(\theta,\phi) = \left[\left(\frac{(2\ell+1)}{4\pi}\frac{(\ell-|m|)!}{(\ell+|m|)!}\right)\right]^{1/2} P_\ell^m(\cos\theta)e^{im\phi} \tag{1.66}$$

in which the associated Legendre functions $P_\ell^m(\cos\theta)$ are

$$P_\ell^m(w) = (1-w^2)^{(1/2)|m|}\ \frac{d^{|m|}P_\ell(w)}{dw^{|m|}} \tag{1.67}$$

where $w = \cos\theta$ and the Legendre functions are found from the generating functions

$$\sum_{\ell=0}^{\infty} P_\ell(w)s^\ell = \frac{1}{\sqrt{1-2sw+s^2}} \qquad \text{for} \quad s < 1. \tag{1.68}$$

From Eq. 1.68 it follows that

$$P_0(w)=1$$

$$P_1(w)=w = \cos\theta \tag{1.69}$$

$$P_2(w)=\tfrac{1}{2}(3w^2 - 1) = \tfrac{1}{2}(3\cos^2\theta - 1).$$

Thus, the first few spherical harmonics are:

$$Y_{0,0} = \sqrt{\frac{1}{4\pi}} \tag{1.70}$$

$$Y_{1,1} = \sqrt{\frac{3}{8\pi}}\sin\theta e^{i\phi} \tag{1.71}$$

$$Y_{1,0} = \sqrt{\frac{3}{4\pi}}\cos\theta \tag{1.72}$$

$$Y_{1,-1} = \sqrt{\frac{3}{8\pi}}\sin\theta e^{-i\phi}. \tag{1.73}$$

8

The matrix elements of angular momentum can also be calculated from the point of view of wave mechanics. In that case we must perform the angular integrations which define the matrix element for an operator $\mathcal{O}$:

$$\int_0^\pi d\phi \int_0^{2\pi} \sin\theta \; d\theta \; Y_{\ell m}^*(\theta,\phi) \; \mathcal{O} \; Y_{\ell' m'}(\theta,\phi) \equiv \langle \ell m | \mathcal{O} | \ell' m' \rangle. \tag{1.74}$$

In general, the matrix mechanics approach to angular momentum is the easier technique for the evaluation of matrix elements. For example we have from Eq. 1.54 the result for the raising operator

$$L_+ Y_{\ell m}(\theta,\phi) = \sqrt{(\ell - m)(\ell + m + 1)} \; \hbar Y_{\ell,m+1}(\theta,\phi). \tag{1.75}$$

1.3   Magnetic Moment and Orbital Angular Momentum

In this section we show that there is a magnetic moment $\vec{\mu}$ associated with the orbital angular momentum $\vec{L}$ given by

$$\vec{\mu} = \left(\frac{e}{2mc}\right)\vec{L} \tag{1.76}$$

where $e = -4.8 \times 10^{-10}$ esu $= -1.6 \times 10^{-19}$ Coulombs of charge. It is for this reason that a discussion of the magnetic properties of solids requires knowledge of the quantum mechanical properties of the angular momentum.

There are various derivations of the result given by Eq. 1.76 which follows from classical electromagnetic theory. By definition, the magnetic moment associated with a charge distribution $\rho_{\text{charge}}(\vec{r}, t)$ is: (see Jackson, pp 181)

$$\vec{\mu} \equiv \frac{1}{2c} \int d^3 r \; \rho_{\text{charge}}(\vec{r} \times \vec{v}). \tag{1.77}$$

The factor $(\vec{r} \times \vec{v})$ in the above definition suggests that $\vec{\mu}$ is related to the orbital angular momentum $\vec{L}$ which is defined for a mass distribution $\rho_{\text{mass}}(\vec{r}, t)$ as

$$\vec{L} = \int d^3 r \, \rho_{\text{mass}} \; (\vec{r} \times \vec{v}). \tag{1.78}$$

For simple systems, the mass and charge densities are proportional:

$$\rho_{\text{mass}}/m = \rho_{\text{charge}}/q = \frac{1}{\text{Volume}} \tag{1.79}$$

where m is in units of mass and q is in units of charge for the electron. Therefore we can write for a simple electron system

$$\vec{\mu} = \left(\frac{q}{2mc}\right)\vec{L} = \left(\frac{e}{2mc}\right)\vec{L}. \tag{1.80}$$

See Eisberg Ch. 11 for another derivation of this result.

It is usually convenient to introduce a special symbol for the magnetic moment of an electron, namely the Bohr magneton μ_B which is defined as

$$\mu_B \equiv e\hbar/2mc = -0.927 \times 10^{-20} \text{ erg/gauss} \tag{1.81}$$

9

and μ_B is a negative number since e is negative. Thus

$$\vec{\mu} = \frac{\mu_B \vec{L}}{\hbar} = \frac{g_\ell \mu_B \vec{L}}{\hbar} \tag{1.82}$$

where we note that the angular momentum is measured in units of $\hbar$. Equation 1.82 defines the g–factor as it relates $\vec{\mu}$ and the angular momentum and we note that the g–factor for orbital motion is $g_\ell = 1$. Remember that since μ_B is a negative number for electrons, the magnetic moment of the electron is directed antiparallel to the orbital angular momentum.

1.4   Spin Angular Momentum

The existence of spin angular momentum is based on several experimental observations:

1. The Stern–Gerlach atomic beam experiment shows that there could be an even number of possible m values

$$m = -\ell, -\ell+1, -\ell+2, \cdots, \ell \tag{1.83}$$

    which implies that ℓ can have a half-integral value.

2. The observation that associated with the spin angular momentum is a magnetic moment

$$\vec{\mu} = g_s \mu_B \vec{S}/\hbar \tag{1.84}$$

    where $\vec{\mu}$ and $\vec{S}$ are oppositely directed. However in Eq. 1.84 the g_s value for the spin is not unity but is very nearly $g_s = 2$. For spectroscopy, the Lamb shift correction is needed whereby $g_s = 2.0023$. Electron spin resonance experiments typically yield g-values to 5 or more significant figures.

3. There is evidence for spin in atomic spectra.

   Like the orbital angular momentum, the spin angular momentum obeys the commutation relations

$$\vec{S} \times \vec{S} = i\hbar\vec{S} \tag{1.85}$$

and consequently we have the matrix elements of the spin operators in the $|s, m_s\rangle$ representation:

$$\langle m'_s s' | S^2 | m_s s \rangle = \hbar^2 s(s+1)\, \delta_{s,s'}\, \delta_{m_s, m'_s} \tag{1.86}$$

$$\langle m'_s s' | S_z | m_s s \rangle = \hbar m_s \delta_{s,s'}\, \delta_{m_s, m'_s} \tag{1.87}$$

$$\langle m'_s s' | S_+ | m_s s \rangle = \hbar\sqrt{(s-m_s)(s+m_s+1)}\ \delta_{s,s'}\, \delta_{m_s+1, m'_s} \tag{1.88}$$

$$\langle m'_s s' | S_- | m_s s \rangle = \hbar\sqrt{(s+m_s)(s-m_s+1)}\ \delta_{s,s'}\, \delta_{m_s-1, m'_s}. \tag{1.89}$$

A single electron has a spin angular momentum $S_z = \hbar/2$ so that there are two possible m_s values, namely $m_s = \pm 1/2$ and also $s(s+1) = (1/2)(3/2) = 3/4$.

1.5 The Spin-Orbit Interaction

An electron in an atomic state having orbital angular momentum $\vec{L}$ and spin angular momentum $\vec{S}$ can have its spin angular momentum coupled to the orbital angular momentum through the so-called spin-orbit interaction. The physical basis for this interaction is as follows. Because of the orbital motion of the electrons, a magnetic field $\vec{H}$ is created. Now this magnetic field acts on the magnetic moment associated with the electron spin and attempts to line up the moment along the magnetic field giving an interaction energy

$$\mathcal{H}'_{s-o} = -\vec{\mu} \cdot \vec{H}. \tag{1.90}$$

We will give here a simple classical argument for the magnitude of the spin-orbit interaction and refer you to Eisberg Ch. 11 for a more complete derivation.

Since we wish to focus our attention on the electron and the magnetic field it sees, we choose a coordination system attached to the electron. In this coordinate system, the nucleus is moving, thereby generating at the position of the electron both an electric field $\vec{E} = e\vec{r}/r^3$ and a magnetic field $\vec{H} = -(\vec{v}/c) \times \vec{E}$. We thus find the interaction energy

$$\mathcal{H}'_{s-o} = -\vec{\mu} \cdot \vec{H} = -\left[-\frac{|e|}{mc}\vec{S}\right] \cdot \left[-\frac{\vec{v}}{c} \times \vec{E}\right]. \tag{1.91}$$

In a solid, we replace $\vec{E} = \vec{\nabla}V(r)/|e|$ where $V(r)$ is the Coulomb potential energy in the solid; in an atomic system, $V(r)$ becomes $U(r)$ and $\vec{\nabla}U(r)$ becomes $f(r)\vec{r}$ where $f(r)$ is a scalar function. We thus obtain for atomic systems

$$\mathcal{H}'_{s-o} = \frac{f(r)}{mc^2}[\vec{S} \cdot (\vec{r} \times \vec{v})] = \frac{f(r)}{m^2c^2}(\vec{L} \cdot \vec{S}). \tag{1.92}$$

For the special case of a simple Coulomb potential $U(r) = -e^2/r$,

$$\vec{\nabla}U = (e^2/r^3)\vec{r} \tag{1.93}$$

or

$$f(r) = e^2/r^3 \tag{1.94}$$

and

$$\mathcal{H}'_{s-o} = \frac{e^2}{(m^2c^2r^3)}\vec{S} \cdot \vec{L}. \tag{1.95}$$

The more correct derivation given in Eisberg shows that

$$\mathcal{H}'_{s-o} = \frac{e^2}{(2m^2c^2r^3)}\vec{S} \cdot \vec{L} \tag{1.96}$$

where the factor of 2 inserted in Eq. 1.96 is due to relativistic corrections. For more general atomic systems the spin-orbit interaction is written as

$$\mathcal{H}'_{s-o} = \xi(r)\vec{S} \cdot \vec{L} \tag{1.97}$$

and for solids where no central force approximation is made, we then have

$$\mathcal{H}'_{s-o} = \frac{1}{2m^2c^2}[\vec{\nabla}V \times \vec{p}] \cdot \vec{S} \tag{1.98}$$

where $V(\vec{r})$ is the periodic potential in the solid.

1.5.1 Solution of Schrödinger's Equation for Free Atoms

We will now study the effect of the spin-orbit interaction on atomic spectra. The one-electron atomic problem in a central force Coulomb field is written as the Schrödinger equation

$$\left[\frac{p^2}{2m} + U(r)\right]\Psi = E\Psi \tag{1.99}$$

(without spin) or in wave mechanics (spherical coordinates) Eq. 1.99 becomes

$$-\frac{\hbar^2}{2m}\left[\frac{1}{r^2}\frac{\partial}{\partial r}\, r^2\frac{\partial}{\partial r} + \frac{1}{r^2\sin^2\theta}\left(\frac{\partial^2}{\partial\phi^2}\right) + \frac{1}{r^2\sin\theta}\left(\frac{\partial}{\partial\theta}\right)\left(\sin\theta\,\frac{\partial}{\partial\theta}\right)\right]\Psi + U(r)\Psi = E\Psi. \tag{1.100}$$

It is clear that if the potential is spherically symmetric, the separation of variables leads to an eigenvalue problem in L^2, or writing

$$\Psi(r,\theta,\phi) = R(r)\, Y_{\ell m}(\theta,\phi) \tag{1.101}$$

we get for the radial equation

$$\left\{\frac{1}{r^2}\frac{d}{dr}\left(r^2\frac{d}{dr}\right) + \left[-\frac{\ell(\ell+1)}{r^2} + \frac{2m}{\hbar}\left(E - U(r)\right)\right]\right\}R(r) = 0 \tag{1.102}$$

where m is the mass and the angular equation is written in terms of the spherical harmonics $Y_{\ell m}(\theta,\phi)$. Thus each atomic state is (without spin) characterized by a principal quantum number n and a quantum number ℓ denoting the orbital angular momentum states. By inspection of the differential equation (Eq. 1.102), the quantum number m does not enter so that every solution to a one-electron atomic problem must be $(2\ell + 1)$-fold degenerate or degenerate in the quantum number m. We can also understand this result physically. For a spherically symmetric system there is no preferred direction. Thus, there can be no difference in energy arising from the component of $\vec{L}$ taken along any particular direction.

The solutions for $\ell = 0$ of the atomic problem where $U(r) = -e^2/r$ gives the Bohr energy levels for the hydrogen atom

$$E_n = -\frac{me^4}{2\hbar^2 n^2} \qquad n = 1, 2, 3, 4, \ldots. \tag{1.103}$$

Since the angular momentum term in the radial equation $-\ell(\ell+1)/r^2$ has the opposite sign from the potential term $-U(\vec{r})$, higher ℓ states will lie higher in energy. A physical way to see this is to think of the angular momentum as giving rise to an increase in kinetic energy and hence less binding. For a general attractive potential $U(\vec{r})$ the classification of the atomic levels is as shown in Fig. 1.2.

We have reviewed this background in order to show that the spin-orbit interaction

$$\mathcal{H}'_{\text{s-o}} = \xi(r)\vec{L}\cdot\vec{S} \tag{1.104}$$

serves to lift certain degeneracies. To calculate the effect of the spin-orbit interaction we introduce the total angular momentum $\vec{J}$ which is defined by

$$\vec{J} \equiv \vec{L} + \vec{S}. \tag{1.105}$$

If no torques are acting on the atomic system, then the total angular momentum is conserved and the magnitude of $\vec{J}$ (or J^2) is a constant of the motion. We can thus find for atomic systems where $U = U(\vec{r})$ various constants of the motion:
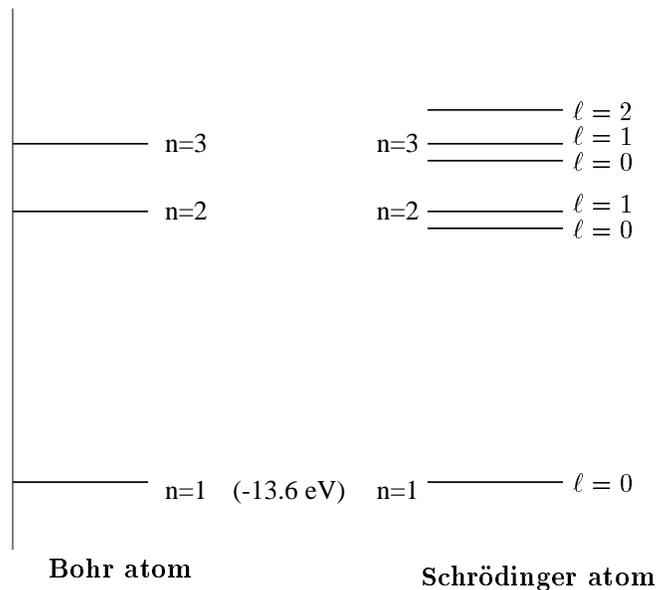
Figure 1.2: Energy levels in the Bohr atom and the Schrödinger solution showing the orbital degeneracy.

1. the energy E giving rise to the principal quantum number n

2. the magnitude of L^2 giving rise to quantum number ℓ

3. the z component (or any other single component) of $\vec{L}$ giving rise to quantum number m_ℓ. The energy levels do not depend on m_ℓ.

4. the magnitude of S^2 giving rise to quantum number s. In the absence of the spin-orbit interaction the energy levels do not depend on the spin.

Since no preferred direction in space is introduced by the spin-orbit interaction, each level is $(2\ell + 1)(2s + 1)$-fold degenerate.

At this point it is profitable to point out the difference between the various possible representations, which will be denoted here by their quantum numbers:

1. no spin: n, ℓ, m_ℓ

2. with spin but no spin-orbit interaction: n, ℓ, s, m_ℓ, m_s

Here each atomic level is $(2s+1)(2\ell + 1)$-fold degenerate but since $s = 1/2$ we have each level $2(2\ell + 1)$-fold degenerate. Having specified m_ℓ and m_s, then m_j is determined by the relation:

$$m_j = m_\ell + m_s \tag{1.106}$$

which follows from the vector relation $\vec{J} = \vec{L} + \vec{S}$ taken along the z direction of quantization. Having specified ℓ gives two possible values for j

$$j = \ell + s = \ell + \frac{1}{2} \tag{1.107}$$

or

$$j = \ell - s = \ell - \frac{1}{2} \tag{1.108}$$

13

Now let us count up the degeneracy from the point of view of the j-values: m_j can have $(2j + 1)$ values for $j = \ell + 1/2$ or $(2\ell + 1) + 1$ values and m_j can have $(2j + 1)$ values for $j = \ell - 1/2$ or $(2\ell - 1) + 1$. Therefore the total number of states is $[2\ell + 2] + [2\ell] = 4\ell + 2 = 2(2\ell + 1)$ so that the degeneracy of the states is the same whether we count states in the $|n, \ell, s, m_\ell, m_s\rangle$ representation or in the $|n, \ell, s, j, m_j\rangle$ representation.

Although (without spin-orbit interaction) the <u>energy</u> is the same for the two representations, the <u>states</u> are not the same. Suppose we take $m_\ell = 1$ and $m_s = -1/2$ to give $m_j = 1/2$. This does not tell us which j, m_j state we have: that is we can have either $j = 3/2$ or $j = 1/2$, for in either case $m_j = 1/2$ is an acceptable quantum number. Thus to go from the (m_ℓ, m_s) representation to the (j, m_j) representation we must make linear combinations of states. That is, the (m_ℓ, m_s) combination $(1,-1/2)$ contributes to both the (j, m_j) states $(3/2,1/2)$ and $(1/2,1/2)$.

If we now introduce the spin-orbit interaction, then not only are the <u>states</u> that contribute to (j, m_j) different but a splitting is introduced into the energy of the states, depending of the value of j. That is, the energy for the $j = 1/2$ levels (2-fold degenerate) will be different than that for the $j = 3/2$ levels (4-fold degenerate). The fact that this splitting occurs in this way is a consequence of symmetry (group theory) and has nothing to do with whether $\mathcal{H}'_{s-o}$ is small or large, or whether we use perturbation theory or not.

To show that this splitting does occur we will evaluate $\vec{L} \cdot \vec{S}$ in the j, m_j representation (remembering that ℓ and s are still "good" quantum numbers). We note that if we consider

$$\vec{J} = \vec{L} + \vec{S} \tag{1.109}$$

and square Eq. 1.109, we obtain the following operator equation:

$$J^2 = (\vec{L} + \vec{S}) \cdot (\vec{L} + \vec{S}) = L^2 + S^2 + 2\vec{L} \cdot \vec{S} \tag{1.110}$$

since $\vec{L}$ and $\vec{S}$ commute. The spin and orbital angular momenta commute because they operate in different vector spaces. Thus we obtain

$$\vec{L} \cdot \vec{S} = \frac{1}{2}(J^2 - L^2 - S^2). \tag{1.111}$$

If we now take the diagonal matrix element, we get:

$$\langle jm_j|\vec{L} \cdot \vec{S}|jm_j\rangle = \frac{1}{2}\langle jm_j|J^2 - L^2 - S^2|jm_j\rangle = \frac{\hbar^2}{2}\left[j(j+1) - \ell(\ell+1) - s(s+1)\right]. \tag{1.112}$$

If we consider, for example, the case of $\ell = 1, s = 1/2$, we get

$$\langle jm_j|\vec{L} \cdot \vec{S}|jm_j\rangle = \hbar^2/2 \quad \text{for} \quad j = 3/2 \tag{1.113}$$

and

$$\langle jm_j|\vec{L} \cdot \vec{S}|jm_j\rangle = -\hbar^2 \quad \text{for} \quad j = 1/2. \tag{1.114}$$

Thus, the spin-orbit interaction lifts the degeneracy of the atomic states (see Fig. 1.3), though the center of gravity is maintained. The magnitude of the splitting depends on the matrix element of $\xi(r)$ between states with principal quantum number n.

Similarly, if we have $\ell = 2$ and $s = 1/2$ we will find a splitting into a $j = 5/2$ and a $j = 3/2$ state; the center of gravity of the levels will be maintained. If we should have

14
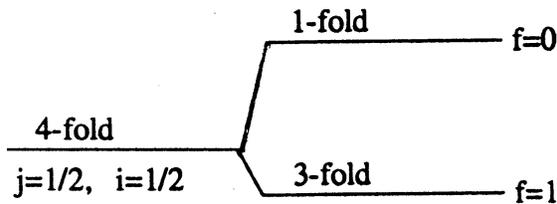
Figure 1.3: Schematic of the spin-orbit splitting of the p-state, $\ell = 1$.

$s = 1$ (as might occur in a multi-electron atom) and $\ell = 1$, then we can make states with $j = 2$, 1, 0. In this case, the spin-orbit interaction will produce a splitting into three levels of degeneracies 5, 3 and 1 to yield a total of nine states which is the number we started with $(2\ell + 1)(2s + 1) = 9$.

We would now like to consider the magnetic moment of an electron in an atom (see §1.3), taking into account the contribution from both the orbital and spin angular momenta. Of particular interest here is the fact that although the g–factor for the orbital contribution is $g_\ell = 1$, that for the spin contribution is $g_s = 2$. What this means is that the magnetic moment $\vec{\mu} = (e/2mc)(\vec{L} + 2\vec{S})$ due to both the orbital and spin contributions is <u>not</u> directed along the total angular momentum $\vec{J}$. As a consequence, we cannot simultaneously diagonalize the magnetic moment operator $\vec{\mu}$ and the total angular momentum $\vec{J}$. We will now discuss two ways to calculate matrix elements of $\vec{\mu}$. The first is called the vector model for angular momentum which gives the diagonal matrix elements, while the second is the Clebsch–Gordan coefficients, which gives both diagonal and off-diagonal matrix elements.

1.6   Vector Model for Angular Momentum

In this section we develop a method to find the expectation value of an operator which is itself a function of angular momentum operators, but cannot be directly diagonalized. The magnetic moment operator is an example of such an operator.

Because of the coupling between the orbital and spin angular momentum, the components L_z and S_z have no definite values. The spin-orbit interaction takes a state specified by the quantum numbers ℓ and s, and splits it into levels according to their j values. So if we have $\ell = 1$ and $s = 1/2$ in the absence of the spin-orbit interaction, then we get a $j = 3/2$ level and a $j = 1/2$ level when the spin-orbit interaction is considered. For the $j = 3/2$ level we have the four states $m_j = 3/2, 1/2, -1/2, -3/2$ and for the $j = 1/2$ level we have the two states $m_j = 1/2$ and –1/2. Since the $m_j = 1/2$ state can arise from either an $m_\ell = 1$ and $m_s = -1/2$ state or an $m_\ell = 0$ and $m_s = 1/2$ state, the specifications of m_ℓ and m_s do not uniquely specify the energy, or to say it another way, the state with quantum numbers $|\ell, s, m_\ell, m_s\rangle = |1, 1/2, 1, -1/2\rangle$ has no definite energy. On the other hand, the state $|\ell, s, j, m_j\rangle$ does have a definite energy and is thus an eigenstate of the energy while $|\ell, s, m_\ell, m_s\rangle$ is <u>not</u> an eigenstate in the presence of the spin-orbit interaction.

The various angular momenta are often represented in terms of a vector diagram as shown in Fig. 1.4. Since there are no external torques acting on the system, the total angular momentum $\vec{J}$ is a constant of the motion. In the absence of any external perturbation on the free atom, we are free to choose the z direction however we wish. If, however, a magnetic

15
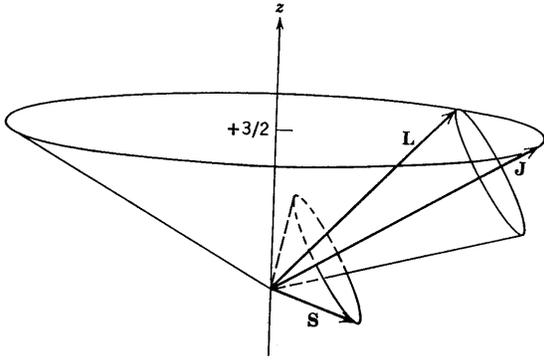
Figure 1.4: This vector diagram for the angular momentum was constructed for: $\ell = 2, s = 1/2, j = 5/2, m_j = 3/2$ and shows that the total angular momentum $\vec{J}$ precesses around the z–axis. On the other hand, the angular momenta $\vec{S}$ and $\vec{L}$ precess around $\vec{J}$.

field is present, there is a preferred direction in space and the z direction is conventionally taken along the direction of the external magnetic field. The projection of $\vec{J}$ on the z axis, J_z, can be diagonalized along with the total Hamiltonian so that we can represent $\vec{J}$ on the diagram above by a definite vector with respect to the z axis. The length of the vector $|\vec{J}|$ is $\hbar\sqrt{j(j+1)}$ and its projection J_z on the diagram in Fig. 1.4 is $(3/2)\hbar$. (Actually for $j = 5/2$ we could have selected five other projections $m_j = 5/2, 1/2, -1/2, -3/2, -5/2$.) Thus the angle between $\vec{J}$ and J_z in Fig. 1.4 is given by

$$\cos\theta = \frac{J_z}{|J|} = \frac{3/2}{\sqrt{(5/2)(7/2)}} = \frac{3}{\sqrt{35}}. \tag{1.115}$$

Now the magnitudes of the vectors $\vec{L}$ and $\vec{S}$ are fixed at

$$|\vec{L}| = \hbar\sqrt{\ell(\ell+1)} = \hbar\sqrt{6} \tag{1.116}$$

and

$$|\vec{S}| = \hbar\sqrt{s(s+1)} = \frac{\hbar}{2}\sqrt{3}. \tag{1.117}$$

However, the direction of these vectors in space is not fixed and this fact is illustrated in Fig. 1.4 as a freedom of precession of the vectors $\vec{L}$ and $\vec{S}$ about $\vec{J}$ such that only their lengths are fixed. We note that $\vec{L}$ and $\vec{S}$ have equal probabilities of being in any particular direction along the precessional path and consequently a projection of $\vec{L}$ or $\vec{S}$ on the z axis would give different values depending on the position along this precessional path. For this reason L_z and S_z do not yield good quantum numbers.

From the diagram, we see that the projections of $\vec{L}$ and $\vec{S}$ on $\vec{J}$ have definite values. Thus, the vector diagram tells us that if we want to find the expectation value of the orbital angular momentum $\vec{L}$ along any direction in space, we project $\vec{L}$ on $\vec{J}$ and then project the resulting vector on the special direction of quantization z. Thus to calculate the expectation value of L_z we find using the vector model:

$$\langle \ell, s, j, m_j | L_z | \ell, s, j, m_j \rangle = \langle \ell, s, j, m_j | \frac{\vec{L} \cdot \vec{J}}{|\vec{J}|^2} (J_z) | \ell, s, j, m_j \rangle. \tag{1.118}$$

16

In the $\langle \ell, s, j, m_j \rangle$ representation, we can readily calculate the diagonal matrix elements of J_z and J^2

$$\langle \ell, s, j, m_j | J_z | \ell, s, j, m_j \rangle = \hbar m_j \tag{1.119}$$

$$\langle \ell, s, j, m_j | J^2 | \ell, s, j, m_j \rangle = \hbar^2 j(j+1). \tag{1.120}$$

To find $\langle \ell, s, j, m_j | \vec{L} \cdot \vec{J} | \ell, s, j, m_j \rangle$ we observe that

$$\vec{S} = \vec{J} - \vec{L} \quad \text{and} \quad S^2 = J^2 + L^2 - 2\vec{L} \cdot \vec{J} \tag{1.121}$$

so that

$$\langle \ell, s, j, m_j | \vec{L} \cdot \vec{J} | \ell, s, j, m_j \rangle = \langle \ell, s, j, m_j | \tfrac{1}{2}(J^2 + L^2 - S^2) | \ell, s, j, m_j \rangle$$

$$= \tfrac{\hbar}{2} \left[j(j+1) + \ell(\ell+1) - s(s+1) \right] \tag{1.122}$$

so for $\ell = 2, s = 1/2, j = 5/2, m_j = 3/2$ we get upon substitution into Eq. 1.122

$$\left\langle \ell, s, j, m_j \left| \frac{|\vec{L} \cdot \vec{J}|}{J^2}(J_z) \right| \ell, s, j, m_j \right\rangle = \hbar \frac{6}{5}. \tag{1.123}$$

The vector model is of great importance in considering the expectation value of vectors which are functions of the angular momentum. Thus the magnetic moment operator $\vec{\mu}_{\text{total}}$ is

$$\vec{\mu}_{\text{total}} = \frac{\mu_B}{\hbar}(g_\ell \vec{L} + g_s \vec{S}) = \frac{\mu_B}{\hbar}(\vec{L} + 2\vec{S}) \tag{1.124}$$

and the magnetic moment is directed along the vector $\vec{L} + 2\vec{S}$. This magnetic moment vector is not along $\vec{J}$ and therefore has no definite value when projected on an arbitrary direction in space such as the z–axis. On the other hand, the projection of $\vec{\mu}_{\text{total}}$ on $\vec{J}$ has a definite value. It is convenient to write Eq. 1.124 as

$$\vec{\mu}_{\text{total}} = \frac{\mu_B}{\hbar}(g\vec{J}) \tag{1.125}$$

so that the energy of an electron in a magnetic field $\vec{B}$ is

$$E = -\vec{\mu}_{\text{total}} \cdot \vec{B} = -\mu_B(Bg m_j) \tag{1.126}$$

where the Landé g–factor g represents the projection of $\vec{\mu}_{\text{total}}$ on $\vec{J}$ so that

$$g = \left\langle \ell, s, j, m_j \left| \frac{(\vec{L} + 2\vec{S}) \cdot \vec{J}}{J^2} \right| \ell, s, j, m_j \right\rangle. \tag{1.127}$$

To evaluate g we note that

$$(\vec{L} + 2\vec{S}) \cdot \vec{J} = (\vec{L} + 2\vec{S}) \cdot (\vec{L} + \vec{S}) = L^2 + 3\vec{L} \cdot \vec{S} + 2S^2 \tag{1.128}$$

but

$$\vec{J} = \vec{L} + \vec{S} \tag{1.129}$$

and

$$J^2 = (\vec{L} + \vec{S})^2 = L^2 + S^2 + 2\vec{L} \cdot \vec{S} \tag{1.130}$$

17
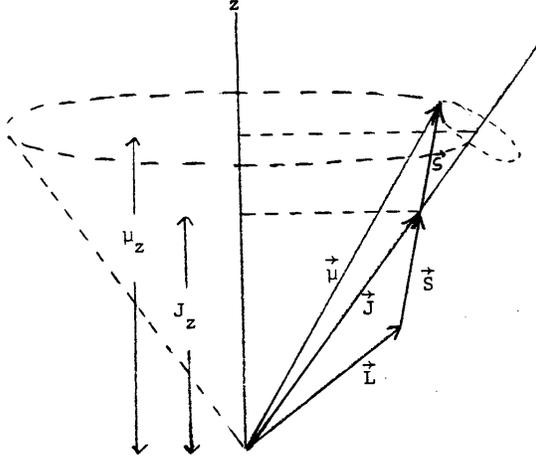
Figure 1.5: The vector model for the magnetic moment operator $\vec{\mu}$. Here we see that $\vec{J}$ precesses around z but J_z is fixed. $\vec{S}$ precesses around $\vec{J}$ and the projection of $\vec{S}$ on $\vec{J}$ is fixed. The projection of $\vec{\mu}$ on $\vec{J}$ is fixed as is the projection of $(\vec{\mu} \cdot \vec{J})\, \vec{J}$ on the z axis. Thus the vector model provides a prescription for finding the expectation value of the magnetic moment operator $\vec{\mu}$.

so that

$$\vec{L} \cdot \vec{S} = \frac{1}{2}(J^2 - L^2 - S^2). \tag{1.131}$$

Thus

$$(\vec{L} + 2\vec{S}) \cdot \vec{J} = L^2 + \frac{3}{2}(J^2 - L^2 - S^2) + 2S^2 = \frac{3}{2}J^2 - \frac{1}{2}L^2 + \frac{1}{2}S^2. \tag{1.132}$$

We now take diagonal matrix elements of Eq. 1.132 in the $|\ell, s, j, m_j\rangle$ representation and find for the Landé g–factor

$$g = \frac{[\frac{3}{2}j(j+1) + \frac{1}{2}s(s+1) - \frac{1}{2}\ell(\ell+1)]}{j(j+1)}. \tag{1.133}$$

Thus using the vector model, we have found the diagonal matrix elements of the magnetic moment operator. In §2.4 we will show how to also find the off–diagonal matrix elements of the angular momentum operator using the Clebsch–Gordan coefficients and using raising and lowering operators.

18

Chapter 2

Magnetic Effects in Free Atoms

2.1 The Zeeman Effect

Suppose we now impose a small magnetic field on our atomic system. The magnetic moment $\vec{\mu}$ will try to line up along the magnetic field $\vec{B}$ yielding an interaction Hamiltonian

$$\mathcal{H}'_Z = -\vec{\mu} \cdot \vec{B}. \tag{2.1}$$

We will see below that the effect of a magnetic field is to lift the $(2j+1)$ degeneracy of the angular momentum states and this effect is called the Zeeman effect. We denote the perturbation Hamiltonian in Eq. 2.1 associated with the Zeeman effect by $\mathcal{H}'_Z$.

To evaluate the matrix elements of Eq. 2.1, we choose the z direction along the magnetic field. Then evaluation of $\mathcal{H}'_Z$ in the $|\ell, s, j, m_j\rangle$ representation yields

$$\langle \ell, s, j, m_j | \mathcal{H}'_Z | \ell, s, j, m_j \rangle = -\mu_B g B \langle \ell, s, j, m_j | J_z | \ell, s, j, m_j \rangle \tag{2.2}$$

following the discussion of the vector model in §1.6. As an illustration, take $j = 5/2$, and from Eq. 2.2 we find that the magnetic field will split the zero field level into $(2j+1) = 6$ equally spaced levels, the level spacing being proportional to $(\mu_B g B)$ and thus proportional to the magnetic field. What we mean by a small magnetic field in Eq. 2.1 is that $\mathcal{H}'_Z = -\vec{\mu} \cdot \vec{B}$ has an expectation value that is small compared with the spin-orbit interaction, i.e., $\mathcal{H}'_Z \ll \mathcal{H}'_{so}$. In this limit the Zeeman problem must be solved in the $|\ell, s, j, m_j\rangle$ representation.

If, on the other hand, the expectation value of the $\mathcal{H}'_Z = -\vec{\mu} \cdot \vec{B}$ interaction is large compared with the spin-orbit interaction, then we solve the problem in the $|\ell, s, m_\ell, m_s\rangle$ representation and consider the spin-orbit interaction as a perturbation. In the $|\ell, s, m_\ell, m_s\rangle$ representation, $\vec{\mu} \cdot \vec{B}$ is readily evaluated from Eq. 1.126

$$\langle \ell, s, m_\ell, m_s | \mathcal{H}'_Z | \ell, s, m_\ell, m_s \rangle = -\mu_B \langle \ell, s, m_\ell, m_s | L_z + 2S_z | \ell, s, m_\ell, m_s \rangle / \hbar$$

$$= -\mu_B B (m_\ell + 2m_s). \tag{2.3}$$

In this case there will be a degeneracy in some of the states in Eq. 2.3 and this degeneracy is lifted by the spin-orbit interaction, which now acts as a perturbation on the Zeeman effect. For intermediate field values where the Zeeman energy and the spin–orbit interaction are of comparable magnitudes, the problem is more difficult to solve (see Schiff, chapter 12).

2.2 The Hyperfine Interaction

Closely related to the spin-orbit interaction is the hyperfine interaction. This interaction, though too small to be important for many solid state applications, is of great importance in nuclear magnetic resonance and Mössbauer spectroscopy studies. The hyperfine interaction arises through the interaction of the magnetic moment of the nucleus with the magnetic field produced by the electrons. Just as we introduce the magnetic moment of the free electron as (see Eq. 1.84)

$$\vec{\mu}_{\text{spin}} = \frac{g_s e}{2mc}\vec{S},\tag{2.4}$$

where $g_s = 2$, we introduce the nuclear magnetic moment

$$\vec{\mu}_{\text{spin-nucleus}} = \frac{g_I \mu_N \vec{I}}{\hbar}\tag{2.5}$$

where the g–factor for the nucleus g_I is constant for a particular nucleus and $\vec{I}$ is the angular momentum of the nucleus. Values of g_I are tabulated in handbooks. For nuclei, g_I can be of either sign. If g_I is positive, then the magnetic moment and spin are lined up; otherwise they are antiparallel as for electrons. The nuclear magneton μ_N is defined as a positive number:

$$\mu_N = \frac{|e|\hbar}{2Mc} = \frac{m}{M}|\mu_B| = \frac{\mu_B}{1836} \sim 5 \times 10^{-24} \text{ ergs/gauss}\tag{2.6}$$

where M is the mass of the proton, so that the hyperfine interaction between the nuclear orbital motion and the nuclear spin is much smaller than the spin-orbit interaction. The magnetic field produced by the electrons at the nuclear position is denoted by $\vec{B}_J$ and will be proportional to $\vec{J}$ or more specifically to

$$\left(\frac{\vec{B}_J \cdot \vec{J}}{J^2}\right)\vec{J}.\tag{2.7}$$

Thus, the hyperfine interaction $\mathcal{H}'_{hf}$ will be of the form $\mathcal{H}'_{hf} = -\vec{\mu}_{\text{spin-nucleus}} \cdot \vec{B}_J$ so that from Eqs. 2.5 and 2.7 we obtain

$$\mathcal{H}'_{hf} = -\text{constant}(\vec{I} \cdot \vec{J}).\tag{2.8}$$

To the extent that the $\mathcal{H}'_{hf}$ interaction is significant in magnitude, neither m_i nor m_j are good quantum numbers, and we must therefore introduce a new <u>total</u> angular momentum $\vec{F}$ which is the sum of the nuclear and electronic angular momenta

$$\vec{F} = \vec{I} + \vec{J}\tag{2.9}$$

so that

$$\vec{F} \cdot \vec{F} = (\vec{I} + \vec{J}) \cdot (\vec{I} + \vec{J})\tag{2.10}$$

and in the representation $|i, j, f, m_f\rangle$ we can evaluate $\vec{I} \cdot \vec{J}$ to obtain

$$\vec{I} \cdot \vec{J} = \frac{1}{2}[f(f+1) - i(i+1) - j(j+1)].\tag{2.11}$$

The presence of this hyperfine interaction lifts some of the $(2i+1)(2j+1)$ degeneracy of the f states. For example let $j = 1/2$, $i = 1/2$, then $f = 0, 1$ and we have $\vec{I} \cdot \vec{J} = 1$ or 0. Thus the hyperfine interaction splits the 4-fold degenerate level into a 3–fold $f = 1$ triplet level and a non–degenerate $f = 0$ singlet level as shown in Fig. 2.1.
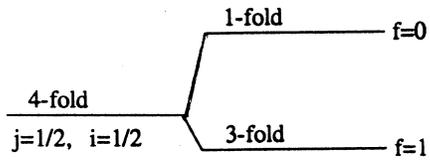
Figure 2.1: Schematic diagram of the splitting of the 4–fold $j = 1/2, i = 1/2$ level under the hyperfine interaction between the nuclear spin and the orbital magnetic field. The level ordering for the hyperfine interaction may be opposite to that for the spin-orbit interaction, since the nuclear g–factor can be either positive or negative.

2.3 Addition of Angular Momenta

We have until now considered the addition of angular momentum in terms of $(\vec{L} + \vec{S})$ for a single electron and $(\vec{J} + \vec{I})$ for the case of the nuclear spin angular momentum. In this section we consider the addition of orbital angular momenta associated with more than one electron. For example, for two electrons $\vec{L}$ could be written as $\vec{L}_1 + \vec{L}_2$. The addition of the angular momentum $\vec{L}_i$ for each electron to obtain a total orbital angular momentum $\vec{L}$ occurs in most atomic systems where we have more than one electron. We will consider here the case of L-S (Russell–Saunders) coupling which is the more important case for atomic systems and for solids. According to the L-S coupling scheme we combine the orbital angular momenta for all the electrons

$$\vec{L} = \Sigma_i \vec{L}_i \tag{2.12}$$

and all the spin angular momenta

$$\vec{S} = \Sigma_i \vec{S}_i \tag{2.13}$$

and then, from the total $\vec{L}$ and the total $\vec{S}$, we form a total $\vec{J} = \vec{L} + \vec{S}$. The representation that we use for finding the matrix elements for J is $|\ell, s, j, m_j\rangle$ where the quantum numbers correspond to the total $\vec{L}$, total $\vec{S}$ and $\vec{J} = \vec{L} + \vec{S}$. Our discussion of the magnetic properties of solids most often uses this representation.

In the following subsection (§2.3.1), we will give some examples of multi-electron systems. First we will find the lowest energy state or the ground state for a many-electron system. To find the lowest energy state we use Hund's rule.

2.3.1 Hund's Rule

Hund's Rule is used to find the ground state s, ℓ and j values for a multi-electron atom and provides a recipe to find the $s, \ell,$ and j values for the ground state. The rules are applied in the following sequence:

1. The ground state has the maximum multiplicity $(2s+1)$ allowed by the Pauli Principle, which determines $\vec{S}$.

2. The ground state has the maximum $\vec{L}$ consistent with the multiplicity in $\vec{S}$ given by Hund's Rule (1).

$(2s + 1)$
multiplicity $\searrow$

$^2\text{F}_{5/2}$

total ℓ value
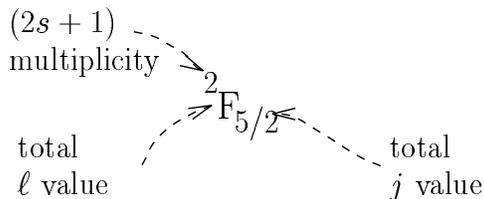
total j value

Figure 2.2: The notation used to specify the quantum numbers s, ℓ, j for an atomic configuration, which for the $^2\text{F}_{5/2}$ level is $s = 1/2$, $\ell = 3$, and $j = 5/2$.

3. The total $\vec{J}$ value is $|\vec{L} - \vec{S}|$ if the shell is less than half full and $|\vec{L} + \vec{S}|$ if the shell is more than half full.

The physical origin of the first Hund's rule is that to minimize the Coulomb repulsion between two electrons it is advantageous to keep them apart, and by selecting the same spin state, the two electrons are required to have different orbital states by the exclusion principle. The spin-orbit interaction which gives rise to the lowering of the ground state is proportional to $\xi(\vec{r})\vec{L} \cdot \vec{S}$ (see §1.5). Thus the lowest energy state is expected to occur when L and S have their maximum values in accordance with the Pauli principle. Finally, $\xi(\vec{r})$ tends to be positive for less than half filled shells and negative for more than half filled shells. Thus $\vec{J}$ in the ground state tends to be a minimum $J = |L - S|$ when the shell is less than half full and a maximum $J = |L + S|$ when the shell is more than half full.

The notation used to specify a state (s, ℓ, j) is shown in Fig. 2.2 for the state: $s = 1/2$, $\ell = 3$, and $j = 5/2$, where the multiplicity $(2s + 1)$ is given as the left hand superscript, ℓ is given by a Roman capital letter and j is given as the right hand subscript. The notation for the total L value is historic and listed here:

$$
\begin{array}{lll}
L = 0 & \text{S} & \text{(Sharp)} \\
L = 1 & \text{P} & \text{(Paschen)} \\
L = 2 & \text{D} & \text{(Diffuse)} \\
L = 3 & \text{F} & \\
L = 4 & \text{G} & \\
L = 5 & \text{H} & \\
L = 6 & \text{I} & \\
L = 7 & \text{K} & \\
\text{etc.} & &
\end{array}
$$

Let us illustrate Hund's rule with a few examples.

- one 4f electron in Ce^{3+}
  This simple configuration is for a single $4f$ electron for which $\ell = 3$. We have then $\ell = 3$, and $s = 1/2$. Hund's Rules (1) and (2) above are already satisfied. Rule (3) gives $\vec{J} = |\vec{L} - \vec{S}|$ or $j = 5/2$ so we have the result that the ground state of a $4f$ electronic configuration is $^2F_{5/2}$. The g–factor using Eq. 1.133 becomes

$$
g = \frac{\frac{3}{2}(\frac{35}{4}) - \frac{3}{2}(4) + \frac{3}{8}}{\frac{35}{4}} = \frac{15}{2} \tag{2.14}
$$

Table 2.1: The $s = 1$ level is 3-fold degenerate and has $m_s = 1, 0, -1$, while the $s = 0$ level is non–degenerate and can only have $m_s = 0$.

m_{s_1}	m_{s_2}	m_s
1/2	1/2	1
1/2	−1/2	0
−1/2	1/2	0
−1/2	−1/2	−1

- the configuration $(4f)^2$ in Pr^{3+}

  For this configuration we have two $4f$ electrons. Applying Hund's Rule (1), the maximum $\vec{S}$ we can have is obtained by taking $(m_s)_{\text{total}} = 1/2 + 1/2 = 1$ so that $s = 1$, thus giving a multiplicity $2s + 1 = 3$. But then we cannot take both electrons with $m_\ell = 3$ because, if we did, we would violate the Pauli principle. Thus the highest ℓ value we can make is to take $m_{\ell_1 \text{max}} = 3$ and $m_{\ell_2 \text{max}} = 2$. Thus $m_{\ell_{\text{total,max}}} = 5$ so that Hund's Rule (2) gives $\ell = 5$ which, from our table above, is an H state. Application of Rule (3) is made for two electrons filling a shell that can hold $2(2 \cdot 3 + 1) = 14$ electrons so that we are still less than half full. The j-value is then found as $(\ell - s)$ and is $j = 5 - 1 = 4$ so that our configuration gives a ground state $^3H_4$ and a Landé g–factor from Eq. 1.133

$$g = \frac{\frac{3}{2}(4)(5) - \frac{1}{2}(5)(6) + \frac{1}{2}(1)(2)}{(4)(5)} = \frac{4}{5}. \tag{2.15}$$

  For homework you will have practice in applying Hund's rule to a different electronic configuration.

2.3.2 Electronic Configurations

It is also useful to find all the states that emerge from a particular electronic configuration, such as $nd\, n'p$. For example, for the $3d4p$ this two-electron configuration we have one d-electron ($\ell = 2$) and one p-electron ($\ell = 1$). Applying Hund's Rule (1) tells us that the $s_{\text{total}} = 1$ configuration will lie lower in energy than the $s_{\text{total}} = 0$ configuration. Taking $s_1 = 1/2$ and $s_2 = 1/2$ we can only have s_{total} values of 0 or 1 as shown in Table 2.1, and there is no way to make an $s_{\text{total}} = 1/2$. Now for the ℓ_{total} we can make a state with $\ell = 3$ (state of lowest energy by Hund's Rule (2)). But as shown in Table 2.2 we can also make states with $\ell = 2$ and $\ell = 1$. In this table is listed the number of ways that a given m_ℓ value can be obtained. For example, $m_\ell = 1$ can be formed by: (1) $m_{\ell_1} = 2$, $m_{\ell_2} = -1$; (2) $m_{\ell_1} = 1$, $m_{\ell_2} = 0$; and (3) $m_{\ell_1} = 0$, $m_{\ell_2} = 1$.

Since the shells for the two electron configuration $ndn'p$ are less than half-full, the j value with lowest energy is $|\ell - s|$. For $s = 0$, we immediately have $j = \ell$ and no spin-orbit splitting results. For $s = 1$, we have three possible j-values: $\ell + 1, \ell, \ell - 1$.

We show below that the number of states is invariant whether we consider the $|\ell, s, m_\ell, m_s\rangle$ representation or the $|j, \ell, s, m_j\rangle$ representation. To demonstrate this point, consider an ℓ-state associated with $s = 1$. This state has a degeneracy $(2\ell + 1)(2s + 1) = 3(2\ell + 1)$.

Table 2.2: The multiplicities of the various m_ℓ levels for the $3d4p$ configuration yielding a total of 15 states.

m_ℓ value	number of states
3	1
2	2
1	3
0	3
−1	3
−2	2
−3	1
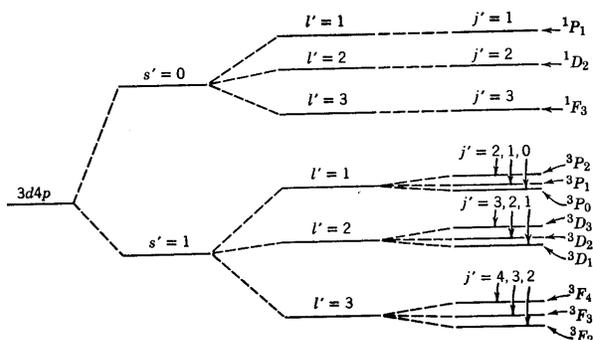
Figure 2.3: Level scheme for the $ndn'p = 3d4p$ electronic configuration where one electron is placed in a $3d$ shell and a second electron is in a $4p$ shell.

When the spin-orbit interaction is turned on we can make three different j values with degeneracies

$$[2(\ell+1)+1] + (2\ell+1) + [2(\ell-1)+1] = 3(2\ell+1) \tag{2.16}$$

so that all levels are accounted for independent of the choice of representation. A diagram illustrating the possible states that can be made from the two-electron configuration $nd\,n'p = 3d\,4p$ is shown in Fig. 2.3. In order to familiarize yourself with this addition of angular momentum, you will construct one of these diagrams for homework. Figure 2.3 is constructed for the case where the two electrons go into different atomic shells. In the case where the two electrons are placed in the same atomic shell, the Pauli principle applies which states that the quantum numbers assigned to the two electrons must be different. Thus, there will be fewer allowed states by the Pauli principle where $n = n'$ and the angular momentum is also the same. To illustrate the effect of the Pauli principle we will consider two electrons in a $2p3p$ configuration (Fig. 2.4) and in a $2p^2$ configuration (Fig. 2.5). A list of possible states for the $2p^2$ configuration is given in Table 2.3.

We notice that in Table 2.3 there are only 15 states in the $2p^2$ configuration because if we have two electrons in a $2p$ level they are indistinguishable and $(m_{\ell_1}, m_{s_1}, m_{\ell_2}, m_{s_2}) = (1, 1/2, 1, -1/2)$ is identical to $(1, -1/2, 1, 1/2)$.

The possible values for s are

$$s_1 + s_2, s_1 + s_2 - 1, \cdots, |s_1 - s_2| \tag{2.17}$$
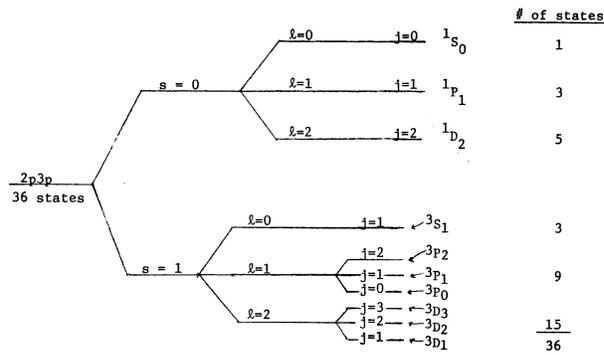
Figure 2.4: States in the $2p\ 3p$ electronic configuration.

Table 2.3: List of states allowed in the $2p^2$ electronic configuration.

m_{ℓ_1}	m_{s_1}	m_{ℓ_2}	m_{s_2}	m_ℓ	m_s	m_j
1	1/2	0	1/2	1	1	2
1	1/2	−1	1/2	0	1	1
0	1/2	−1	1/2	−1	1	0
1	1/2	1	−1/2	2	0	2
1	1/2	0	−1/2	1	0	1
1	1/2	−1	−1/2	0	0	0
0	1/2	0	−1/2	0	0	0
0	1/2	−1	−1/2	−1	0	−1
−1	1/2	−1	−1/2	−2	0	−2
0	1/2	1	−1/2	1	0	1
−1	1/2	1	−1/2	0	0	0
−1	1/2	0	−1/2	−1	0	−1
1	−1/2	0	−1/2	1	−1	0
1	−1/2	−1	−1/2	0	−1	−1
1	−1/2	−1	−1/2	−1	−1	−2

25
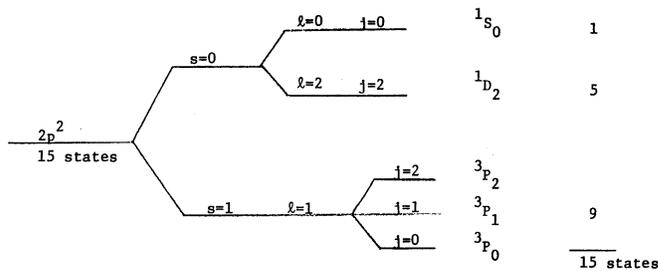
Figure 2.5: Level scheme for the $2p^2$ configuration where the Pauli Exclusion Principle must be considered explicitly.

and for ℓ are

$$\ell_1 + \ell_2, \ell_1 + \ell_2 - 1, \cdots, |\ell_1 - \ell_2| \tag{2.18}$$

and for j are

$$\ell + s, \ell + s - 1, \cdots, |\ell - s|. \tag{2.19}$$

Since the Pauli Exclusion Principle prohibits the state

$$(m_{\ell_1}, m_{s_1}, m_{\ell_2}, m_{s_2}) = (1, 1/2, 1, 1/2)$$

we cannot have $j = 3$ and the states for $s = 1, \ell = 2$ in Fig. 2.4 do not occur in the $2p^2$ configuration. The ground state is then a $^3P_0$ state with higher lying states in that multiplet being $^3P_1$ and $^3P_2$. To account for the m_ℓ value of ± 2 in Table 2.3, we have a state $^1D_2$; and this state is also consistent with the m_j value of 2 when $m_\ell = 2$. With the ^3P states and the $^1D_2$ we have accounted for $9 + 5 = 14$ states and we have one more to go to get to 15. The only way to do this is with a $^1S_0$ state so our diagram becomes as shown in Fig. 2.5.

A general rule to be used in selecting states allowed by the Pauli principle is that the total state must be antisymmetric under exchange of particles, so that if we have a symmetric spin state, the orbital state must be antisymmetric under interchange of particles. Thus for the $s = 1$ symmetric ($\uparrow\uparrow$) spin state, only the antisymmetric orbital state $\ell = 1$ is allowed. Likewise, for the $s = 0$ antisymmetric ($\uparrow\downarrow$) spin state only the $\ell = 0$ and $\ell = 2$ symmetrical orbital states that are allowed, consistent with the allowed states shown in Fig. 2.5.

2.4 Clebsch–Gordan Coefficients

Up to this point we have used physical arguments (such as the vector model) for finding matrix elements of various operators in the $|\ell, s, j, m_j\rangle$ representation. We shall now view this problem from a more mathematical point of view. If we have a wave function in one representation, we can by a unitary transformation change from one representation to another. This is a mathematical statement of the fact that an arbitrary function can be expressed in terms of any complete set of functions. In quantum mechanics, we write such a transformation quite generally as

$$\psi_\alpha = \sum_\beta \phi_\beta \langle \beta | \alpha \rangle \tag{2.20}$$

26

Table 2.4: Listing of the states which couple to the $|\ell, s, j, m_j\rangle$ and $|\ell, s, m_\ell, m_s\rangle$ representations for $\ell = 2$, $s = 1/2$.

m_ℓ	m_s	m_j
2	1/2	5/2
2	−1/2	3/2
1	1/2	3/2
1	−1/2	1/2
0	1/2	1/2
0	−1/2	−1/2
−1	1/2	−1/2
−1	−1/2	−3/2
−2	1/2	−3/2
−2	−1/2	−5/2

where ψ_α is one member of a complete set of functions designated by quantum number α, while ϕ_β is one member of a different complete set of functions labeled by quantum number β, and $\langle\beta|\alpha\rangle$ is the transformation coefficient expressing the projection of one "vector" on another, and the sum in Eq. 2.20 is taken over all quantum numbers β. Because the number of possible states α is equal to the number of states β and because $|\psi_\alpha|^2$ is identified with the magnitude of an observable, $\langle\beta|\alpha\rangle$ is a square matrix which conserves lengths and is hence written as a unitary matrix. If now the function ψ_α is an eigenfunction of the total angular momentum and of its z projection, then ψ_α denotes $|\ell, s, j, m_j\rangle$, where the Dirac ket, expressed in terms of all the four quantum numbers, can be written explicitly with appropriate spherical harmonics. Similarly the function ϕ_β in Eq. 2.20 denotes the wave function $|\ell, s, m_\ell, m_s\rangle$. Then Eq. 2.20 provides an expansion of the $|\ell, s, j, m_j\rangle$ function in terms of the $|\ell, s, m_\ell, m_s\rangle$ function which defines the Clebsch–Gordan coefficients $\langle\ell, s, m_\ell, m_s|\ell, s, j, m_j\rangle$ by

$$|\ell, s, j, m_j\rangle = \sum_{m_s, m_\ell; m_s + m_\ell = m_j} |\ell, s, m_\ell, m_s\rangle\langle\ell, s, m_\ell, m_s|\ell, s, j, m_j\rangle \qquad (2.21)$$

where the sum is on all the m_s and m_ℓ values which contribute to a particular m_j. Since the operator relation $\vec{J} = \vec{L} + \vec{S}$ is valid, we can write $J_z = L_z + S_z$ and also $m_j = m_\ell + m_s$. In writing Eq. 2.21 we also restrict j to lie between $|\ell - s| \le j \le \ell + s$. These rules can be proved rigorously but we will not do so here. Instead, we will illustrate the meaning of the rules. As an example, take $\ell = 2, s = 1/2$. This gives us ten states with m_j values as shown in Table 2.4. We see that except for the $m_j = \pm 5/2$ states, we have two different states with the same m_j value. This is exactly what is needed is provide six m_j states for $j = 5/2$ and four m_j states for $j = 3/2$. Successive j values differ by one and not by 1/2, since we cannot make proper integral m_j values for $j =$ integer in the case $\ell = 2$, $s = 1/2$.

Since the Clebsch–Gordan coefficients form a unitary matrix, we have orthogonality relations between rows and between columns of these coefficients

$$\sum_{m_s, m_\ell} \langle\ell, s, j, m_j|\ell, s, m_\ell, m_s\rangle \, \langle\ell, s, m_\ell, m_s|\ell, s, j', m_j'\rangle = \delta_{j,j'}\delta_{m_j, m_j'} \qquad (2.22)$$

27

$$\sum_{m_j} \langle \ell, s, m_\ell, m_s | \ell, s, j, m_j \rangle \, \langle \ell, s, j, m_j | \ell, s, m'_\ell, m'_s \rangle = \delta_{m_\ell, m'_\ell} \delta_{m_s, m'_s}. \tag{2.23}$$

We now address ourselves to the problem of calculating the Clebsch–Gordan coefficients. In particular, the coefficient $\langle \ell, s, -\ell, -s | \ell, s, (\ell+s), -(\ell+s) \rangle$ is unity since the state $| \ell, s, -\ell, -s \rangle$ in the $| \ell, s, m_\ell, m_s \rangle$ representation is the same as the state $| \ell, s, (\ell+s), -(\ell+s) \rangle$ in the $| \ell, s, j, m_j \rangle$ representation. As an example of this point take $m_\ell = -2$, $m_s = -1/2$ in Table 2.4. This makes an $m_j = -5/2$ state and it is the only way to prepare an $m_j = -5/2$ state. So starting with this minimum m_j value state, we will use the raising operator $J_+ = L_+ + S_+$ of Eq. 1.13 to act on both sides of the equation

$$J_+ | \ell, s, (\ell+s), -(\ell+s) \rangle = (L_+ + S_+) | \ell, s, -\ell, -s \rangle. \tag{2.24}$$

We then get for the left-hand side using the raising operator relation Eq. 1.13

$$\sqrt{([\ell+s]+[\ell+s])([\ell+s]-[\ell+s]+1)} \, | \ell, s, (\ell+s), (-\ell-s+1) \rangle \tag{2.25}$$

where the m_j value has now been raised by unity. From the right hand side of Eq. 2.24 we get

$$\sqrt{(\ell+\ell)(\ell-\ell+1)} \, | \ell, s, -\ell+1, -s \rangle + \sqrt{(s+s)(s-s+1)} \, | \ell, s, -\ell, -s+1 \rangle \tag{2.26}$$

which from Eq. 2.24 gives an equation of the form

$$| \ell, s, (\ell+s), (-\ell-s+1) \rangle = \frac{1}{\sqrt{2(\ell+s)}} \left[\sqrt{2\ell} \, | \ell, s, -\ell+1, -s \rangle + \sqrt{2s} \, | \ell, s, -\ell, -s+1 \rangle \right]. \tag{2.27}$$

Thus we have evaluated the Clebsch–Gordan coefficients:

$$\langle \ell, s, -\ell+1, -s | \ell, s, \ell+s, (-\ell-s+1) \rangle = \sqrt{\frac{\ell}{\ell+s}} \tag{2.28}$$

$$\langle \ell, s, -\ell, -s+1 | \ell, s, \ell+s, (-\ell-s+1) \rangle = \sqrt{\frac{s}{\ell+s}} \tag{2.29}$$

And by repeated application of the raising operator J_+ we can find all the Clebsch–Gordan coefficients corresponding to a given j value. To find the coefficients for the $(j-1)$ quantum states, we must use the orthogonality relations given by Eqs. 2.22 and 2.23 to construct one coefficient and then use raising and lowering operators to produce the remaining coefficients for the $(j-1)$ set of states.

As an example of the Clebsch–Gordan coefficients, consider the addition of angular momentum for two spins (e.g., take $\ell = 1/2$ and $s = 1/2$). The development given here is general and we can imagine this case to illustrate a $\vec{J}$ arising from the addition of two angular momenta, $\vec{J} = \vec{S}_1 + \vec{S}_2$. From Eqs. 2.28 and 2.29 we have for the Clebsch–Gordan coefficients:

$$\left\langle \frac{1}{2}, \frac{1}{2}, \frac{1}{2}, -\frac{1}{2} \middle| \frac{1}{2}, \frac{1}{2}, 1, 0 \right\rangle = \frac{1}{\sqrt{2}} = \left\langle \frac{1}{2}, \frac{1}{2}, -\frac{1}{2}, \frac{1}{2} \middle| \frac{1}{2}, \frac{1}{2}, 1, 0 \right\rangle. \tag{2.30}$$

Clearly $\left\langle \frac{1}{2}, \frac{1}{2}, -\frac{1}{2}, -\frac{1}{2} \middle| \frac{1}{2}, \frac{1}{2}, 1, -1 \right\rangle = 1$. It is convenient to represent these results in matrix form

$\langle \ell, s, m_\ell, m_s \rvert \; / \; \lvert \ell, s, j, m_j \rangle$	$\lvert \frac{1}{2}, \frac{1}{2}, 1, 1 \rangle$	$\lvert \frac{1}{2}, \frac{1}{2}, 1, 0 \rangle$	$\lvert \frac{1}{2}, \frac{1}{2}, 1, -1 \rangle$	$\lvert \frac{1}{2}, \frac{1}{2}, 0, 0 \rangle$
$\langle \frac{1}{2}, \frac{1}{2}, \frac{1}{2}, \frac{1}{2} \rvert$	1	0	0	0
$\langle \frac{1}{2}, \frac{1}{2}, \frac{1}{2}, -\frac{1}{2} \rvert$	0	$\frac{1}{\sqrt{2}}$	0	$\frac{1}{\sqrt{2}}$
$\langle \frac{1}{2}, \frac{1}{2}, -\frac{1}{2}, \frac{1}{2} \rvert$	0	$\frac{1}{\sqrt{2}}$	0	$-\frac{1}{\sqrt{2}}$
$\langle \frac{1}{2}, \frac{1}{2}, -\frac{1}{2}, -\frac{1}{2} \rvert$	0	0	1	0

where the $\langle \ell, s, m_\ell, m_s \rvert$ values label the rows and the $\lvert \ell, s, j, m_j \rangle$ values label the columns. The zero entries in the last column are found by requiring $m_j = m_\ell + m_s$. The $\frac{1}{\sqrt{2}}$ and $-\frac{1}{\sqrt{2}}$ entries are found from normalization. The orthogonality and normalization requirements are valid because the Clebsch–Gordan coefficients form a unitary transformation.

Clebsch–Gordan coefficients are found tabulated in various quantum mechanics texts as well as in books on group theory (in a chapter on the full rotation group). For our present purposes in a solid state course, you should know how to construct such matrices for the addition of small angular momenta such as $\ell = 1$, $s = 1/2$ (homework problem). You should also know how to use tabulated Clebsch–Gordan matrices that you will find in books and journal articles.

Now let us see what the Clebsch–Gordan coefficients have to do with the evaluation of the various matrix elements that occur in problems on magnetism. Suppose we have an operator L_z acting on an eigenfunction in the $\lvert \ell, s, j, m_j \rangle$ representation. The wave function $\lvert \ell, s, j, m_j \rangle$ is <u>not</u> an eigenfunction of L_z; that is, the operator L_z does <u>not</u> act on $\lvert \ell, s, j, m_j \rangle$ to give an eigenvalue times $\lvert \ell, s, j, m_j \rangle$. We can find the action of L_z on $\lvert \ell, s, j, m_j \rangle$ by expressing this state in terms of states which are eigenstates of L_z, namely the states $\lvert \ell, s, m_\ell, m_s \rangle$. We then get

$$L_z \lvert \ell, s, j, m_j \rangle = \sum_{m_\ell, m_s; m_\ell + m_s = m_j} L_z \lvert \ell, s, m_\ell, m_s \rangle \, \langle \ell, s, m_\ell, m_s \lvert \ell, s, j, m_j \rangle \tag{2.31}$$

where the sum is restricted to m_ℓ and m_s values for which $m_j = m_s + m_\ell$. We note that the action of L_z on an eigenstate of L_z gives $m_\ell \hbar \lvert \ell, s, m_\ell, m_s \rangle$. Thus we get for the expectation value of L_z in the $\lvert \ell, s, j, m_j \rangle$ representation a sum over all m_ℓ and m_s states that contribute to m_j:

$$\langle \ell, s, j, m_j \lvert L_z \rvert \ell, s, j, m_j \rangle = \sum_{m_\ell, m_s; m_\ell + m_s = m_j} \hbar m_\ell \langle \ell, s, j, m_j \lvert \ell, s, m_\ell, m_s \rangle \, \langle \ell, s, m_\ell, m_s \lvert \ell, s, j, m_j \rangle. \tag{2.32}$$

It is readily seen that the results obtained with the Clebsch–Gordan coefficients are in agreement with the vector model.

The Clebsch–Gordan coefficients are more general than the vector model discussed in §1.6 in that these coefficients allow the calculation of off-diagonal matrix elements as well as the diagonal matrix elements that can also be evaluated by the vector model. Operators that are not diagonalized by a given representation have non-vanishing off-diagonal matrix elements, as for example $\langle \ell, s, j', m'_j \lvert L_z \rvert \ell, s, j, m_j \rangle$, which enter when considering transitions between eigenstates.

The Clebsch–Gordan coefficients are also useful in finding explicit wave functions in the sense of wave mechanics. For example, we can use the Clebsch–Gordan coefficients to write the wave functions for a given ℓ and $s = 1/2$ namely

$$\lvert \ell, s, m_\ell, m_s = 1/2 \rangle = Y_{\ell m_\ell}(\theta, \phi) \, \chi_\alpha \tag{2.33}$$

29

where χ_α denotes the spin function for spin up. The spin function for spin down would then be written as χ_β and would correspond to $m_s = -1/2$. We can write an explicit expression for $|\ell, s, j, m_j\rangle$ by making use of the spherical harmonics and the Clebsch–Gordan coefficients. An alternate method for finding explicit expressions for the wave functions $|\ell, s, j, m_j\rangle$ is to remain entirely within the bounds of wave mechanics and to use the Addition Theorem for Spherical Harmonics which is discussed in many of the standard quantum mechanics texts.

Chapter 3

Diamagnetism and Paramagnetism of Bound Electrons

3.1 Introductory Remarks

The magnetic properties of solids are described quantitatively in terms of the magnetization $\vec{M}$ which is defined as the magnetic moment per unit volume. Most solids are only weakly magnetic and develop a magnetization only when an external magnetic field is applied. In such cases, the amount of magnetization that is developed depends upon the magnitude of the magnetic susceptibility χ which is defined by

$$\vec{M} = \overleftrightarrow{\chi} \cdot \vec{H} \tag{3.1}$$

where $\overleftrightarrow{\chi}$ is in general a tensor in a crystalline solid. In Gaussian units, χ is dimensionless since $\vec{M}$ and $\vec{H}$ are both measured in the same units – gauss. Materials for which $\chi > 0$ are denoted as paramagnetic and $\chi < 0$ are diamagnetic. Materials with a spontaneous magnetization (i.e., which exhibit a magnetization $\vec{M}$ without application of a magnetic field) typically have much larger values for χ and can be either ferromagnetic, antiferromagnetic or ferrimagnetic, as discussed in Chapter 7. In the present Chapter we focus on materials which are either diamagnetic or paramagnetic and do not exhibit spontaneous magnetization.

Magnetic moments in solids can be associated with both the conduction electrons and the ions (or closed shell valence electrons). In the case of electrons, magnetic moments are associated both with the orbital motion and with the spin angular momentum of these electrons. To understand the intimate connection between magnetic moments and angular momenta, we review here a few basic definitions.

In cgs units, the magnetic induction $\vec{B}$ is related to the magnetic field $\vec{H}$ through the permeability $\overleftrightarrow{\mu}$

$$\vec{B} = \overleftrightarrow{\mu} \cdot \vec{H} = \vec{H} + 4\pi\vec{M} = \vec{H} + 4\pi \overleftrightarrow{\chi} \cdot \vec{H} = (\overleftrightarrow{1} + 4\pi \overleftrightarrow{\chi}) \cdot \vec{H} \tag{3.2}$$

$$\overleftrightarrow{\mu} = \overleftrightarrow{1} + 4\pi \overleftrightarrow{\chi} \geq 0 \tag{3.3}$$

where $\overleftrightarrow{1}$ is the unit second rank tensor having 1's along the main diagonal and zero elsewhere. The condition $1 + 4\pi\chi \geq 0$ is required by thermodynamic stability so that the

maximum diamagnetic susceptibility is $\chi = -1/4\pi$, which is the value of χ for a superconductor that has complete exclusion of the magnetic flux ($B = 0$).

The field variables $\vec{B}$ and $\vec{E}$ are directly derived from the vector and scalar potentials $\vec{A}$ and ϕ respectively:

$$\vec{E} = -\vec{\nabla}\phi - 1/c(\partial\vec{A}/\partial t) \tag{3.4}$$

$$\vec{B} = \vec{\nabla} \times \vec{A}. \tag{3.5}$$

The field variables are unique, but the potentials are not (i.e., a gauge transformation yields a new equivalent potential implying the same field variables)

$$\vec{A}' = \vec{A} + \vec{\nabla}g(\vec{r}, t) \tag{3.6}$$

$$\phi' = \phi - \frac{1}{c}\frac{\partial g(\vec{r}, t)}{\partial t} \tag{3.7}$$

where $g(\vec{r}, t)$ is any analytic function and the gauge transformation given by Eqs. 3.6 and 3.7 does not change the fields in any way. In fact, we require that all measurable quantities be invariant under a gauge transformation.

The magnetic moment associated with the orbital angular momentum is (see §1.3)

$$\vec{\mu} = \left(\frac{e}{2mc}\right)\vec{L} \tag{3.8}$$

in which angular momentum for electrons in atomic states is quantized in units of $\hbar$ and therefore the magnetic moment is quantized in units of Bohr magnetons μ_B

$$\mu_B = \frac{e\hbar}{2mc} = -0.923 \times 10^{-20} \text{ ergs/gauss.} \tag{3.9}$$

The charged particles of solids, electrons and nuclei, not only have orbital angular momentum, but can also have spin angular momentum $\vec{S}$. A magnetic moment $\vec{\mu}$ is also associated with the spin angular momentum $\vec{S}$. Experimental studies of atomic spectra show that the magnetic moment associated with the electron spin can be related to $\vec{S}$ by

$$\vec{\mu} = \left(\frac{eg_s}{2mc}\right)\vec{S} \tag{3.10}$$

where g_s is the g–factor which is 2 for free electrons. Since e is a negative number, the magnetic moment and spin are antiparallel. This g–factor is introduced so that an equivalent relation between the angular momentum and the magnetic moment will be valid for both spin and orbital angular momentum. In a solid, the g–factor (or effective g–factor) can differ from 2, and can in fact be either positive or negative.

In general for free electrons,

$$\vec{\mu} = \left(\frac{eg_\ell}{2mc}\right)\vec{L} + \left(\frac{eg_s}{2mc}\right)\vec{S} = \left(\frac{e}{2mc}\right)(\vec{L} + 2\vec{S}) = \left(\frac{e}{2mc}\right)(\vec{J} + \vec{S}) = \left(\frac{\mu_B}{\hbar}\right)(\vec{J} + \vec{S}). \tag{3.11}$$

Because the g–factor for the electron spin g_s is 2, and not unity, we say that g_s is anomalous. Furthermore, since $g_s = 2$, the magnetic moment $\vec{\mu}$ is not directed along $\vec{J}$, so that $\vec{\mu}$ and $\vec{J}$ cannot be simultaneously diagonalized, and $\vec{\mu}$ and $\vec{J}$ are operators that do not commute.

Table 3.1: The magnitude of various magnetic quantities at several values of magnetic field.

Magnetic field H or B	0.1 tesla	1.0 tesla	10.0 tesla	units
Energy of 1 Bohr magneton $\mu_B B$	0.5×10^{-5}	0.5×10^{-4}	0.5×10^{-3}	eV
Equivalent temperature $\mu_B B / k_B$	0.06	0.6	6	deg K
Cyclotron frequency $eB/mc = \omega_c$	2×10^{10}	2×10^{11}	2×10^{12}	rad/sec
$f_c = \omega_c / 2\pi$	3×10^9	3×10^{10}	3×10^{11}	Hz
$\lambda_c = c / f_c$	10	1	0.1	cm
$\hbar \omega_c$	10^{-5}	10^{-4}	10^{-3}	eV

It is for this reason that the properties of the angular momentum operators in quantum mechanics play a major role in the magnetic properties of solids.

Magnetic moment can be associated with either orbital motion or with spin. Because of the larger nuclear mass, nuclear moments are several orders of magnitude smaller than are the electronic magnetic moments. Nuclear moments are widely studied by the nuclear magnetic resonance technique and provide a valuable and sensitive local probe for studying solids. Nevertheless, the small magnitude of the nuclear moments allows us to neglect them in computing the static magnetization of solids.

The magnetic moment associated with the spin is a permanent moment which is present whether or not a magnetic field is present. On the other hand, the magnetic moment associated with the orbital motion of the electrons is proportional to the applied magnetic field and is called an induced moment. By Lenz's law, the induced moment is always negative and leads to diamagnetic effects.

In calculating the magnetization, we will often need to resort to a statistical approach, because we cannot hope to specify the detailed state of the system. In treating the orbital and spin angular momenta, we must also consider the coupling between $\vec{L}$ and $\vec{S}$ through the spin-orbit interaction. For atoms with high atomic number, the spin-orbit interaction will be large compared with effects associated with laboratory magnetic fields. To determine whether the spin-orbit interaction or the energy associated with magnetic field interactions is larger, we now consider the orders of magnitude of magnetic interactions in solids.

Magnetic energies in solids are generally small compared with electronic energies. That is, electronic energy gaps are of the order 1 eV while magnetic energies are typically in the millivolt range. A useful table showing the order of magnitude of magnetic quantities is given in Table 3.1. We note that the highest dc fields presently available are under 40 tesla, though pulsed fields of over 100 tesla have been achieved.

Inspection of Table 3.1 shows us immediately why most experiments involving magnetic energies of these magnitudes must be carried out at high magnetic fields and low temperatures. To have sharply defined magnetic energy levels we require the magnetic energies $\mu_B B \gg k_B T$, where k_B is Boltzmann's constant. Inspection of Table 3.1 also shows why cyclotron resonance experiments are easier to carry out in semiconductors where the effective masses are typically in the range $m^*/m \sim 0.1$ so that the cyclotron frequency in such semiconductors is one order of magnitude higher than for a free electron at the same value of the B field. Typical semimetals also have carriers with small effective masses, and therefore exhibit relatively large magnetic field interactions.

Typical energies for nuclear magnetic effects are reduced by three to four orders of magnitude from the values given in Table 3.1. For this reason nuclear resonance experiments are usually performed at radio frequencies whereas electron spin resonance experiments are performed at microwave frequencies. The lower energies for nuclear magnetism can be exploited in such experiments as adiabatic magnetization and nuclear polarization (Overhauser effect). In adiabatic demagnetization, the demagnetization of the electronic system results in the generation of temperatures in the millidegree K range. On the other hand, the demagnetization of the nuclear system yields temperatures in the 10^{-6} deg K range because $\mu_N \sim 10^{-3} \mu_B$ where μ_N is the nuclear magneton. Although the magnitude of nuclear magnetism is small compared with electronic effects, nuclear magnetism is of considerable theoretical and practical interest for ultra-low temperature science and technology, as well as for magnetic imaging and for the chemical characterization of crystalline materials.

3.2 The Hamiltonian for Magnetic Interactions for Bound Electrons

Now that we have a feeling for the small order of magnitude involved in the weak magnetic effects in solids, let us look more closely into how we would calculate the energies of electrons in magnetic systems. Using the one-electron Hamiltonian approach to solids, we can write the Hamiltonian which includes the effects of the electromagnetic field and of the permanent magnetic moments as:

$$\mathcal{H} = \frac{[\vec{p} - (e/c)\vec{A}]^2}{2m} + e\phi + V(\vec{r}) - \vec{\mu}_p \cdot \vec{B} \tag{3.12}$$

in which we have not included the spin-orbit interaction but have included the effect of a magnetic field through the vector potential $\vec{A}$, an electric field through the potential ϕ, the periodic potential through $V(\vec{r})$, and permanent magnetic moments through the $\vec{\mu}_p \cdot \vec{B}$ term. To include the spin-orbit interaction, we must add to Eq. 3.12 a term $\mathcal{H}_{s-o} = [1/(2m^2c^2)]\vec{S} \cdot (\vec{\nabla}V \times \vec{p})$ and in the presence of electromagnetic fields we replace $\vec{p} \rightarrow \vec{p} - (e/c)\vec{A}$ in this relation for $\mathcal{H}_{s-o}$. If we are dealing with the problem of a static electric field, we can set the vector potential equal to zero and consider only the scalar potential ϕ. If we are considering a static magnetic field, we can set the scalar potential $\phi = 0$ and consider only the vector potential $\vec{A}$. If we are considering an electromagnetic field ($\omega \neq 0$), then we can also choose our gauge so that $\phi = 0$.

The $\vec{\mu}_p \cdot \vec{B}$ term takes into account the permanent magnetic moments in a solid which arise, for example, from the electron spin. Thus (neglecting for the moment the spin-orbit interaction), we can write the Hamiltonian (Eq. 3.12) for an electron in a magnetic field as

$$\mathcal{H} = \mathcal{H}_0 - \left(\frac{e}{2mc}\right)(\vec{p} \cdot \vec{A} + \vec{A} \cdot \vec{p}) + \frac{e^2 A^2}{2mc^2} + e\phi - \vec{\mu}_p \cdot \vec{B} \tag{3.13}$$

where $\mathcal{H}_0 = p^2/2m + V(\vec{r})$ is the Hamiltonian for an electron in a crystalline solid in zero field. No assumption on the commutivity of $\vec{p}$ and $\vec{A}$ is made in writing Eq. 3.13. For simplicity we can neglect ϕ and the commutator $[p, A]$ to obtain a perturbation Hamiltonian for an electron in a solid

$$\mathcal{H}' = -\frac{e}{mc}\vec{p} \cdot \vec{A} + \frac{e^2 A^2}{2mc^2} - \vec{\mu}_p \cdot \vec{B}. \tag{3.14}$$

We can also introduce the interaction of an electron in a magnetic field through the perturbation Hamiltonian

$$\mathcal{H}' = -\vec{\mu}_{\text{total}} \cdot \vec{B} = -\frac{e}{mc}(\vec{L} + 2\vec{S}) \tag{3.15}$$

For specific solid state problems either Eq. 3.13 or Eq. 3.15 are used.

Since Eq. 3.13 contains the vector potential explicitly it is convenient to use a specific gauge to write the Hamiltonian for magnetic interactions. In the case of a static magnetic field, we can set $\phi = 0$ and the uniform magnetic field in the z direction is derived from a vector potential

$$\vec{A} = \frac{1}{2}(\vec{B} \times \vec{r}) \tag{3.16}$$

with components (in the symmetric gauge)

$$A_x = -\frac{1}{2}yB \qquad A_y = \frac{1}{2}xB \qquad A_z = 0 \tag{3.17}$$

which is substituted into the perturbation Hamiltonian of Eq. 3.14. Then writing $p_j = (\hbar/i)(\partial/\partial x_j)$ and

$$\vec{\mu}_p = \left(\frac{g_s e}{2mc}\right)\vec{S} \tag{3.18}$$

the perturbation Hamiltonian of Eq. 3.14 for an electron in an external magnetic field becomes

$$\mathcal{H}' = \frac{ie\hbar B}{2mc}\left(x\frac{\partial}{\partial y} - y\frac{\partial}{\partial x}\right) + \left(\frac{e^2 B^2}{8mc^2}\right)(x^2 + y^2) - \left(\frac{g_s e}{2mc}\right)\vec{S} \cdot \vec{B} \tag{3.19}$$

where the first term follows from $-(e/2mc)\vec{L} \cdot \vec{B}$ and gives rise to a paramagnetic contribution to χ. However, the second term in Eq. 3.19 which is proportional to B^2 gives rise to a diamagnetic contribution to the susceptibility. The final term in Eq. 3.19 is again paramagnetic and proportional to $\vec{B}$ and is due to the interaction of the spin angular momentum of the electron with the magnetic field.

3.3   Diamagnetism of Bound Electrons

All atoms in gases, liquids and solids exhibit a diamagnetic contribution to the total susceptibility. The origin of this effect can be understood from very elementary considerations, both from the standpoint of classical physics and quantum mechanics.

We first give a classical derivation of the diamagnetic susceptibility of bound electrons. When a magnetic field is applied, the electrons will move to set up a current to oppose the change in magnetic flux. According to the definition of the magnetic moment $\vec{\mu}$ (given in §1.3), we will now show that each electron will contribute to the diamagnetic moment $\vec{\mu}$. Suppose that there are Z electrons in an atom. Then

$$\vec{\mu} = \left(\frac{Ze}{2c}\right)(\vec{r} \times \vec{v}) = \left(\frac{Ze}{2c}\right)\omega\langle\rho_r^2\rangle\hat{b} \tag{3.20}$$

where $\hat{b}$ is a unit vector along $\vec{B}$ and ρ_r is the distance of an electron from the center of its magnetic field-induced orbit in a plane $\perp$ to the magnetic field, and ω is the Larmor frequency of precession for a bound electron, where $\omega = -eB/2mc$. We therefore obtain

$$\vec{\mu} = -\left(\frac{Ze^2\vec{B}}{4mc^2}\right)\langle\rho_r^2\rangle \tag{3.21}$$

which is independent of temperature. This moment is induced and is not present as $B \to 0$. The diamagnetic susceptibility is then $[\chi = (\partial \vec{\mu} / \partial \vec{H}) / \text{volume}]$

$$\chi = -\left(\frac{Ne^2 Z}{4mc^2}\right)\hat{\mu}\langle\rho_r^2\rangle \tag{3.22}$$

where N is the atomic density and the permeability $\hat{\mu} \simeq 1$. The quantity $\langle\rho_r^2\rangle$ in Eq. 3.22 is related to the orbit made by an electron moving in a magnetic field is not well defined classically. However, Eq. 3.22 tells us that if $\langle\rho_r^2\rangle$ is large, the electrons will give a greater contribution to the diamagnetic susceptibility. The simple classical approach given above provides us with the magnitude and functional dependence for the diamagnetic contribution to χ, though we must still calculate $\langle\rho_r^2\rangle$. Our classical model is that electrons in an atom are arranged in shells. Without a magnetic field, the electrons assume a spherically symmetric state of motion in each shell. In a magnetic field, it is only the motion perpendicular to the field that is relevant to the magnetic properties. In this plane there will be a net circulation of charge for each atomic shell, characterized by the Larmor frequency.

To give a more satisfactory description of orbital diamagnetism, we will now give a quantum mechanical derivation of $\chi(T)$ and explicitly consider the charge distribution for electrons in bound states. The one-electron perturbation Hamiltonian of Eq. 3.19 is the basis of the quantum mechanical treatment.

Let us for the moment just deal with the diamagnetic term

$$\mathcal{H}'_{\text{dia}} = \left(\frac{e^2 B^2}{8mc^2}\right)(x^2 + y^2) \tag{3.23}$$

that appears in Eq. 3.19. Since it is small, it can be handled in perturbation theory. Then, in first-order perturbation theory, we get a correction to the electron energy $E_{\text{dia}}^{(1)}$ due to the diamagnetism of the bound electrons:

$$E_{\text{dia}}^{(1)} = \left(\frac{e^2 B^2}{8mc^2}\right)\sum_i \langle\psi_0^i|\rho_r^2|\psi_0^i\rangle \tag{3.24}$$

and the matrix element of ρ_r^2 is summed over all electrons. In the spirit of perturbation theory the diagonal matrix element of $\rho_r^2 = (x^2 + y^2)$ in Eq. 3.24 is generally calculated for zero magnetic field between ground state electronic wave functions ψ_0^i.

We can interpret the diamagnetic energy of Eq. 3.24 as arising from a magnetic moment induced by the field and directed along the field. Thus, according to the definition of the magnetic moment we obtain

$$\vec{\mu} = -\frac{\partial \vec{E}_{\text{dia}}}{\partial \vec{B}} = -\left(\frac{e^2 \vec{B}}{4mc^2}\right)\sum_i\langle\rho_r^2\rangle \tag{3.25}$$

where $\langle\rho_r^2\rangle$ denotes the diagonal matrix elements appearing in Eq. 3.24 and the sum in Eq. 3.25 is over all electrons in the atom. The quantum mechanical calculation of Eqs. 3.24 and 3.25 thus yield the same result for χ as was obtained classically (see Eq. 3.21), only now we have a well-defined method for calculating this expectation value of ρ_r^2. For homework, we will evaluate $\vec{\mu}$ for a specific atomic system, hydrogen.
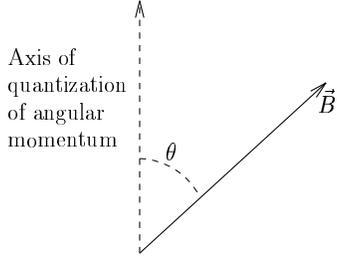
Figure 3.1: Diagram showing the orientation of the magnetic field relative to the axis of quantization of angular momentum in a crystal.

If the magnitude of the diamagnetic interaction is sufficiently large, we must go to 2nd order perturbation theory. Then we get a second order contribution to E_{dia} from the various excited states

$$E_{\text{dia}}^{(2)} = \sum \frac{|\langle \psi_0 | \mathcal{H}'_{\text{dia}} | \psi_{\text{excited}} \rangle|^2}{(E_{\text{ground}} - E_{\text{excited}})} \tag{3.26}$$

where $\mathcal{H}'_{\text{dia}}$ is given by Eq. 3.23 Terms obtained in second order perturbation theory using Eq. 3.26 are sometimes important and must be considered for the following reason. Up until now we have assumed that the quantization of angular momentum is along the magnetic field. In a solid, we are likely to carry out the quantization in terms of the crystallographic axes. But then the magnetic field direction must be expressed with respect to the crystal coordinates, in which case the perturbation Hamiltonian (Eq. 3.23) requires minor revision:

$$\mathcal{H}' = \sum_i \left(\frac{e^2 B^2}{8mc^2} \right) r_i^2 \cos^2 \theta_i \tag{3.27}$$

where the summation is over all the electrons and θ_i is the angle between the magnetic field and the axis of quantization of the angular momentum (see Fig. 3.1). In a solid the diamagnetic contribution to the magnetic moment may vanish in 1st order perturbation theory for certain magnetic field directions and we must go to 2nd order. It often turns out that the 2nd order term $E_{\text{dia}}^{(2)}$ is of the opposite sign to the 1st order term $E_{\text{dia}}^{(1)}$ and, therefore, $E_{\text{dia}}^{(2)}$ gives a paramagnetic contribution to χ (compare with the first order term in Eq. 3.24 which gives a diamagnetic contribution to χ):

$$E_{\text{dia}}^{(2)} = +\frac{2|\langle \psi_0 | \mathcal{H}'_{\text{dia}} | \psi_{\text{excited}} \rangle|^2}{(E_0 - E_{\text{excited}})} = -\frac{2|\langle \psi_0 | \mathcal{H}'_{\text{dia}} | \psi_{\text{excited}} \rangle|^2}{E_g} \tag{3.28}$$

where for simplicity we consider only one excited state and E_g is the energy gap between the ground state and the excited state. The paramagnetic contribution in Eq. 3.28 is called Van-Vleck paramagnetism. Like $E_{\text{dia}}^{(1)}$, the second order term $E_{\text{dia}}^{(2)}$ originates from purely orbital motion and like $E_{\text{dia}}^{(1)}$ is temperature independent. In general, the most important contribution from the orbital motion comes in first-order perturbation theory and we don't have to worry about second order terms. We have just included this idea into the present discussion to show that the orbital motion may give rise to both diamagnetic and paramagnetic contributions.

For the inert gases, the only contribution to the magnetism from the bound state electrons is the diamagnetic contribution and typical experimental values for the magnetic susceptibility are:

$$\chi_{\text{molar}} \sim -1.9 \times 10^{-6} \text{ cm}^3/\text{mole} \quad \text{Helium} \quad Z=2$$
$$\chi_{\text{molar}} \sim -43 \times 10^{-6} \text{ cm}^3/\text{mole} \quad \text{Xenon} \quad Z=54 \ .$$

Neglecting for the moment that the electrons in xenon occupy several different atomic shells (or have different principal quantum numbers), since xenon has 54 electrons compared to 2 for helium, we can get a rough check on the idea that <u>all</u> electrons contribute to diamagnetism from the product

$$(1.9)(27) \simeq 51.$$

3.4 Paramagnetism of Bound Electrons

Whereas all atoms possess core diamagnetism, not all atoms possess core paramagnetism. Referring to Eq. 3.19, the perturbation Hamiltonian which describes the paramagnetism due to the bound electrons is

$$\mathcal{H}'_{\text{para}} = \sum_i -\left(\frac{e}{2mc}\right)(\vec{L}_i + 2\vec{S}_i) \cdot \vec{B} = -\vec{\mu}_{\text{para}} \cdot \vec{B} \tag{3.29}$$

where

$$\vec{\mu}_{\text{para}} = \frac{e}{2mc}\sum_i(\vec{L}_i + 2\vec{S}_i). \tag{3.30}$$

Thus if we have a closed atomic shell, the total $\vec{L}$ and total $\vec{S}$ both vanish and $\mathcal{H}'_{\text{para}}$ vanishes too. For helium, as an example, both electrons are in an s-states (zero angular momentum) and have antiparallel spins, so that there is no paramagnetic contribution due to the bound electrons.

The calculation for the paramagnetism for the bound electrons characteristically is treated in two parts:

1. determination of the moment $\vec{\mu}_{\text{para}}$

2. a statistical calculation of the average of $\vec{\mu}_{\text{para}}$.

With regard to the calculation of $\vec{\mu}_{\text{para}}$, it may be carried out either classically (approximately valid for large values of the angular momentum) or quantum mechanically. With regard to the statistical problem, thermal disorder acts to randomize the alignment of the moments by the magnetic field so that the average value of $\vec{\mu}_{\text{para}}$ will be temperature dependent, in contrast to the situation for the diamagnetism for the bound electrons which is independent of temperature.

For paramagnetic materials, Eq. 3.30 shows that the magnetic moment is independent of the magnetic field but is a property of the atomic system; such moments are called <u>permanent</u> moments, in contrast to moments which are induced by the presence of a magnetic field, such as the case for the diamagnetic contribution to χ which is discussed in §3.3. The magnetic field tends to line up the moments and thermal energy tends to randomize the orientation of the magnetic moments.

We will first give a classical derivation of Curie's law which provides a good way to think about paramagnetic systems, even if it must later be refined to take into account the quantum mechanical aspects of the problem.

The interaction energy of a magnetic moment with the magnetic field is

$$E = -\vec{\mu}_{\text{para}} \cdot \vec{B}. \tag{3.31}$$

Insofar as the magnetic energy tends to be small compared with the thermal energy, the permanent moments can be excited by thermal excitation to higher energy states whereby $\vec{\mu}_{\text{para}}$ is no longer along $\vec{B}$. Thus the average energy at temperature T is found by performing a statistical average through summing over all states

$$\langle E \rangle = \frac{\sum [-\vec{\mu}_{\text{para}} \cdot \vec{B}] e^{\vec{\mu}_{\text{para}} \cdot \vec{B}/k_B T}}{\sum e^{\vec{\mu}_{\text{para}} \cdot \vec{B}/k_B T}} \tag{3.32}$$

where we have written k_B for Boltzmann's constant. In doing the problem classically, $\vec{\mu}_{\text{para}}$ and $\vec{B}$ can make any arbitrary angle with respect to each other (this is not so quantum-mechanically). Classically we can write

$$\cos \theta = \frac{\vec{\mu}_{\text{para}} \cdot \vec{B}}{|\mu_{\text{para}}| B} \tag{3.33}$$

so that the sums in Eq. 3.32 become integrals over θ. Let $x = \mu_{\text{para}} B/k_B T \ll 1$ where x denotes the ratio of the magnetic energy to the thermal energy and also let $y = \cos \theta$. We now perform an angular integration as indicated in

$$\int_0^{2\pi} d\phi \int_0^{\pi} \sin \theta d\theta, \tag{3.34}$$

where we use the coordinate system in Fig. 1.1. If we set $y = \cos \theta$, then

$$\langle E \rangle = -\mu_{\text{para}} B \left(\frac{\int_{-1}^{1} e^{xy} y \, dy}{\int_{-1}^{1} e^{xy} dy} \right) \tag{3.35}$$

and

$$\langle E \rangle = -\mu_{\text{para}} B \left(\frac{d}{dx} \right) \ln \int_{-1}^{1} e^{xy} dy = -\mu_{\text{para}} B \left[\left(\frac{d}{dx} \right) \ln(e^x - e^{-x}) - \left(\frac{d}{dx} \right) \ln x \right] \tag{3.36}$$

$$= -\mu_{\text{para}} B \left[\coth x - \frac{1}{x} \right] \equiv -\mu_{\text{para}} B \, L(x) \tag{3.37}$$

where $L(x)$ is the dimensionless Langevin function shown in Fig. 3.2.

A Taylor expansion of $\coth x$ for small x is

$$\coth x = 1/x + x/3 - x^3/45 + \cdots \tag{3.38}$$

so that

$$L(x) = x/3 - x^3/45 + \cdots \tag{3.39}$$

is the expansion of $L(x)$ for small x. For very small x, we retain only the leading term or

$$L(x) \simeq \frac{x}{3} = \frac{\mu_{\text{para}} B}{3 k_B T}. \tag{3.40}$$

39

Figure 3.2: Plot of the dependence of the Langevin function $L(x)$ on x (solid curve) where $L(x) = \coth x - (1/x)$ and $x = \mu_{\text{para}}B/k_BT$. For small x $L(x) \sim x/3$ (dashed curve).)
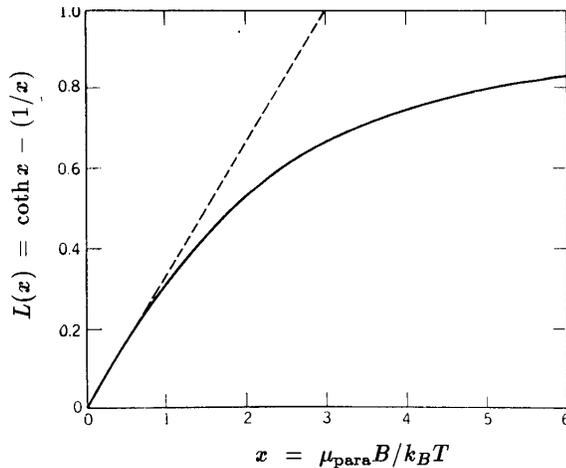
Since $\langle E \rangle = -\langle \mu_{\text{para}} \rangle B$ we have for the thermal average $\langle \mu_{\text{para}} \rangle$

$$\langle \mu_{\text{para}} \rangle = \frac{\mu_{\text{para}}^2 B}{3k_BT} \tag{3.41}$$

so that

$$\chi_{\text{para}} = \frac{N\mu_{\text{para}}^2 \hat{\mu}}{3k_BT} = \frac{C}{T} \tag{3.42}$$

where C is Curie's constant and $\hat{\mu}$ is the permeability. Equation 3.42 which expresses a proportionality between χ_{para} and $1/T$ is called the Curie law.

From this treatment you see that the Curie law, which gives the functional form of $\chi_{\text{para}}(T)$ as $1/T$ is only approximate. That is, classically the temperature dependence of χ_{para} is given by the Langevin function $L(x)$ shown in Fig. 3.2, which reduces to the Curie relation for small x when the magnetic energy is much less than the thermal energy.

At low temperatures we would expect departures from the $1/T$ law according to the plot shown in Fig. 3.2. When we do the problem quantum-mechanically below, we will find that yet another function applies. Nevertheless, saturation effects, as suggested by the Langevin function, are observed experimentally as shown in Fig. 3.3. From the discussion given so far, we conclude that if we want to enhance the paramagnetic behavior, we need to go to low temperatures and if we want to enhance the diamagnetic behavior we need to go to high fields.

Now let us think about the changes that we must make in the above treatment to make it quantum-mechanical. For one thing, we must find an explicit expression for μ_{para} by finding the expectation value of the magnetic moment operator in an eigenstate of the total Hamiltonian $\mathcal{H}'_{\text{para}}$ in Eq. 3.29 in the $|\ell, s, j, m_j\rangle$ representation. The magnetic moment can be found easily using the vector model.

By treating the magnetic moment as a quantized operator, we can using Eqs. 1.127 and 1.133 write the quantum mechanical energy levels in the form

$$E_j = -m_j g\mu_B B \tag{3.43}$$

40

Figure 3.3: Plot of magnetic moment versus H/T for spherical samples of (I) potassium chromium alum, (II) ferric ammonium alum, and (III) gadolinium sulfate octahydrate. Over 99.5% magnetic saturation is achieved at a low temperature of 1.3 K and a field of about 50,000 gauss. The fit to the experimental data makes use of Eq. 3.52 which expresses the magnetic moment in terms of a Brillouin function. [After W.E. Henry, Phys. Rev. 88, 559 (1952)]

(a)
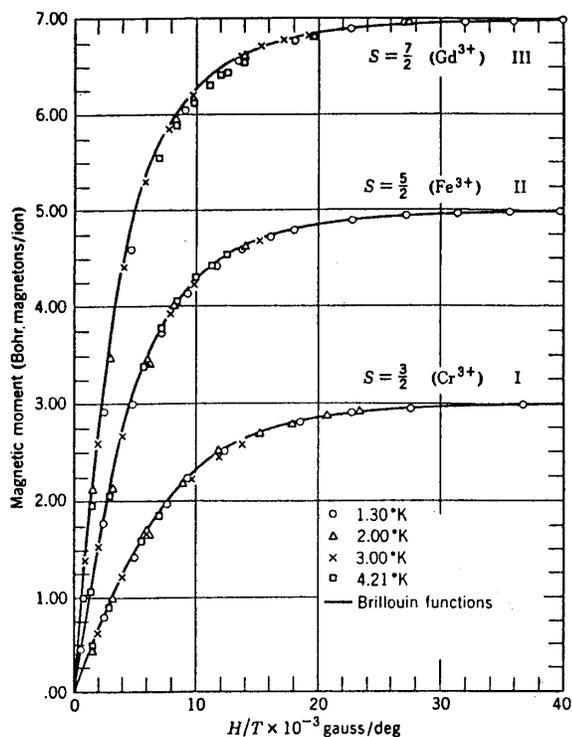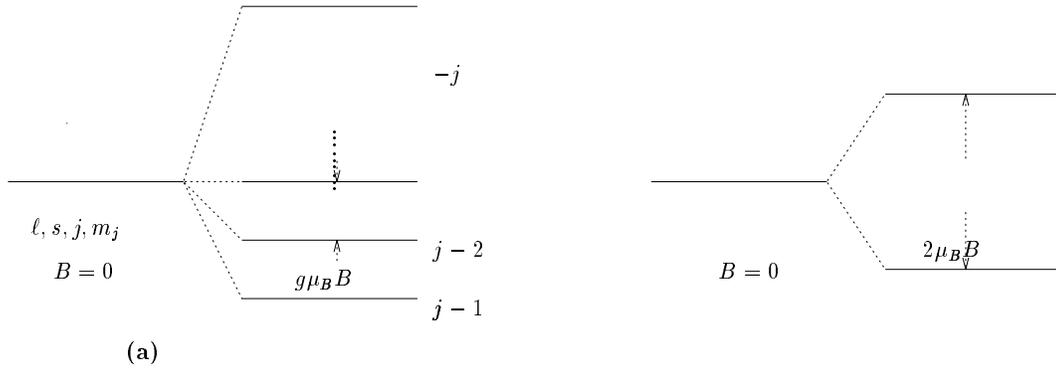
Figure 3.4: (a) Equally spaced levels for different m_j values $-j \leq m_j \leq j$ in a magnetic field where the Zeeman splitting between adjacent levels is $g\mu_B B$ where g is the Landé g–factor. (b) For a 2-level, spin up and spin down system, the Zeeman splitting is $2\mu_B B$.

where g is the Landé g–factor

$$g = \frac{[\frac{3}{2}j(j+1) + \frac{1}{2}s(s+1) - \frac{1}{2}\ell(\ell+1)]}{j(j+1)} \tag{3.44}$$

and μ_B is the Bohr magneton. These magnetic energy levels are equally spaced, since the quantum number m_j is either an integer or half-integer and can assume values

$$m_j = j, j-1, \ldots, -j. \tag{3.45}$$

For a two level spin up and spin down system, we have $s = 1/2$ and $\ell = 0$, $g = 2$, $m_j = \pm 1/2$ and $E = \pm\mu_B B$, while for a more general set of quantum numbers we have an equally spaced set of Zeeman levels shown in Fig. 3.4(a).

Quantum mechanically the mean value for the magnetic moment is found, as before, by computing the mean energy

$$\langle E \rangle = \frac{\sum_{m_j} e^{m_j g\mu_B B/k_B T}(-m_j g\mu_B B)}{\sum_{m_j} e^{m_j g\mu_B B/k_B T}}. \tag{3.46}$$

To simplify the notation let $x = g\mu_B Bj/k_B T$ where $j =$ maximum value which m_j can assume. Physically, x denotes the ratio between the magnetic energy and the thermal energy. The sums in Eq. 3.46 can be related to geometric series by recognizing that

$$\langle E \rangle = -g\mu_B Bj \frac{\sum_{m_j}(m_j/j)e^{m_j x/j}}{\sum_{m_j} e^{m_j x/j}}$$
$$= -g\mu_B Bj(\frac{\partial}{\partial x}) \ln \sum_{m_j=-j}^{j} e^{m_j \frac{x}{j}}. \tag{3.47}$$

The geometric sum in Eq. 3.47 then yields

$$\sum_{m_j=-j}^{j} e^{m_j \frac{x}{j}} = \frac{[e^{(j+1)\frac{x}{j}} - e^{-j\frac{x}{j}}]}{[e^{\frac{x}{j}} - 1]} = \frac{[e^{(j+1/2)\frac{x}{j}} - e^{-(j+1/2)\frac{x}{j}}]}{[e^{\frac{x}{2j}} - e^{-\frac{x}{2j}}]} \tag{3.48}$$

42

thereby giving the following results for the mean energy

$$\langle E \rangle = -g\mu_B B j \left(\frac{\partial}{\partial x} \right) \left[\ln \left(\sinh \left(\frac{2j+1}{2j} x \right) \right) - \ln \left(\sinh \left(\frac{x}{2j} \right) \right) \right] \tag{3.49}$$

$$= -g\mu_B B j \left[\left(\frac{2j+1}{2j} \right) \frac{\cosh(\frac{2j+1}{2j})x}{\sinh(\frac{2j+1}{2j})x} - \left(\frac{1}{2j} \right) \left(\frac{\cosh(\frac{x}{2j})}{\sinh(\frac{x}{2j})} \right) \right] \tag{3.50}$$

so that

$$\langle E \rangle = -g\mu_B B j \left[\left(\frac{2j+1}{2j} \right) \left(\coth(\frac{2j+1}{2j})x \right) - \left(\frac{1}{2j} \right) \left(\coth(\frac{x}{2j}) \right) \right] = -(g\mu_B B j) B_j(x) \tag{3.51}$$

where $B_j(x)$ is defined as the Brillouin function. By writing $\langle E \rangle = -\langle \mu_{\text{para}} \rangle B$, we can obtain the mean magnetic moment (thermal average) as

$$\langle \mu_{\text{para}} \rangle = g\mu_B j B_j(x) \tag{3.52}$$

and by multiplying $\langle \mu_{\text{para}} \rangle$ by N, the number of magnetic moments per unit volume, we obtain $N\langle E \rangle = -N\langle \mu_{\text{para}} \rangle B$, where $N\langle \mu_{\text{para}} \rangle$ is the magnetization per unit volume. The quantity $\langle \mu_{\text{para}} \rangle$ is plotted in Fig. 3.3 for several magnetic compounds with different $j = S$ values, yielding excellent agreement between the experimental data and $\langle \mu_{\text{para}} \rangle$ calculated from Eq. 3.52.

The expansion of the Brillouin function for small x is

$$B_j(x) = \left(\frac{j+1}{3j} \right) x - \left[(j+1)^2 + j^2 \right] \frac{(j+1)}{90j^3} (x^3) + \cdots \tag{3.53}$$

and this result can be used to derive Curie's law by writing $B_j(x) \simeq (\frac{j+1}{3j})x$ for small x. Thus for $x \ll 1$,

$$\langle \mu_{\text{para}} \rangle \simeq g\mu_B j \left(\frac{j+1}{3j} \right) \frac{g\mu_B B j}{k_B T} = \frac{g^2 \mu_B^2 B j (j+1)}{3k_B T} \tag{3.54}$$

or

$$\chi_{\text{para}} = \frac{N\hat{\mu} g^2 \mu_B^2 j(j+1)}{3k_B T}. \tag{3.55}$$

It is of interest to compare the quantum mechanical derivation of the Curie law to the classical derivation of Eq. 3.42. A comparison of Eq. 3.42 and 3.55 suggests the identification of

$$\mu_{\text{para}}^2 \equiv g^2 \mu_B^2 j(j+1) \tag{3.56}$$

where the j and Landé g–factor g for a particular magnetic species are found by quantum mechanics (see §1.6).

By making measurements of the temperature dependence of the magnetic susceptibility, we can determine the Curie constant C which is defined by the Curie law

$$\chi_{\text{para}} = \frac{C}{T} \tag{3.57}$$

through Eq. 3.55 as

$$C = \frac{N\hat{\mu} g^2 \mu_B^2 j(j+1)}{3k_B}. \tag{3.58}$$

43

Figure 3.5: Plot of the susceptibility per gram versus reciprocal temperature for powdered $CuSO_4 \cdot K_2SO_4 \cdot 6H_2O$, showing the Curie law temperature dependence. [After J.C. Hupse, *Physica* **9**, 633 (1942).]
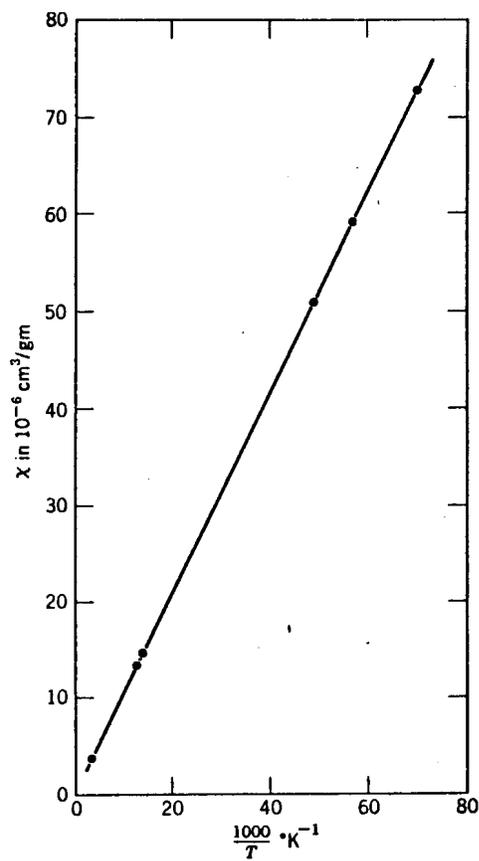
Table 3.2: Effective magneton numbers p for trivalent lanthanide group ions (near room temperature).

Ion	Configuration	Basic level	p(calc)	p(exp)
Ce^{3+}	$4f^1 5s^2 p^6$	$^2F_{5/2}$	2.54	2.4
Pr^{3+}	$4f^2 5s^2 p^6$	$^3H_4$	3.58	3.5
Nd^{3+}	$4f^3 5s^2 p^6$	$^4I_{9/2}$	3.62	3.5
Pm^{3+}	$4f^4 5s^2 p^6$	$^5I_4$	2.68	–
Sm^{3+}	$4f^5 5s^2 p^6$	$^6H_{5/2}$	0.84	1.5
Eu^{3+}	$4f^6 5s^2 p^6$	$^7F_0$	0	3.4
Gd^{3+}	$4f^7 5s^2 p^6$	$^8S_{7/2}$	7.94	8.0
Tb^{3+}	$4f^8 5s^2 p^6$	$^7F_6$	9.72	9.5
Dy^{3+}	$4f^9 5s^2 p^6$	$^6H_{15/2}$	10.63	10.6
Ho^{3+}	$4f^{10} 5s^2 p^6$	$^5I_8$	10.60	10.4
Er^{3+}	$4f^{11} 5s^2 p^6$	$^4I_{15/2}$	9.59	9.5
Tm^{3+}	$4f^{12} 5s^2 p^6$	$^3H_6$	7.57	7.3
Yb^{3+}	$4f^{13} 5s^2 p^6$	$^2F_{7/2}$	4.54	4.5

The Curie law is very well obeyed by paramagnetic salts, as shown in Fig. 3.5 where χ is plotted vs. $1/T$. The points are experimental and the fit is to Eq. 3.57.

In deriving Curie's law, we neglected any interactions between magnetic moments (called the dipole-dipole interaction). The dipole-dipole interaction $\mathcal{H}_{\text{dip}}$ between magnetic moments $\vec{\mu}_1$ and $\vec{\mu}_2$ is given by

$$\mathcal{H}_{\text{dip}} = \frac{1}{r^3}\left[\vec{\mu}_1 \cdot \vec{\mu}_2 - 3(\vec{\mu}_1 \cdot \hat{r})(\vec{\mu}_2 \cdot \hat{r})\right] \tag{3.59}$$

where $\vec{r}$ is the vector between the dipoles and $\hat{r}$ is a unit vector along $\vec{r}$. The dipole-dipole interaction tends to line up a dipole due to the magnetic field generated by neighboring dipoles.

3.5   Angular Momentum States in Paramagnetic Ions

Some paramagnetic systems that have important practical applications (such as laser materials) are insulating host crystals containing a small concentration of paramagnetic impurities. The paramagnetic susceptibility in the low field limit is found by the Curie law

$$\chi_{\text{para}} = \frac{N\hat{\mu}\mu_{\text{para}}^2}{3k_B T} \tag{3.60}$$

where μ_{para} is given by Eq. 3.56 in which j and g are found by the vector model. Experimental values for μ_{para} for the rare earth ions are given in Table 3.2 where p is defined by $p^2 = g^2 j(j+1)$ where p physically denotes the effective number of Bohr magnetons. The comparison between the calculated and experimental values of p in Table 3.2 shows

the excellent agreement between the calculated and experimental values for μ_{para} for the various rare earth ions.

Although Table 3.2 is useful for describing the ground state of rare earth paramagnetic ions, it does not give information about the excited states. Information about the energy levels of the excited states are of great value to people who design laser materials. Such information is largely established by optical techniques. Many of the high power solid state lasers used commercially today involve a population inversion created between some excited levels of a paramagnetic rare earth ion in an ionic host material – e.g. Nd:YAG. A R&D field that has been on–going for some time is the development of more efficient laser materials with lower operating thresholds and at more laser frequencies based on excited states of these rare earth ions.

3.6   Paramagnetic Ions and Crystal Field Theory

Crystal field theory is important for the discussion of the properties of paramagnetic ions (such as rare earth ions or transition metal ions) in a host crystal. Since the magnetic ions are well separated from each other, they behave like atomic entities and the treatment we have given in §3.5 is appropriate. There are several effects, however, that are different for paramagnetic ions in a solid as compared with a gas, including crystal field splittings and, in the case of transition metal ions, the quenching of the orbital angular momentum.

The basic assumption of crystal field theory is that the crystal is ionic. Each atom gives up or receives electrons to make a closed shell or a more stable electron configuration. Examples where crystal field theory applies are host materials, such as Al_2O_3 and MgO. Here, each ion is bonded to ions of opposite charge and the bonds are called ligands. We may assign a radius to each ion or ion core.

In crystal field theory (also called ligand field theory) we assume that the paramagnetic ion is surrounded by a set of point charges. We then find the electric potential $eV(r_i, \theta_i, \phi_i)$ produced by these ions and ligands and include this term in the Hamiltonian $\mathcal{H}$ for the paramagnetic ion. This theory is most useful in magnetically dilute substances where paramagnetic ions are far apart. Examples where crystal field theory applies include 1% Cr^{3+} in Al_2O_3 (which constitutes a common laser material), and 1% Er^{3+} in $LaCl_3$. The Hamiltonian for the paramagnetic ion is given by

$$\mathcal{H} = \sum_{i=1}^{n}\left[\left(\frac{p_i^2}{2m}\right) - \frac{e^2 Z}{r_i} + e^2 \sum_{j>i}\frac{1}{r_{ij}}\right] + \lambda \vec{L}\cdot\vec{S} + \sum_{i=1}^{n} eV(r_i, \theta_i, \phi_i) \tag{3.61}$$

which can be written as:

$$\mathcal{H} = \mathcal{H}_{\text{ion}} + \mathcal{H}_{\text{s}-\text{o}} + \mathcal{H}_{\text{crystal field}} \tag{3.62}$$

where the sums are over all the electrons and $V(r_i, \theta_i, \phi_i)$ is the crystal field potential produced by the ligands at the site r_i. Figure 3.6 shows the splittings of the ionic energy levels by the crystal field and the spin-orbit interaction. There are three cases of interest, depending on the relative magnitudes of the crystal field potential and the spin-orbit interaction.

1. <u>Strong Crystal Field</u> – Here the crystal field is large compared with the spin-orbit interaction. Thus the crystal field breaks up the $\vec{L}\cdot\vec{S}$ coupling of the atomic electrons.

46

$$\mathcal{H}_{\text{ion}} \qquad\qquad \mathcal{H}_{\text{ion}} + V_{\text{cubic}} \qquad\qquad \mathcal{H}_{\text{ion}} + V_{\text{cubic}} + \mathcal{H}_{\text{s}-\text{o}}$$
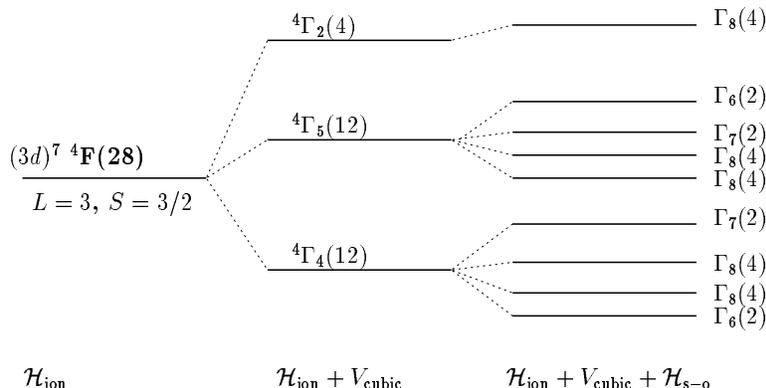
Figure 3.6: Crystal field splittings for a paramagnetic ion with a $(3d)^7$ configuration in the regime where the crystal field is much larger than the spin–orbit interaction.

The transition metal compounds having incomplete $3d$-shells are in this category. Orbital angular momentum is quenched by the strong crystal field.

2. Medium Crystal Field – Here the crystal field is of comparable magnitude to the spin-orbit interaction. Thus the crystal field breaks up the $\vec{L} \cdot \vec{S}$ coupling, but ℓ and s remain good quantum numbers. Co^{2+} and Ni^{2+} with an incomplete $3d$ shell are in this category. Orbital angular momentum is usually quenched in part for this case.

3. Weak Crystal Field – Here the crystal field is small compared with the spin-orbit interaction. Thus in this case j is a good quantum number. Rare earth ions which have an incomplete $4f$ level belong to this case. $4f$ electrons are more shielded from their ligands than $3d$ electrons, and hence the crystal field is weaker for the $4f$ electrons.

The crystal field $V(r_i, \theta_i, \phi_i)$ is invariant under every symmetry operation which leaves the crystal structure invariant. The crystal field potential can be found by summing the potential of point charges of nearest neighbors, next nearest neighbors, etc. Therefore, the crystal field potential does not exhibit spherical symmetry but rather the symmetry of the crystalline lattice. Once the spherical symmetry is lifted, $\vec{J}$ is no longer a constant of the motion. By lowering the symmetry from full rotational symmetry of the free ion to the crystal symmetry of the lattice, certain degeneracies in the energy are lifted, as shown in Fig. 3.6. A more detailed discussion of crystal field theory is given in a course on group theory.

A second effect which occurs in crystals with strong crystal fields is the quenching of the orbital angular momentum, which is discussed in the next section.

3.7 Quenching of Orbital Angular Momentum

Let us consider the quenching of the orbital angular momentum which occurs in materials with a strong crystal field. For simplicity consider an ion with a single electron in a p-state, with all other electrons being accommodated in a closed shell. Neglecting both the effect
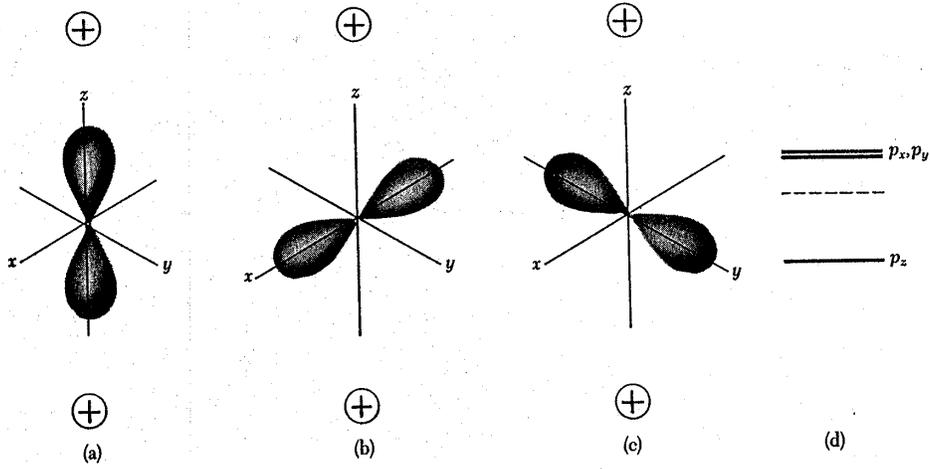
Figure 3.7: A schematic representation of the eigenfunctions (a), (b), (c) and energy eigenvalues (d) for a uniaxial crystal field along the z–direction and $L = 1$. In the free atom the states $m = +1, 0, -1$ have identical energies so that the states are degenerate. In the crystal the atom has a lower energy when the electron cloud is coupled to positive ions as in (a) than when it is oriented midway between them, as in (b) and (c). The wavefunctions that give rise to these charge densities are of the form $zf(r), xf(r)$ and $yf(r)$ and are called the p_z, p_x, p_y orbitals, respectively. In an axially symmetric field, as shown, the p_x and p_y orbitals are degenerate. The energy levels referred to the free atom (dotted line) are shown in (d). If the electric field does not have axial symmetry, all three states will have different energies.

of the electron spin and of the spin-orbit interaction, we can write down three degenerate p-states:

$$Y_{1,1}(\theta, \phi) R_{n,\ell}(r) \propto \left[(x + iy)/\sqrt{2} \right] f(r) \qquad m = 1$$

$$Y_{1,0}(\theta, \phi) R_{n,\ell}(r) \propto z\ f(r) \qquad\qquad m = 0 \qquad\qquad (3.63)$$

$$Y_{1,-1}(\theta, \phi) R_{n,\ell}(r) \propto \left[(x - iy)/\sqrt{2} \right] f(r) \qquad m = -1.$$

Since p-states are degenerate in the free atom, we write them in a form that that displays the crystal symmetry, as shown in Fig. 3.7. The proper eigenfunctions to display a p-function in a cubic crystal field are $xf(r)$, $yf(r)$ and $zf(r)$ (see Fig. 3.7). The energy levels are also indicated in this figure.

Let us find the average value of L_z (denoted by $\langle L_z \rangle$) for the $xf(r)$ state:

$$xf(r) = \frac{1}{\sqrt{2}} \left\{ \left[\frac{x + iy}{\sqrt{2}} f(r) + \frac{x - iy}{\sqrt{2}} f(r) \right] \right\} \qquad (3.64)$$

so that the expectation value for L_z should be found from the following integral which we

48

Table 3.3: A table showing the effective Bohr magnetons for various configurations of the $3d$ transition metal ions.

Ion	Config-uration	Basic Level	$p(\text{calc}) = g[j(j+1)]^{1/2}$	$p(\text{calc}) = 2[s(s+1)]^{1/2}$	$p(\text{exp})^a$
Ti^{3+}, V^{4+}	$3d^1$	$^2D_{3/2}$	1.55	1.73	1.8
V^{3+}	$3d^2$	$^3F_2$	1.63	2.83	2.8
Cr^{3+}, V^{2+}	$3d^3$	$^4F_{3/2}$	0.77	3.87	3.8
Mn^{3+}, Cr^{2+}	$3d^4$	$^5D_0$	0.00	4.90	4.9
Fe^{3+}, Mn^{2+}	$3d^5$	$^6S_{5/2}$	5.92	5.92	5.9
Fe^{2+}	$3d^6$	$^5D_4$	6.70	4.90	5.4
Co^{2+}	$3d^7$	$^4F_{9/2}$	6.63	3.87	4.8
Ni^{2+}	$3d^8$	$^3F_4$	5.59	2.83	3.2
Cu^{2+}	$3d^9$	$^2D_{5/2}$	3.55	1.73	1.9

^{a} Representative values

show below goes to zero

$$\int d^3r \; x f(r) L_z \; x f(r) = 0. \tag{3.65}$$

More generally, using time inversion symmmetry we see that, if the ground state eigenfunction is real, then L_z is given by

$$L_z = \left(\frac{\hbar}{i}\right)\left[\left(x\frac{\partial}{\partial y}\right) - \left(y\frac{\partial}{\partial x}\right)\right], \tag{3.66}$$

so that the expectation values for L_z becomes

$$\langle\psi_0|L_z|\psi_0\rangle = \int \psi_0^* \left(\frac{\hbar}{i}\right)\left[\left(x\frac{\partial}{\partial y}\right) - \left(y\frac{\partial}{\partial x}\right)\right]\psi_0 \; d^3r. \tag{3.67}$$

For a ground state wave function ψ_0 that is real,

$$\langle L_z\rangle = \frac{\hbar}{i}\int \psi_0 \left[\left(x\frac{\partial}{\partial y}\right) - \left(y\frac{\partial}{\partial x}\right)\right]\psi_0 \; d^3r \tag{3.68}$$

which implies that $\langle L_z\rangle$ is pure imaginary. But $\langle L_z\rangle$ is an observable, so that $\langle L_z\rangle$ must be real. Hence $\langle L_z\rangle \equiv 0$ for the case of cubic symmetry. Similar arguments follow for crystals with other symmetries.

The quenching of the orbital angular momentum is important in the limit where the crystal field is large compared with the spin–orbit interaction. In this case, we continue to label states in the $|\ell, s, m_\ell, m_s\rangle$ representation so that the magnetic moment $(\vec{L}+2\vec{S})$ yields an eigenvalue $(m_\ell + 2m_s)$. With the quenching of $\vec{L}$, we eliminate $\vec{L}$ from the problem and take $\vec{J} = \vec{S}$. This seems to be a good approximation for the transition metal ions, especially those with less than a half-filled $3d$ shell, as shown in Table 3.3. Only partial quenching of $\vec{L}$ occurs experimentally for more than half-filled $3d$ shells. When the orbital angular momentum is quenched, then the effective paramagnetic moment is $p = 2\sqrt{s(s+1)}$ and we can forget about $\vec{L}$ in calculating both the Landé g–factor and the total angular momentum, consistent with the results in Table 3.3.

49

Chapter 4

Paramagnetism and Diamagnetism of Nearly Free Electrons

References

- Ashcroft and Mermin, *Solid State Physics*, pp. 661-664, and Chapter 14.

- Kittel, *Introduction to Solid State Physics*, 6th Ed., pp. 239–249 and 413–416.

4.1 Introduction

In Chapter 3 we considered the diamagnetism and paramagnetism of bound electrons associated with the core electrons in crystalline materials. In the present chapter, we treat the paramagnetism of conduction electrons (Pauli paramagnetism) and also consider the diamagnetism (Landau diamagnetism) of the s and p nearly free electrons in metals and semiconductors. In addition we devote considerable attention to the discussion of the energy levels of conduction electrons in a magnetic field, also known as Landau levels.

4.2 Pauli Paramagnetism

We have previously discussed the response of bound electrons to a magnetic field. We first show in this section that the Curie law for bound electrons has the wrong temperature dependence for describing the paramagnetic response of conduction electrons in a magnetic field. We then indicate the new physics that must be introduced to handle the behavior of the conduction electrons, and show that by taking into account the Fermi statistics, the proper temperature dependence is obtained.

For the bound electrons, the paramagnetic susceptibility in a weak field is given by the Curie law:

$$\chi = \frac{n\hat{\mu}g^2\mu_B^2 j(j+1)}{3k_BT} \tag{4.1}$$

where n is the carrier density and $\hat{\mu}$ is the permeability in the constitutive equation $B = \hat{\mu}H$. Free electrons have no orbital angular momentum, but only spin angular momentum so that

$j = s = 1/2$ and $g = 2$. Therefore we obtain

$$g^2 j(j+1) = 2^2 \left(\frac{1}{2}\right)\left(\frac{3}{2}\right) = 3,$$

and we would expect the Curie law for free electrons having a concentration n to be

$$\chi_{\text{free electrons}} = \frac{n\hat{\mu}\mu_B^2}{k_B T}. \tag{4.2}$$

Equation 4.2 suggests that the free electrons should contribute substantially to the susceptibility (for a simple metal like sodium) as the temperature is decreased. Instead, we find experimentally that $\chi_{\text{free electrons}}$ is small in magnitude and nearly independent of temperature. The reason for this discrepancy is simply that we need to use Fermi statistics to treat free electrons and not Maxwell–Boltzmann statistics which we used in the calculation of Curie's Law. In discussing the statistics for whole atomic systems, as was done in considering the paramagnetism of the bound electrons, Maxwell–Boltzmann statistics is the proper statistics to use since the quantum numbers of each atom are not correlated with those of other atoms.

We will now give two different derivations of the paramagnetic susceptibility of free electrons taking Fermi statistics into account. We will find this contribution to χ to be positive, and is called Pauli paramagnetism, in honor of the man who first explained this effect successfully.

The first "derivation" of the Pauli paramagnetic susceptibility is hand-waving. Although it can hardly qualify as a derivation, it nevertheless provides us with a very nice physical picture of Pauli paramagnetism. Suppose that the free electrons form as electron gas with all energy states occupied up to the Fermi level. Only those states near the Fermi surface can contribute to the susceptibility, for it is only those states which have unoccupied states nearby in energy. Thus, the fraction of electrons that can contribute to χ is on the order of T/T_F where the Fermi temperature T_F is related to the Fermi energy E_F through the Boltzmann constant k_B by $T_F = E_F/k_B$. This argument then indicates that the free electron density which is effective in contributing to χ is the fraction $n(T/T_F)$ so that

$$\chi_{\text{free electrons}} \simeq \frac{n\hat{\mu}\mu_B^2}{k_B T}\left(\frac{T}{T_F}\right) = \frac{n\hat{\mu}\mu_B^2}{k_B T_F}. \tag{4.3}$$

Because $T_F \gg T$ for metals at room temperature, the Pauli paramagnetism is expected to be small compared with the contribution from the bound electrons and χ is essentially independent of T in agreement with experiment.

We will now give a second derivation of this result that is still quite physical, but somewhat more rigorous than the hand-waving approach. The second derivation given here is the basis for many arguments you will see in the literature in the field of magnetism, and is based on a density of states picture for spin-up and spin-down bands as shown in Fig. 4.1. The arrows on this diagram refer to the directions of the magnetic moments. The spin angular momentum $\vec{S}$ has a direction opposite to $\vec{\mu}$. To see the familiar density of states curve for nearly free electrons in 3D space $\rho(E) \propto E^{1/2}$, hold Fig. 4.1 on its side. This figure shows that the total occupation for the spin-up and spin-down states is different, but the occupation in both cases is terminated at the same Fermi energy. If we were thinking
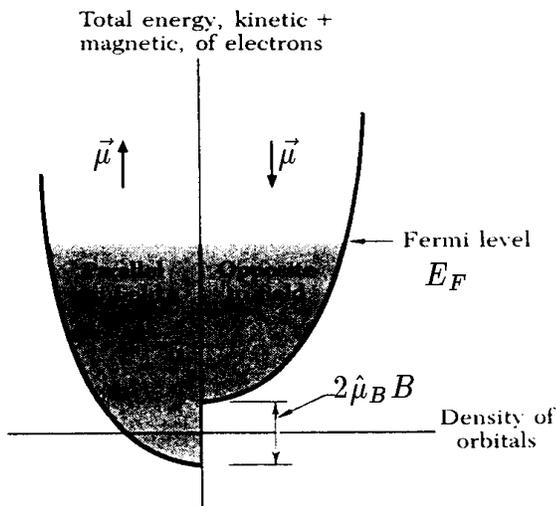
Figure 4.1: Pauli paramagnetism at 0 K, the levels below E_F are occupied. The number of electrons in the "up" and "down" bands will adjust to make the energies equal at the Fermi level. We use the notation $\hat{\mu}_B = |\mu_B|$ to take account of the fact that μ_B is a negative quantity due to the negative charge on the electron.

of electrons in a solid, we would call the two sides of the picture spin-up and spin-down bands. In Fig. 4.1 the energy E at the band edge is either $\pm\mu_B B$ relative to the energy in zero magnetic field. Thus, the electrons with spin along the magnetic field go into the $\downarrow$ band on the right hand side of the figure, while the electrons with $\vec{S}$ antiparallel to $\vec{B}$ go into the band on the left hand side of Fig. 4.1.

Let us now calculate the average number of electrons in the spin up and spin down bands. This average number will be roughly half of the total carrier concentration n. In carrying out the calculation we note that because of the negative sign of the electron charge, μ_B is a negative quantity. We therefore use $\hat{\mu}_B$ to denote the absolute value $|\mu_B|$. Then we write

$$n_+ = \frac{1}{2} \int_{-\hat{\mu}_B B}^{E_F} dE \; f(E) \; \rho(E + \hat{\mu}_B B) \tag{4.4}$$

where n_+ is the electron density with the magnetic moment directed along the field, $f(E)$ is the Fermi function, and $\rho(E + \hat{\mu}_B B)$ is the density of states for the ensemble for which the magnetic moment is directed along the magnetic field (see Fig. 4.1). To carry out the integral in Eq. 4.4, expand the density of states

$$\rho(E + \hat{\mu}_B B) = \rho(E) + \hat{\mu}_B B(\partial\rho(E)/\partial E) + \cdots. \tag{4.5}$$

Then upon substitution of Eq. 4.5 into Eq. 4.4 we obtain

$$n_+ = \frac{1}{2} \int_0^\infty dE \; f(E)\rho(E) + \frac{1}{2} \int_{-\hat{\mu}_B B}^0 dE \; f(E)\rho(E) + \frac{(\hat{\mu}_B B)}{2} \int_{-\hat{\mu}_B B}^\infty dE \; f(E)\rho'(E). \tag{4.6}$$

The second term on the right hand side of Eq. 4.6 vanishes because $\rho(E) = 0$ for $E < 0$. The last term on the right hand side of Eq. 4.6 is handled through integration by parts:

$$\int_{-\hat{\mu}_B B}^\infty dE \; f(E) \; \rho'(E) = f(E)\rho(E)|_{-\hat{\mu}_B B}^\infty - \int_{-\hat{\mu}_B B}^\infty dE \; f'(E)\rho(E). \tag{4.7}$$

The first term in Eq. 4.7 vanishes at both limits, since $\rho(E)$ vanishes at the lower limit where $E = -\hat{\mu}_B B < 0$, and $f(E)$ vanishes at the upper limit $E \to \infty$. The second term in Eq. 4.7 selects the density of states at the Fermi level because of the delta function properties of $f'(E) = -\delta(E - E_F)$, and we therefore obtain:

$$n_+ = (\frac{1}{2})n_0 + (\frac{1}{2})\hat{\mu}_B B\rho(E_F). \tag{4.8}$$

52

Similarly, we can carry out the corresponding calculation for n_- to obtain

$$n_- = \frac{1}{2} \int_{+\hat{\mu}_B B}^{\infty} dE \; f(E) \; \rho(E - \hat{\mu}_B B) = (\frac{1}{2})n_0 - (\frac{1}{2})\hat{\mu}_B B \rho(E_F). \tag{4.9}$$

The magnetic moment per unit volume is proportional to the net number of electrons contributing to the magnetic moment times $\hat{\mu}_B$, and can be written as

$$M = \hat{\mu}_B(n_+ - n_-) = \mu_B^2 B \rho(E_F) \tag{4.10}$$

so that

$$\chi = \mu_B^2 \rho(E_F). \tag{4.11}$$

We note that since χ depends on the square of μ_B, there is no distinction between $\hat{\mu}_B^2$ and μ_B^2. It is to be noted that the derivation for χ given here does not take into account the effect of the magnetic field on the electronic states. This effect is, in fact, of significant importance but beyond the scope of the simple discussion presented here.

For free electrons we can easily evaluate the density of states at the Fermi level $\rho(E_F)$ to obtain

$$\rho(E_F) = (3/2)\frac{n}{E_F} = \frac{3n}{2k_B T_F} \tag{4.12}$$

so that

$$M = (3/2)\frac{n\mu_B^2 B}{k_B T_F} \tag{4.13}$$

from which we obtain

$$\chi = (3/2)\frac{n\hat{\mu}\mu_B^2}{k_B T_F} \tag{4.14}$$

which except for the numerical factor is the same result as was obtained by the hand-waving approach given by Eq. 4.3 in the first "derivation" of the Pauli paramagnetic susceptibility. Measurements of the Pauli paramagnetic contribution are difficult to carry out and interpret because of difficulties in separating the various physical contributions to the experimentally determined $\chi(T)$. The most effective method to measure the Pauli contribution is a comparison between the susceptibilities implied by electron spin resonance and nuclear magnetic resonance.

4.3 Introduction to Landau Diamagnetism

The orbital motion of the nearly free electrons in a magnetic field gives rise to diamagnetism. The magnetic energy levels associated with this diamagnetism are called Landau levels and the diamagnetism is called Landau diamagnetism, named after the famous Russian physicist Lev Davidovich Landau, who first studied this phenomenon theoretically back in 1930.

In this chapter we discuss the fundamental properties associated with the Landau levels insofar as they determine Landau diamagnetism. Since the Landau levels imply a variety of magneto-oscillatory phenomena which are important for studies of the Fermi surface for crystalline solids, these topics are discussed in Chapter 5, while in Chapter 6 we discuss magnetic effects in the quantized 2D electron gas which have recently become important because of quantum wells and superlattices. In our discussion of the diamagnetism associated with nearly free electrons, we will first discuss the magnetic energy levels (or Landau levels)

which form the basis for Landau diamagnetism. The discussion starts with a derivation of the basic equations for a free electron system, and then proceeds to discuss electrons in simple parabolic bands for 3D materials.

4.4 Quantized Magnetic Energy Levels in 3D

The Hamiltonian for a free electron in a magnetic field uses the basic Schrödinger equation

$$\left[\frac{(\vec{p} - (e/c)\vec{A})^2}{2m} - \vec{\mu} \cdot \vec{B}\right]\psi = E\psi \qquad (4.15)$$

in which the square on the first term implies the scalar product of each of the factors $[\vec{p} - (e/c)\vec{A}]$. To represent a magnetic field along the z axis, we choose the asymmetric gauge (Landau gauge) for the vector potential $\vec{A}$:

$$A_x = -By$$

$$A_y = 0 \qquad (4.16)$$

$$A_z = 0$$

and we note that $\vec{\mu}$ in Eq. 4.15 is the magnetic moment associated with the electron spin, where $\vec{\mu} = g_s \mu_B \vec{S}/\hbar$.

Since the only coordinate in the problem (Eqs. 4.15 and 4.16) is y, the form of $\psi(x, y, z)$ in Eq. 4.15 is chosen to make the differential equation separable into plane wave motion in the x and z directions. The wave function $\psi(x, y, z)$ is thus written as

$$\psi(x, y, z) = e^{ik_x x} e^{ik_z z} \phi(y). \qquad (4.17)$$

Substitution of Eq. 4.17 in Eq. 4.15 results in the expression

$$\left[\frac{(\hbar k_x + (e/c)By)^2}{2m} + \frac{p_y^2}{2m} + \frac{\hbar^2 k_z^2}{2m} - \frac{g_s \mu_B}{\hbar}\vec{S} \cdot \vec{B}\right]\phi(y) = E\phi(y) \qquad (4.18)$$

where g_s and μ_B are, respectively, the free electron g–factor ($g_s = 2.0023$) and the Bohr magneton $\mu_B = e\hbar/(2mc)$. We see immediately that the orbital portion of Eq. 4.18 is of the form of the harmonic oscillator equation

$$\left[\frac{p_x^2}{2m} + \frac{1}{2}mx^2\omega_c^2\right]\psi_{\text{H.O.}}^{(\ell)} = E_\ell \psi_{\text{H.O.}}^{(\ell)}. \qquad (4.19)$$

where $\psi_{\text{H.O.}}^{(\ell)}$ is a harmonic oscillator function and $E_\ell = \hbar\omega_c(\ell + 1/2)$ are the harmonic oscillator eigenvalues in which ℓ is an integer, $\ell = 0, 1, \ldots$. A comparison of Eq. 4.18 with the harmonic oscillator equation Eq. 4.19 shows that the characteristic frequency for the harmonic oscillator is the cyclotron frequency $\omega_c = eB/(mc)$ and the harmonic oscillator is centered about

$$y_0 = -\frac{\hbar k_x}{m\omega_c}. \qquad (4.20)$$

54

These identifications yield the harmonic oscillator equation

$$\left[\frac{p_y^2}{2m} + \frac{\omega_c^2}{2m}(y - y_0)^2 + \frac{\hbar^2 k_z^2}{2m} - \frac{g_s \mu_B}{\hbar} \vec{S} \cdot \vec{B} \right] \phi(y) = E\phi(y). \tag{4.21}$$

Thus, the energy eigenvalues of Eq. 4.21 for a free electron in a magnetic field can be written down immediately as

$$E_{\ell,m_s}(k_z) = \frac{\hbar^2 k_z^2}{2m} + \hbar\omega_c(\ell + \frac{1}{2}) - g_s \mu_B m_s B \tag{4.22}$$

recognizing that in the direction parallel to $\vec{B}$ we have plane wave motion, since there is no force acting along $\vec{B}$, and in the plane perpendicular to $\vec{B}$ we have harmonic oscillator motion. The last term in Eq. 4.22 gives the contribution from spin terms with spin up corresponding to $m_s = 1/2$ and spin down corresponding to $m_s = -1/2$.

For a band electron in a solid, the energy eigenvalues in a magnetic field are given in the "effective mass approximation" by an expression which is very similar to Eq. 4.22 except that the free electron mass is replaced by an effective mass tensor and the free electron g-factor $g_s = 2.0023$ is replaced by an effective g-factor g_{eff}. Thus Landau levels for carriers in a simple parabolic band in a semiconductor are given by

$$E_{\ell,m_s}(k_z) = \frac{\hbar^2 k_z^2}{2m_{\parallel}^*} + \hbar\omega_c^*(\ell + \frac{1}{2}) - g_{\text{eff}}\mu_B m_s B \tag{4.23}$$

where the various band parameters in Eq. 4.23 are defined as follows: $m_{\parallel}^*$ is the effective mass tensor component along the magnetic field, $\omega_c^* = eB/(m_c^* c)$ is the cyclotron frequency, m_c^* is the cyclotron effective mass for motion in the plane normal to the magnetic field, and g_{eff} is the effective g–factor.

The quantum numbers describing the energy eigenvalues $E_{\ell,m_s}(k_z)$ are as follows:

1. ℓ is the Landau level index (or harmonic oscillator level index), $\ell = 0, 1, 2, 3, \ldots$.

2. m_s is the spin quantum number, $1/2$ for $\uparrow$ and $-1/2$ for $\downarrow$.

3. k_z assumes values between $-\infty$ and $+\infty$ in free space and is a quasi-continuous variable in the first Brillouin zone for a real solid.

4. k_x is the wave vector in the plane $\perp$ to $\vec{B}$ and does not enter into Eq. 4.23 for the energy levels.

Since the magnetic energy levels $E_{\ell,m_s}(k_z)$ are independent of k_x, the quantum number k_x contributes directly to the density of states in a magnetic field. This degeneracy factor is discussed in §4.4.1. The form of $E_{\ell,m_s}(k_z)$ is then discussed in §4.4.2 and finally the effective mass parameters $m_{\parallel}^*$ and m_c^* and the effective g-factor are discussed in §4.4.3.

4.4.1 Degeneracy of the Magnetic Energy Levels in k_x

The degeneracy of the magnetic energy levels $E_{\ell,m_s}(k_z)$ in k_x is found by considering the center of the harmonic oscillator function, which from Eq. 4.20 is at $y_0 = -\hbar k_x/(m\omega_c)$. Since y_0 lies in the interval

$$-L_y/2 < y_0 < L_y/2, \tag{4.24}$$

and since the center of the harmonic oscillator is inside the sample, we have the requirement

$$-\frac{m\omega_c L_y}{2\hbar} < k_x < \frac{m\omega_c L_y}{2\hbar}. \tag{4.25}$$

Thus the limits on the range of the quantum number k_x are between $k_x^{\min}$ and $k_x^{\max}$ which are given by

$$k_x^{\min} = -m\omega_c L_y/2\hbar$$

$$\tag{4.26}$$

$$k_x^{\max} = m\omega_c L_y/2\hbar.$$

With the limits on k_z imposed by Eq. 4.26, the sum over states (using Fermi statistics) becomes

$$\mathcal{Z} = \sum_{\ell=0}^{\infty} \sum_{k_z=-\infty}^{\infty} \sum_{k_x=k_x^{\min}}^{k_x^{\max}} \sum_{m_s=-1/2}^{1/2} \ln\left(1 + e^{[E_F - E_{\ell,m_s}(k_z)]/k_B T}\right). \tag{4.27}$$

Since the energy levels are independent of k_x, we can sum Eq. 4.27 over k_x to obtain a degeneracy factor which is important in all magnetic energy level phenomena

$$\sum_{k_x} \rightarrow \int_{k_x^{\min}}^{k_x^{\max}} dk_x \frac{L_x}{2\pi} = \frac{L_x L_y m\omega_c}{2\pi\hbar} \tag{4.28}$$

utilizing the uncertainty principle which requires that there is one k_x state per $2\pi/L_x$ since $N_x a = L_x$, in which a is the lattice constant. It is important to emphasize that the sum over k_x in Eq. 4.28 is proportional to the magnetic field since $\omega_c \propto B$.

Referring to Fig. 4.2(d) we see how upon application of a magnetic field in the z direction the wave vector quantum numbers k_x and k_y in the plane normal to the magnetic field are transformed into the Landau level index ℓ and the quantum number k_x which has a high degeneracy factor per unit area of $(m\omega_c/h)$. It is convenient to introduce the characteristic magnetic length λ defined by

$$\lambda^2 \equiv \frac{\hbar c}{eB} \tag{4.29}$$

so that from Eq. 4.28 the degeneracy factor per unit area becomes $1/(2\pi\lambda^2)$.

From Fig. 4.2(d) we see a qualitative difference between the states in a magnetic field and the states in zero field. For fields too small to confine the carriers into a cyclotron orbit with a characteristic length less than λ, the electrons are best described in the zero field limit, or we can say that the Landau level description applies for magnetic fields large enough to define a cyclotron orbit within the sample dimensions and for electron relaxation times long enough for an electron not to be scattered before completing an electron orbit, $\omega_c \tau > 1$. We return to the discussion of this degeneracy factor in discussion the 2D electron gas in Chapter 6.

4.4.2   Dispersion of the Magnetic Energy Levels Along the Magnetic Field

The dispersion of the magnetic energy levels is given by Eq. 4.23 and is displayed in Fig. 4.2(a). In this figure it is seen that the dispersion relations $E_{\ell,m_s}(k_z)$ are parabolic in k_z for each Landau level, each level ℓ being displaced from levels $\ell+1$ and $\ell-1$ by the Landau level separation $\hbar\omega_c$. The lowest Landau level ($\ell = 0$) is at an energy $(\hbar\omega_c/2)$ above the
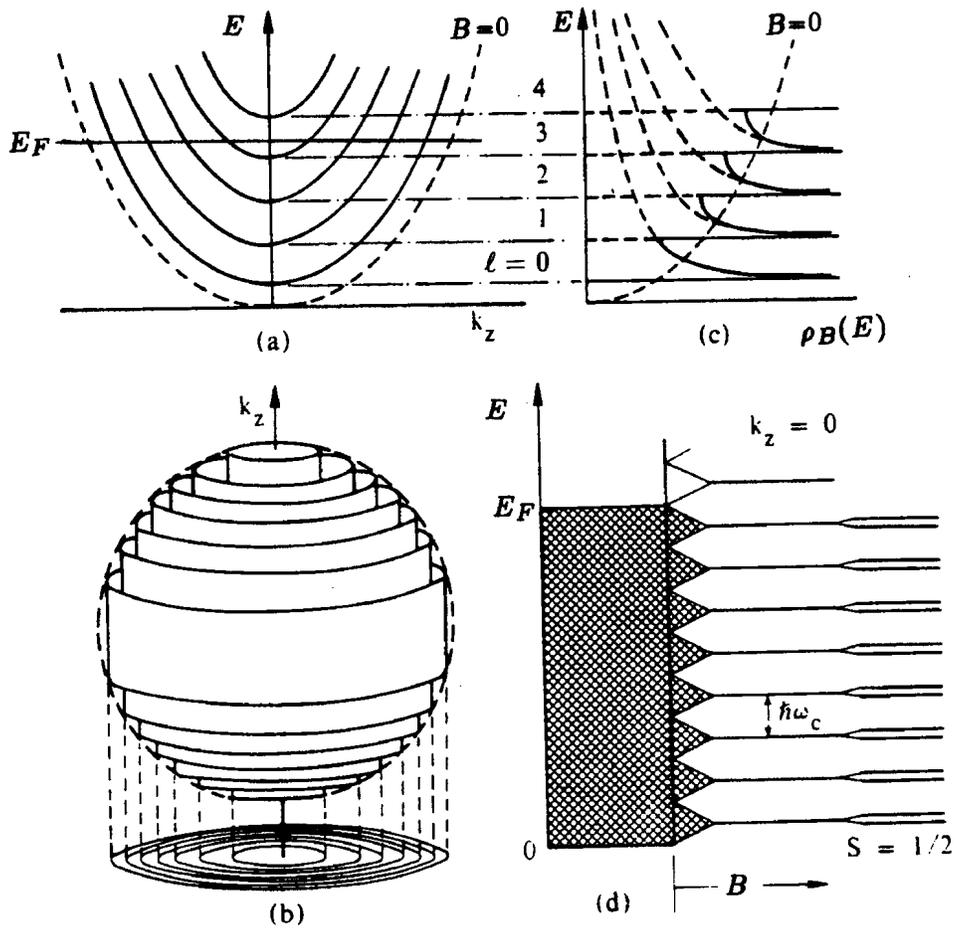
Figure 4.2: Various aspects of Landau levels. (a) E vs k_z for the first few Landau levels $\ell = 0, 1, \ldots, 4$. The $B = 0$ parabola (dashed curve) refers to the ordinary free electron case with zero magnetic field. (b) k–space showing Landau levels in 3D. The allowed k-values lie on the concentric cylinders, and the spherical Fermi surface cuts these cylinders. (c) The solid line is the density of states for all the Landau levels while the dashed-solid curves give the density of states in a magnetic field for each of the Landau levels. Singularities in the density of states occur whenever a Landau level pops through the Fermi level. The dashed curve labeled $B = 0$ refers to the density of states in zero field, and shows the expected $\sqrt{E}$ dependence. (d) A schematic diagram showing how the states in zero field go into Landau levels when the B field is applied. The diagram also shows the effect of electron-spin splitting on the Landau levels.

57

energy of electrons in zero magnetic field. The occupation of each Landau level is found by integration up to the Fermi level E_F. Figure 4.2(b) shows special k_z values where either a Landau level crosses the Fermi level or a Landau level pops through the Fermi level E_F. As the magnetic field increases the Landau level separation increases until a Landau level pops through E_F, requiring a redistribution of electrons through the remaining Landau levels.

In this section we focus on the k_z dependence of the magnetic energy levels. First we obtain the sum of the number density over k_z which involves conversion of the sum on states to an integral

$$\sum_{k_z} \to 2 \int_0^\infty dk_z \frac{L_z}{2\pi}. \tag{4.30}$$

Using Fermi statistics we then obtain for the number density:

$$
\begin{aligned}
n(L_x, L_y, L_z) =\ & \sum_{\text{states}} \frac{1}{1+e^{(E_{\ell,m_s}(k_z)-E_F)/k_B T}} \\
=\ & \frac{L_x L_y m \omega_c}{2\pi \hbar} \frac{2L_z}{2\pi} \sum_{\ell,m_s} \int_0^\infty dk_z \frac{1}{1+e^{(E_{\ell,m_s}(k_z)-E_F)/k_B T}},
\end{aligned} \tag{4.31}
$$

so that the degeneracy factor per unit volume is $(1/2\pi^2\lambda^2)$.

Keeping the Fermi level constant, the electron density is found by summing the Fermi distribution over all states in the magnetic field, where the Fermi function

$$f(E_{\ell,m_s}(k_z)) = \frac{1}{1 + e^{(E_{\ell,m_s}(k_z)-E_F)/k_B T}} \tag{4.32}$$

gives the probability that the state (ℓ, m_s, k_z) is occupied. In a magnetic field, the 3D electron density n of a nearly free electron solid (neglecting spin splitting effects) is

$$n = \frac{2eB}{(2\pi)^2 \hbar c} \sum_{\ell=0}^{\ell_{\max}} \int_{-\pi/a}^{\pi/a} dk_z f(E_{\ell,m_s}(k_z)) \tag{4.33}$$

in which a factor of 2 for the electron spin degeneracy has been inserted.

For simplicity, we further consider the magnetic energy levels for a simple 3D parabolic band (neglecting spin)

$$E_\ell(k_z) = \frac{\hbar^2 k_z^2}{2m^*} + \hbar\omega_c^*(\ell + 1/2) \tag{4.34}$$

so that

$$k_z = \left(\frac{2eB}{c\hbar}\right)^{1/2} \left[\frac{E}{\hbar\omega_c^*} - (\ell + 1/2)\right]^{1/2} \tag{4.35}$$

where we have written E to denote $E_\ell(k_z)$. Differentiating Eq. 4.35 gives

$$dk_z = \left(\frac{2eB}{c\hbar}\right)^{1/2} \frac{dE}{2\hbar\omega_c^*} \left[\frac{E}{\hbar\omega_c^*} - (\ell + 1/2)\right]^{-1/2}. \tag{4.36}$$

For the case of a 2D electron gas, the electrons are confined in the z direction and exhibit bound states. Thus no integration over k_z (see Eq. 4.33) is needed for a 2D electron gas. However, for the 3D electron gas, integration of Eq. 4.33 thus yields a carrier density at $T = 0$ of

$$n = \frac{1}{\pi^2\lambda^2} \sum_{\ell=0}^{\ell_F} \int_{E(k_z=0)}^{E_F} \left(\frac{2eB}{c\hbar}\right)^{1/2} \frac{dE}{2\hbar\omega_c^*} \left[\frac{E}{\hbar\omega_c^*} - (\ell + 1/2)\right]^{-1/2} \tag{4.37}$$

where the characteristic magnetic length λ is given by Eq. 4.29. Carrying out the integration in Eq. 4.37, we obtain the result

$$n = \frac{1}{\pi^2 \lambda^2} \sum_{\ell=0}^{\ell_F} \left(\frac{2eB}{c\hbar}\right)^{1/2} \left[\frac{E_F}{\hbar\omega_c^*} - (\ell + 1/2)\right]^{1/2} \tag{4.38}$$

where ℓ_F is the highest occupied Landau level. The oscillatory effects associated with Eq. 4.38 are discussed in Chapter 5.

From differentiation of Eq. 4.38 with respect to energy, we obtain the density of states in a magnetic field $\rho_B(E) = (\partial n / \partial E)$

$$\rho_B(E) = \frac{\sqrt{2eB/\hbar c)}}{2\pi^2 \hbar \omega_c^* (\hbar c/eB)} \sum_{\ell} \left[\frac{E}{\hbar\omega_c^*} - (\ell + 1/2)\right]^{-1/2} \tag{4.39}$$

which is plotted in Fig. 4.2c, showing singularities at each magnetic subband extrema. Because of the singular behavior of physical quantities associated with these extrema, the subband extrema contribute resonantly to magneto-optical spectra, as discussed in Chapter 5.

To illustrate the oscillatory behavior of Eq. 4.38 in $1/B$, we write Eq. 4.38 as the sum over Landau levels and can be written as

$$n = \frac{\sqrt{2}}{\pi^2 \lambda^3} \sum_{\ell=0}^{\ell_F} \left(\ell_F' - \ell\right)^{1/2} \tag{4.40}$$

and the resonance condition is

$$\ell_F' = \frac{E_F}{\hbar\omega_c^*} - \frac{1}{2} \tag{4.41}$$

gives a measure of the occupation level as is illustrated in Fig. 4.2a. The oscillatory behavior of n and other physical observables is the subject of Chapter 5.

4.4.3 Band Parameters Describing the Magnetic Energy Levels

The magnetic energy levels given by Eq. 4.23 depend on several band parameters $m_\parallel^*$, m_c^* and g_{eff}. In this section we summarize the properties of these band parameters. To observe the effects associated with the Landau levels we require that $\omega_c \tau \gg 1$, which implies that an electron can execute at least one cyclotron orbit before being scattered. Because of the small effective masses of carriers in semiconductors, the cyclotron frequency is high, and the spacing between magnetic energy levels also becomes large in comparison to free electrons.

The effective mass parameters $m_\parallel^*$ and m_c^* which enter Eq. 4.23 can be simply written for semiconductors because of the simplicity of their Fermi surfaces. For arbitrary magnetic field directions, it is often convenient to use the formula

$$m_c^* = \left(\frac{\det[\overleftrightarrow{m}^*]}{\hat{b} \cdot \overleftrightarrow{m}^* \cdot \hat{b}}\right)^{1/2} \tag{4.42}$$

to find the cyclotron effective mass m_c^* for an ellipsoidal constant energy surface, where $\det[\overleftrightarrow{m}^*]$ is the determinant of the effective mass tensor $\overleftrightarrow{m}^*$ and $\hat{b}$ is a unit vector in the direction of the magnetic field so that

$$m_\parallel^* = \hat{b} \cdot \overleftrightarrow{m}^* \cdot \hat{b}. \tag{4.43}$$

Figure 4.3: Simplified view of the band edge structure of a direct gap semiconductor, e.g., GaAs at $\vec{k} = 0$. Note that the spin-orbit splitting in the valence band is nearly as large as the bandgap.
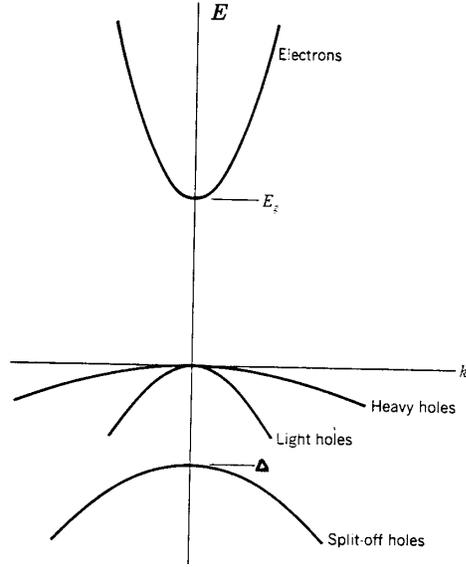
Equations 4.42 and 4.43 are particularly useful when the constant energy ellipsoidal surface does not have its major axes along the crystalline axes and the magnetic field is arbitrarily directed with respect to the major axes of the ellipsoidal constant energy surface. For ellipsoidal constant energy surfaces, neither $m_\parallel^*$ nor m_c^* depend on k_z. For more general Fermi surfaces, m_c^* is found by integration of $k/(\partial E/\partial k)$ around a constant energy surface normal to the magnetic field and m_c^* will depend on k_z in general. The effective mass component along the magnetic field $m_\parallel^*$ is unaffected by the applied field.

The calculation of g_{eff} is more complicated than for the effective mass components, and makes considerable use of group theory to handle symmetry phenomena. Therefore we will treat g_{eff} as an experimentally determined band parameter.

In materials with large spin–orbit coupling (see Fig. 4.3) the effective g–factor, g_{eff}, is found experimentally to be quite different from the free electron value of 2 and g_{eff} can be either positive or negative. For example, for the conduction band of InSb, $g_{\mathrm{eff}} \simeq -50$ and the cyclotron effective mass for the electron carriers is small ($m_c^* \simeq 0.014m$) and isotropic. The extremum ($k_z = 0$) of each magnetic sub-band (indexed by the quantum number $\ell =$ integer) is indicated in Fig. 5.2. For the case of InSb, the lowest magnetic energy level is a spin $\uparrow$ state, with the spin oriented along the magnetic field due to the negative effective g-factor of InSb. This negative g-factor arises because of the large orbital contribution to the g-factor which can occur in solids with a large spin-orbit interaction, an effect that is totally absent in atomic systems.

60

4.5 The Magnetic Susceptibility for Conduction Electrons

Having obtained the magnetic energy levels for the conduction electrons, we can then use statistical mechanics to obtain the magnetization per unit volume using

$$M = +\frac{k_B T}{V}\frac{\partial \ln \mathcal{Z}}{\partial H} \qquad (4.44)$$

where the partition function $\mathcal{Z}$ for the conduction electrons is given by Eq. 4.27 and the magnetic susceptibility is given by $\chi = \partial M/\partial H$.

Most interest in studies of the magnetic susceptibility has focussed on the magneto-oscillatory phenomena exhibited by the partition function $\mathcal{Z}$ as is further discussed in Chapter 5.

Chapter 5

Magneto-Oscillatory and Other Effects Associated with Landau Levels

References

- Ashcroft and Mermin, *Solid State Physics*, Ch. 14.

- Kittel, *Introduction to Solid State Physics*, 6th Ed., pp. 239–249.

5.1 Overview of Landau Level Effects

Studies of the density of states in a magnetic field and intraband (cyclotron resonance) and interband transitions between magnetic energy levels provide three of the most informative techniques for study of the constant energy surfaces, Fermi surfaces, and effective mass parameters in solid state physics:

1. The de Haas–van Alphen effect and the other related magneto-oscillatory effects provide the main method for studying the shape of the constant energy surfaces of semiconductors and metals. This is the main focus of this chapter.

2. Cyclotron resonance (see Fig. 5.1) gives values for the effective mass tensor components by measurement of the transition between adjacent magnetic energy levels in a single band (intraband transitions)

$$\hbar\omega_c^* = E_\ell - E_{\ell-1} \tag{5.1}$$

where the cyclotron frequency for a carrier orbit normal to the magnetic field is given by $\omega_c^* = eB/(m_c^* c)$ and E_ℓ denotes a Landau level with Landau level index ℓ. The magnetic energy level structure for two simple parabolic bands shown in Fig. 5.2 can be interpreted as the Landau level subbands for the valence and conduction bands for a model semiconductor. The dispersion of the energy levels along k_z discussed in Chapter 4

$$E_{\ell,m_s}(k_z) = \frac{\hbar^2 k_z^2}{2m} + \hbar\omega_c(\ell + \frac{1}{2}) - g_s\mu_B m_s B \tag{5.2}$$
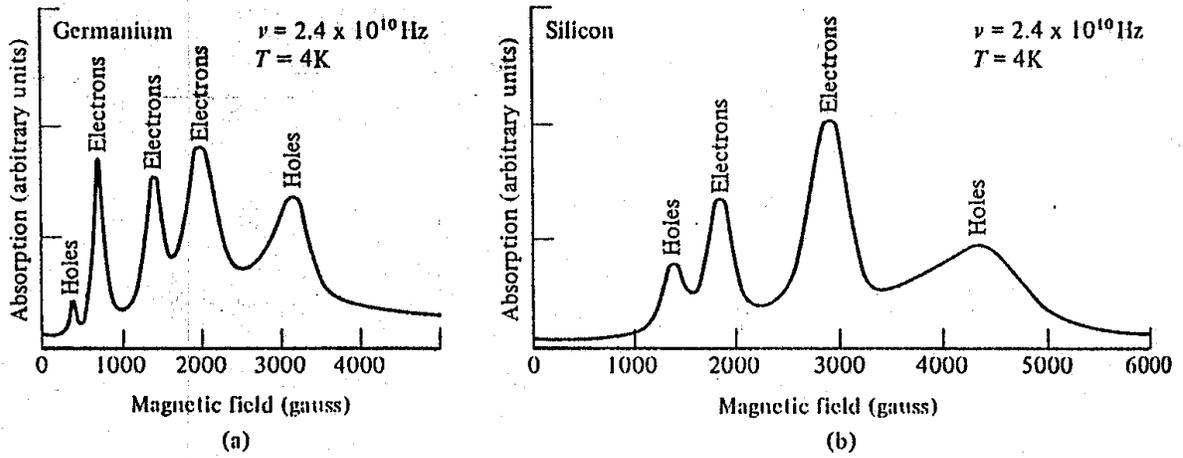
Figure 5.1: Typical cyclotron resonance signals in (a) germanium and (b) silicon. The magnetic field lies in a (110) plane and makes an angle with the [001] axis of 60° for the spectrum shown for Ge and 30° for the spectrum shown for Si. (From G. Dresselhaus, et al., Phys. Rev. 98, 368 (1955).)

is shown in Fig. 5.2 for each magnetic subband ℓ for a given spin state m_s. As shown in Fig. 5.1, cyclotron resonance experiments can be carried out on both the electron and hole carrier pockets of semiconductors. Electrons and holes correspond to the two different circularly polarizations of the microwave excitation radiation. Because of the different band curvatures and effective masses associated with the various carrier types in metals and semiconductors, $\hbar\omega_c^*$ will be in resonance with $\hbar\omega$ of the resonant microwave cavity at different magnetic field values. The optical selection for these intraband (cyclotron resonance) transitions is $\Delta\ell = \pm 1$. By varying the magnetic field direction relative to the crystal axes, the corresponding cyclotron effective masses can be determined, thereby giving the effective mass tensors for electrons and/or holes.

3. Interband Landau level transitions (see Fig. 5.2) occur when the optical frequency is equal to the separation between the extrema ($k_z = 0$) of the Landau levels ℓ and ℓ'

$$\hbar\omega = E_{\ell,c} - E_{\ell',v} = E_g + \hbar\omega_{c,c}^*(\ell + 1/2) + \hbar\omega_{c,v}^*(\ell' + 1/2). \qquad (5.3)$$

These interband transitions provide information on effective masses for the valence and conduction bands and the bandgaps between them. The optical selection rule for these interband transitions is $\Delta\ell = 0$. In Eq. 5.3 the subscripts v and c refer to the valence and conduction bands, respectively. Table 5.1 gives values for the effective masses for the conduction band m_e, and valence bands for heavy holes m_{hh} and light holes m_{lh} and for the split-off bands for several direct gap semiconductors, and data are included for the split-off band shown in Fig. 4.3.

In semiconductors it is relatively easy to observe quantum effects in a magnetic field because of the light mass, high mobility and long relaxation times of the carriers which make it easy to satisfy $\omega_c\tau \gg 1$, the requirement for observing quantum effects.

63
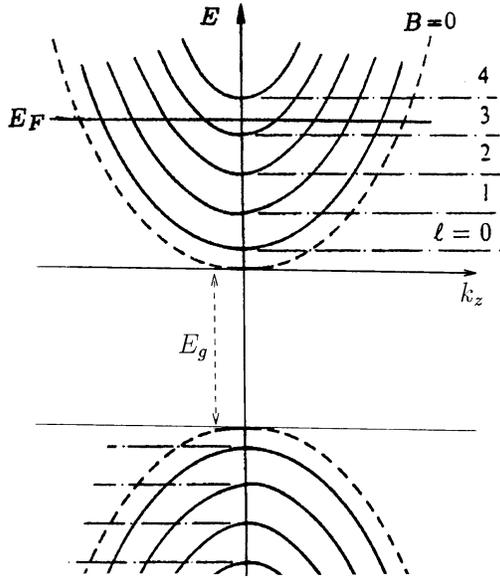
Figure 5.2: Magnetic energy levels for simple parabolic valence and conduction bands. Intraband cyclotron resonance and interband Landau level transitions occur between these magnetic energy levels. The dashed curves represent the energy dispersion relation in zero magnetic field. In this diagram the spin on the electron is neglected.

Table 5.1: Effective masses of electrons and holes in direct gap semiconductors.

Crystal	Electron m_e/m_0	Heavy Hole m_{hh}/m_0	Light Hole m_{lh}/m_0	Split-Off Hole m_{soh}/m_0	Spin-Orbit Δ (eV)	Gap E_g (eV)
InSb	0.015	0.39	0.021	(0.11)	0.82	0.23
InAs	0.026	0.41	0.025	(0.08)	0.43	0.43
InP	0.073	0.40	(0.078)	(0.15)	0.11	1.42
GaSb	0.047	0.30	0.06	(0.14)	0.80	0.81
GaAs	0.070	0.68	0.12	(0.20)	0.34	1.52

Figure 5.3: Schematic diagram of the extrema of the energy of the Landau levels for the quantum limit $\ell = 0, 1, 2, \ldots$ showing occupation of the two lowest magnetic sub-bands for $k_z = 0$. The parabola indicates the k_x (or k_y) dependence at $B = 0$.
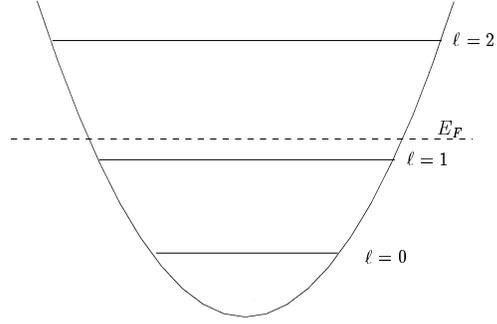
5.2   Quantum Oscillatory Magnetic Phenomena

Consider the magnetic energy levels such as those shown in Fig. 5.2 for a band electron in a solid. Assume, for example, that we have carriers in the conduction band and hence a Fermi level as indicated in Fig. 5.3 where we plot the parabolic $E(\vec{k})$ relation in zero magnetic field and indicate the energy of each magnetic sub-band extremum by its Landau level index. For each magnetic subband, the density of states is singular at its subband extremum and the resonances in the magneto-oscillatory experiments occur when an energy extremum is at the Fermi energy. Now imagine that we increase the magnetic field. The Landau level spacing is $\hbar\omega_c^* = \hbar eB/(m_c^* c)$ and is proportional to B. Thus as we increase B, we eventually reach a value B_ℓ for which the highest occupied Landau level ℓ crosses the Fermi level and the electrons that formerly were in this level must redistribute themselves among the lower levels below the Fermi level.

Assume for the moment that the Fermi level is independent of magnetic field, which is a good approximation when many Landau levels are occupied. We will now show that the passage of Landau levels through the Fermi level produces an oscillatory dependence of the electron density upon the reciprocal of the magnetic field.

Since many physical quantities depend on the density of states, these physical quantities will also exhibit an oscillatory dependence on $1/B$. Thus, this oscillatory dependence on $(1/B)$ is observed in a large class of observables such as the electrical resistivity (Shubnikov–de Haas effect), Hall effect, Seebeck coefficient, ultrasonic attention, velocity of sound, optical dielectric constant, relaxation time, temperature dependence (magnetothermal effect), magnetic susceptibility (the de Haas–van Alphen effect). We discuss below the oscillatory dependence of the carrier density on $1/B$ as representative of this whole class of magneto-oscillatory effects.

In order for the de Haas–van Alphen effect to be observable, we require that an electron complete an orbit before scattering. The time to complete an orbit is $2\pi/\omega_c^*$ and this time must be small compared with τ the average time between electron scattering events. Thus the condition for observing the de Haas–van Alphen effect is usually written as $\omega_c^* \tau \gg 1$. Thus the observation of magneto-oscillatory phenomena requires high magnetic fields (large ω_c) and low temperatures (long τ). Low temperatures are also necessary so that the Landau level separations can be large compared with thermal energies. Landau level separations generally are quite small in magnitude. For example, for $B = 10$ tesla or 100 kilogauss, and m equal to the free electron mass, the Landau level separation is $\sim 10^{-3}$ eV (or ~ 12K) which is to be compared with $k_B T$ at room temperature with an energy of 0.025

65

eV. Therefore it is desirable to carry out de Haas–van Alphen experiments in the vicinity of 1K. For simplicity, we will take $T = 0K$ in our simple discussion of magneto-oscillatory effects so that the Fermi function is 1 for $E < E_F$ (occupied states) and is 0 for $E > E_F$ (unoccupied states).

The oscillatory behavior of the electron density in a magnetic field can be understood from the following considerations. As we increase the magnetic field two things happen.

1. The density of states degeneracy associated with k_x increases because this degeneracy is proportional to B (see Eq. 4.28).

2. With increasing field B, the number of electrons in a magnetic energy level ℓ decreases as its magnetic energy level extremum approaches the Fermi level. This emptying of electrons from higher lying magnetic sub-bands is not a linear function of B. In particular, when a level crosses the Fermi level, the emptying of electron states is very rapid due to the high density of states at $k_z = 0$ (see Fig. 4.2c).

Consider, for example the emptying of the $\ell = 1$ Landau level as it passes through E_F, for increasing magnetic field. All electrons in this level must be emptied when the Landau level crosses E_F (see Fig. 5.3). We show below that the extrema in the Landau levels correspond to singularities in the density of states (see Fig. 4.2c). The 3D density of states in a magnetic field has a monotonic magnetic field-dependent background due to the degeneracy factor of Eq. 4.28 as well as a resonance at

$$E_F = \hbar\omega_c^*(\ell + 1/2) = \frac{\hbar e B_\ell}{m_c^* c}(\ell + 1/2) \qquad (5.4)$$

denoting the energy where a Landau level passes through the Fermi level. As B increases further, the magnetic energy levels tend to empty their states slowly just after the Landau level has passed through the Fermi level, and the monotonic linearly increasing degeneracy term (Eq. 4.28) dominates. The interplay of these two factors leads to oscillations in the density of states and consequently in all physical observables depending on the density of states. The resonance condition in the density of states in a magnetic field is given by Eq. 5.4 which defines the resonant magnetic field B_ℓ as the field where the E_ℓ Landau level passes through E_F. Making use of Eq. 5.4, we see that the resonances in the density of states (Eq. 4.39) are periodic in $1/B$ with a period defined by

$$\mathcal{P} \equiv \frac{1}{B_\ell} - \frac{1}{B_{\ell-1}} = \frac{e\hbar}{m_c^* E_F c}[(\ell + 1/2) - (\ell - 1/2)] = \frac{e\hbar}{m_c^* E_F c}. \qquad (5.5)$$

Equation 5.5 shows that the period $\mathcal{P}$ is independent of the quantum number (Landau level index) ℓ, but depends on the product $m_c^* E_F$. It turns out that the temperature dependence of the amplitude of the de Haas–van Alphen resonances depends on m_c^* so that one can thus measure both m_c^* and the product $m_c^* E_F$ through study of these magneto-oscillatory phenomena, thereby yielding E_F and m_c^* independently.

It is often convenient to discuss the de Haas–van Alphen effect in terms of cross–sectional areas of the Fermi surface. Since $E_F = \hbar^2 k_F^2/2m^*$ and $\mathcal{A} = \pi k_F^2$, we have $E_F = \hbar^2 \mathcal{A}/2\pi m^*$ and from Eq. 5.5 the de Haas–van Alphen period $\mathcal{P}$ becomes

$$\mathcal{P} = \frac{1}{B_\ell} - \frac{1}{B_{\ell-1}} = \frac{2\pi e}{c\hbar\mathcal{A}}. \qquad (5.6)$$

Figure 5.4: Fermi surface showing extremal cross–sectional areas. The indicated maximum and minimum areas would each show distinct de Haas–van Alphen periods. The larger cross section would have a shorter period.
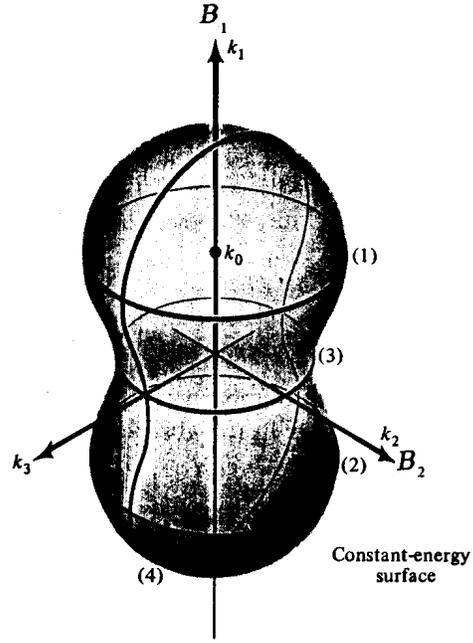
Equation 5.6 shows that the de Haas–van Alphen period $\mathcal{P}$ depends only on the Fermi surface cross sectional area $\mathcal{A}$ (see Fig. 5.4) except for universal constants. A more rigorous derivation of the de Haas–van Alphen period $\mathcal{P}$ shows that Eq. 5.6 is valid for an arbitrarily shaped Fermi surface and the area $\mathcal{A}$ that is associated with the resonance is the extremal cross-sectional area – either the maximum or minimum as illustrated in Fig. 5.4. A physical explanation for the dominance of the extremal cross section of the Fermi surface is that all cross sectional areas normal to the magnetic field contribute to the magneto-oscillatory effect, but upon integration over k_z, the cross-sections which do not vary with k_z (or vary very little with k_z) will contribute to the same de Haas–van Alphen period $\mathcal{P}$, while the non-extremal cross sections will each contribute to different values of $\mathcal{P}$ and therefore will not give a resonant oscillatory period. By varying the magnetic field orientation, different cross-sections will become extremal, and in this way the shape of the Fermi surface can be monitored. Ellipsoidal constant energy surfaces have only one extremal (maximum) cross-section and the cyclotron effective mass m_c^* is independent of k_z.

As an example of the de Haas–van Alphen effect in a real material, we see in Fig. 5.5a oscillations observed in silver with $\vec{B} \parallel (111)$ direction. In this figure we see oscillations with a long period as well as fast or short period oscillations. From the Fermi surface diagram in the extended Brillouin zone shown for silver in Fig. 5.5b, we identify the fast periods with the large Fermi surface cross sections associated with the belly orbits and the slow oscillations with the small cross sectional necks. From Fig. 5.5b, it is clear that the necks can be clearly observed only for the $\vec{B} \parallel (111)$ directions. However, the anisotropy of the belly orbit can be monitored by varying the orientation of $\vec{B}$.

Not only do the electrons execute orbits in reciprocal space, they also execute orbits in real space in the presence of a magnetic field. Because the length scales in real space

(a)   (b)
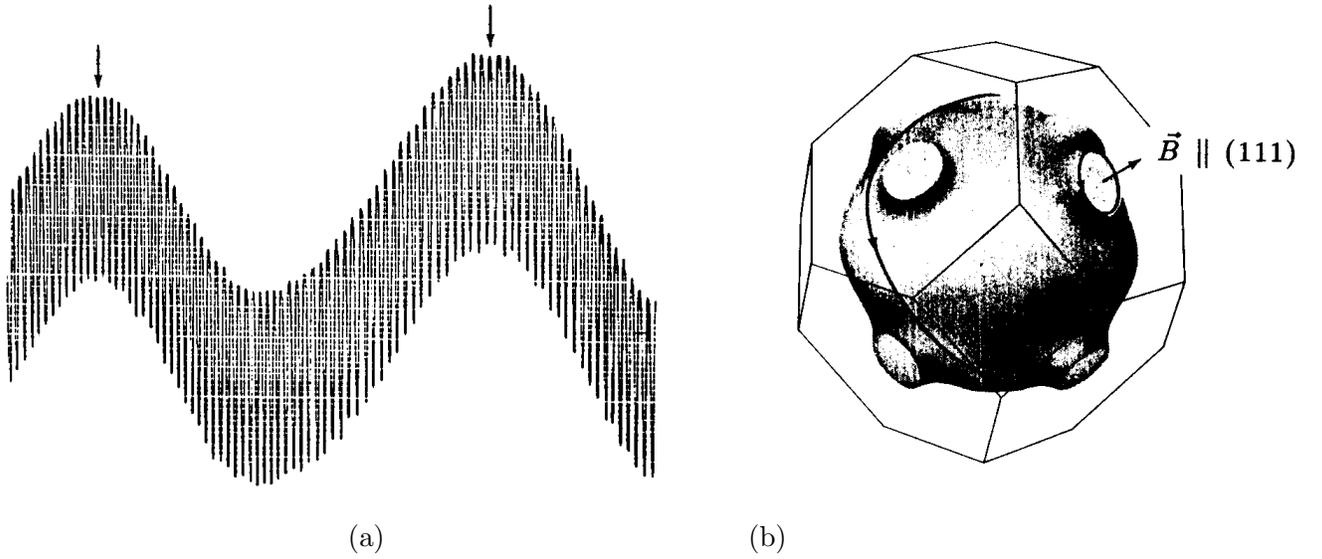
Figure 5.5: (a) De Haas–van Alphen effect for silver with $\vec{B} \parallel$ (111) direction, allowing observation of the belly (fast oscillation) orbit and neck (slow oscillation) orbit shown in (b). The Fermi surface for silver is inferred from measurement of the de Haas–van Alphen effect as a function of magnetic field orientation. The period for the neck orbits [see (b)] is given by the distance between the vertical arrows in (a).

and reciprocal space are inversely proportional to one another, large orbits in k-space (see Fig. 5.4) correspond to small orbits in real space. Furthermore for ellipsoidal orbits (which commonly occur in semiconductor physics), a large k_y/k_x ratio in the k-space orbit would correspond to a small y/x ratio in real space orbit but a large value for x/y, so that the semi-major axis in the real space orbit is rotated by 90°, relative to the semi-major axis of the reciprocal space orbit.

Although we have neglected the electron spin in the above discussion, it is nevertheless important. De Haas–van Alphen oscillations occur whenever a spin-up or a spin-down level crosses E_F. In fact, magneto-oscillatory observations provide an excellent tool for studying both the Landau level spacing as well as the effective g–factor g_{eff} as can be seen from Fig. 4.2d. Values for m_c^* and g_{eff} can be obtained independently since the period between every second resonance yields the Landau level separation, while sequential resonances are separated by $g_{\text{eff}}\mu_B B$.

5.3   Selection Rules for Landau Level Transitions

Since the magnetic energy states are described by harmonic oscillator wave functions, the matrix elements coupling different Landau levels are described by the selection rules for harmonic oscillators. Utilizing the matrix element of the coordinate taken between harmonic

oscillator states, we write

$$\langle \ell | x | \ell' \rangle = \sqrt{\frac{\hbar}{2m_c^* \omega_c^*}} \left[\sqrt{\ell+1}\, \delta_{\ell',\ell+1} + \sqrt{\ell}\, \delta_{\ell',\ell-1} \right]. \tag{5.7}$$

The corresponding matrix element for p_x is

$$\langle \ell | p_x | \ell' \rangle = \sqrt{\frac{\hbar m_c^* \omega_c^*}{2}} \left[\sqrt{\ell+1}\, \delta_{\ell',\ell+1} + \sqrt{\ell}\, \delta_{\ell',\ell-1} \right]. \tag{5.8}$$

The matrix elements for x and p_x determine the matrix elements for intraband transitions, referred to in §5.1. It is also of interest to discuss the expectation value of $\langle \ell | x^2 | \ell' \rangle$ and $\langle \ell | p_x^2 | \ell' \rangle$ which are

$$\langle \ell | x^2 | \ell \rangle = \left(\frac{\hbar}{2m_c^* \omega_c^*} \right) (2\ell+1) = \frac{\hbar}{m_c^* \omega_c^*}(\ell+1/2) \tag{5.9}$$

$$\langle \ell | p_x^2 | \ell \rangle = \left(\frac{\hbar m_c^* \omega_c^*}{2} \right) (2\ell+1) = \hbar m_c^* \omega_c^*(\ell+1/2) \tag{5.10}$$

to yield the partition theorem that the kinetic and potential energies of the harmonic oscillator are each $(\hbar \omega_c^*/2)(\ell+1/2)$. The "classical mean radius" for a harmonic oscillator state is defined by

$$\sqrt{\langle \ell | x^2 | \ell \rangle} = \lambda \sqrt{(\ell+1/2)} \tag{5.11}$$

using Eq. 5.9, thus giving physical meaning to the characteristic length λ in a magnetic field which is $\lambda = (\hbar/m_c^* \omega_c^*)^{1/2} = (c\hbar/eB)^{1/2}$ as given in Eq. 4.29. We see here that λ is independent of m_c^* and except for universal constants depends only on B. The classical mean radius thus has a value at 10 tesla (or 100 kG) of $\sim 10^{-6}$ cm which is about 30 lattice constants in extent. Thus to get a classical orbit within a unit cell we would require fields of $\sim 3{,}000$ tesla or 30 megagauss. With present technology it is not yet possible to generate an external magnetic field with magnetic effects comparable in magnitude to crystal fields, though the highest available fields (300 tesla in the form of pulsed fields) permit entry into this important and interesting regime.

5.4   Landau Level Quantization for Large Quantum Numbers

The most general quantization condition for electrons in conduction bands was given by Onsager. Suppose that a magnetic field is applied parallel to the z–axis. Then the wave vector components k_x, k_y which are perpendicular to the magnetic field B should satisfy the commutation relation

$$[k_x, k_y] = \frac{s}{i}, \tag{5.12}$$

where $s = 1/\lambda^2$ is proportional to the magnetic field B and is defined as $s = eB/\hbar c$ and where

$$k_x \rightarrow \frac{1}{i}\frac{\partial}{\partial x} - \frac{eB}{c\hbar}y \tag{5.13}$$

and

$$k_y \rightarrow \frac{1}{i}\frac{\partial}{\partial y}. \tag{5.14}$$

69

The reason why k_x and k_y in a magnetic field do not commute, of course, relates to the fact that y and p_y do not commute. We define the raising and lowering operators k_+ and k_- in terms of k_x and k_y

$$k_\pm = \frac{1}{\sqrt{2}}(k_x \pm i k_y), \qquad (5.15)$$

and the operation of $k_\pm$ on the harmonic oscillator wavefunction ϕ_ℓ is given by

$$\begin{aligned} k_+\phi_\ell &= [(\ell+1)s]^{\frac{1}{2}}\phi_{\ell+1} \\ k_-\phi_\ell &= (\ell s)^{\frac{1}{2}}\phi_{\ell-1}. \end{aligned}, \qquad \ell = 0,1,2,\cdots. \qquad (5.16)$$

The general quantization condition gives $k^2 = k_+k_- + k_-k_+$ so that

$$(2\ell+1)s \longrightarrow k^2 \qquad (5.17)$$

and corresponds to the Bohr–Sommerfeld–Onsager relation:

$$\oint_{E(k)=\text{const}} |k|dk = 2\pi s\left(\ell + \frac{1}{2}\right), \quad (\ell \gg 1) \qquad (5.18)$$

where the line integral is over an orbit on the constant energy surface. This semiclassical quantization gives the classical limit for large quantum numbers and can be applied to calculate orbits of carriers in a magnetic field on any constant energy surface.

Chapter 6

The Quantum Hall Effect (QHE)

References

- Prange and Girvin, *The Quantum Hall Effect*, Springer-Verlag (1987).

6.1 Introduction to Quantum Hall Effect

The observations of the quantum Hall effect (QHE), and the fractional quantum Hall effect (FQHE) which is mentioned in section §6.6, were made possible by advances in the preparation of high mobility materials with physical realizations of a 2D electron gas. The MOSFET devices (see Part I, §9.2) and the modulation-doped heterostructures (see Part I, §9.3) give rise to the formation of a 2D electron gas in a narrow interface region. In this Chapter we present a simple view of the physics of the quantum Hall effect and the two-dimensional electron gas.

The "Quantum Hall Effect" (QHE) is the step–like increase in the Hall resistance ρ_{xy} in units of h/e^2 with magnetic field (see Fig. 6.1). Each step in (ρ_{xy}) is accompanied by a vanishing of the magnetoresistance (i.e., $\rho_{xx} = 0$) as shown in Fig. 6.1. For an ordinary 3D electron gas, ρ_{xy} increases linearly with magnetic field B and the magnetoresistance ρ_{xx} increases as B^2 (see Part I, §8.2). The quantum Hall effect is a strictly 2D phenomenon which can be observed in semiconductors containing a 2D electron gas region (e.g., in a modulation–doped superlattice as in Part I, §9.3). A second requirement for observation of the Quantum Hall Effect is a very high carrier mobility, so that no carrier scattering occurs until the carrier has completed many cyclotron orbits ($\omega_c \tau \gg 1$). A third prerequisite for the observation of the quantum Hall effect is that the Landau level separation of the magnetic levels is large compared with $k_B T$. Thus the QHE is normally observed at very high magnetic fields, very low temperatures and in very high mobility samples, as shown in Fig. 6.1.

6.2 Basic Relations for 2D Hall Resistance

The conventional 3D Hall effect is usually measured in a long sample in which a fixed current I_x is flowing in the x–direction and a magnetic field B is applied in the z–direction. The Lorentz force on the electrons $e(\vec{v}/c) \times \vec{B}$ is compensated by the Hall electric field E_H
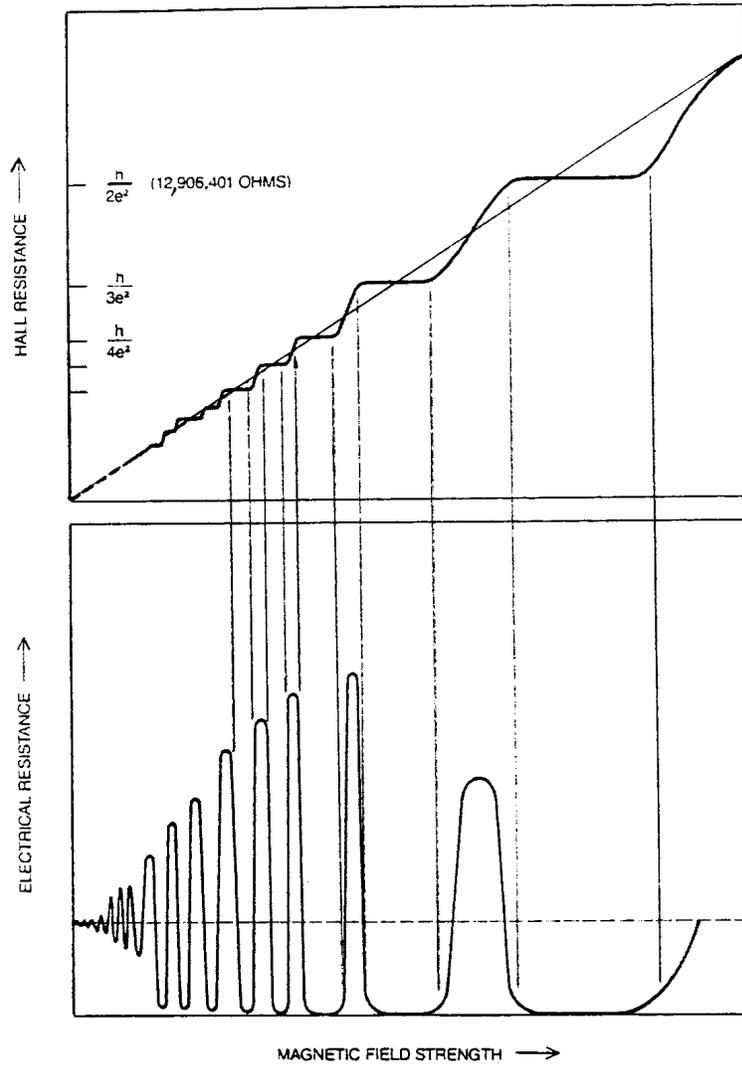
Figure 6.1: The quantum Hall effect. As shown in the upper panel, the Hall resistance shows plateaux which coincide with the disappearance of the sample's electrical resistance. On the plateaux, the Hall resistance remains constant while the magnetic field strength is varied. At each of these plateaux, the value of the Hall resistance is precisely equal to $h/(\ell e^2)$, where ℓ is an integer, while the magnetoresistance component vanishes $\rho_{xx} = 0$. (Note: plateaux is the preferred plural of plateau.)

Figure 6.2: Typical geometry of a sample used for Hall effect measurements. The formation of a 2D electron gas (2DEG) in a GaAs heterostructure is shown in the enlargement of the cross section. The Hall voltage V_H and the voltage drop V_x are measured under the constant current condition $I_x = $ constant as a function of the magnetic field B_z perpendicular to the 2D electron gas.
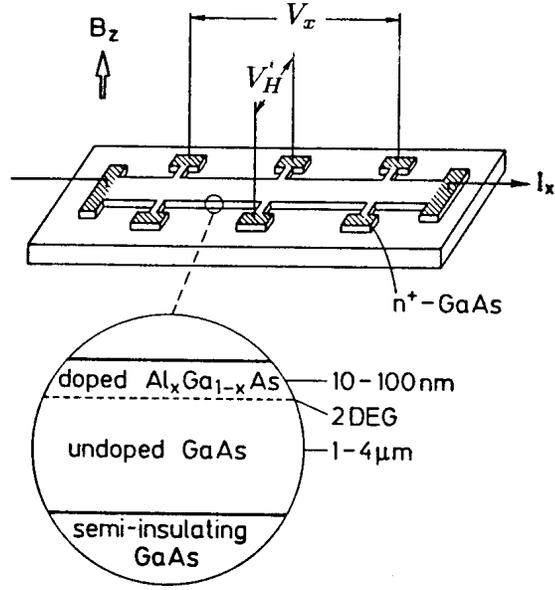
in the y–direction to prevent the flow of current in the y–direction. The geometry for the Hall measurements is shown in Fig. 6.2. The two voltages V_x (driving voltage) and V_H (Hall voltage) are measured. The longitudinal (R_x) and Hall (R_H) resistances are defined in terms of the current flow I_x as:

$$R_x = V_x/I_x$$

$$R_H = V_H/I_x.$$

(6.1)

In general, the conductivity tensor ($\overleftrightarrow{\sigma}$) and the resistivity ($\overleftrightarrow{\rho}$) tensors relate the current density ($\vec{j}$) and the electric field ($\vec{E}$) vectors, and the vector relations in 2D are written as:

$$\vec{j} = \begin{pmatrix} j_x \\ j_y \end{pmatrix} = \overleftrightarrow{\sigma} \cdot \vec{E} = \begin{pmatrix} \sigma_{xx} & \sigma_{xy} \\ \sigma_{yx} & \sigma_{yy} \end{pmatrix} \begin{pmatrix} E_x \\ E_y \end{pmatrix}$$

(6.2)

and in terms of the resistivity as

$$\vec{E} = \begin{pmatrix} E_x \\ E_y \end{pmatrix} = \overleftrightarrow{\rho} \cdot \vec{J} = \begin{pmatrix} \rho_{xx} & \rho_{xy} \\ \rho_{yx} & \rho_{yy} \end{pmatrix} \begin{pmatrix} j_x \\ j_y \end{pmatrix}$$

(6.3)

with the required relation between $\overleftrightarrow{\sigma}$ and $\overleftrightarrow{\rho}$

$$\overleftrightarrow{\sigma} \cdot \overleftrightarrow{\rho} = \overleftrightarrow{1}$$

(6.4)

where $\overleftrightarrow{1}$ is the unit matrix with components (δ_{ij}). Since the off–diagonal xy components of $\overleftrightarrow{\rho}$ result from the magnetic field, they are odd under reversal of the magnetic field direction

(time reversal symmetry), yielding the relation between components

$$\sigma_{xx} = \sigma_{yy},$$

$$\sigma_{yx} = -\sigma_{xy},$$

$$\rho_{xx} = \rho_{yy},$$

$$\rho_{yx} = -\rho_{xy}.$$

(6.5)

Equations 6.4 and 6.5 imply that for the 2D electron gas:

$$\rho_{xx} = \sigma_{xx}/(\sigma_{xx}^2 + \sigma_{xy}^2), \qquad \rho_{xy} = -\sigma_{xy}/(\sigma_{xx}^2 + \sigma_{xy}^2)$$

$$\sigma_{xx} = \rho_{xx}/(\rho_{xx}^2 + \rho_{xy}^2), \qquad \sigma_{xy} = -\rho_{xy}/(\rho_{xx}^2 + \rho_{xy}^2).$$

(6.6)

An especially interesting implication of these formulae is that in a 2D system, when $\sigma_{xx} = 0$ but $\sigma_{xy} \neq 0$, then ρ_{xx} is also zero (and vice versa). This means that (as long as σ_{xy} is finite), the vanishing of the longitudinal conductivity implies that the longitudinal resistivity also vanishes. This is precisely the situation that occurs in the quantum Hall effect, and is fundamental to this phenomenon.

We now relate the resistance parameters that are measured (R_x and R_H) to the current density $\vec{j}$ and the electric fields $\vec{E}$. For a long device (as shown in Fig. 6.2), $j_y = 0$, so that R_H is related to the resistivity components ρ_{xx} and ρ_{xy} via:

$$R_x = V_x/I_x = (L/W) \cdot (E_x/j_x)|_{j_y=0} = (L/W)\rho_{xx}$$

$$R_H = V_H/I_x = (E_y/j_x)|_{j_y=0} = \rho_{xy}$$

(6.7)

Note that the dimensions of the resistivity in 2D is $\Omega/\square$, and that R_H in 2D has the same dimensions as ρ_{xy}.

In the presence of a DC magnetic field $\vec{B} = B\hat{z}$, and in the relaxation–time approximation, the classical equation of motion for the carriers is written as:

$$\frac{d\vec{v}}{dt} = \frac{e}{m^*}\left(\vec{E} + \frac{1}{c}\vec{v} \times \vec{B}\right) - \vec{v}/\tau$$

(6.8)

where $\vec{v}$ denotes the drift velocity of the carriers, and the charge on the electron is taken as a negative number. Using the relation $\vec{j} = ne\vec{v}$, we can write

$$\sigma_0 E_x = j_x - \omega_c \tau j_y$$

$$\sigma_0 E_y = \omega_c \tau j_x + j_y$$

(6.9)

where $\sigma_0 = ne^2\tau/m^*$ and $\omega_c = eB/m^*c$. Finally, combining Eqs. 6.7 and 6.9 with the condition $j_y = 0$, we can write:

$$E_y = \frac{\omega_c \tau}{\sigma_0} j_x$$

(6.10)

and the Hall resistance R_H becomes

$$R_H \equiv \frac{E_y}{j_x} = \frac{\omega_c \tau}{\sigma_0} = \frac{(eB/m^*c)\tau}{(ne^2\tau/m^*)} = \frac{B}{nec} = \mathcal{R}B \qquad (6.11)$$

where $\mathcal{R} = (1/nec)$ is called the Hall coefficient. We note here that R_H is proportional to the magnetic field. The result derived in Eq. 6.11 is valid for a classical system that ignores the quantization of the magnetic energy levels. This quantization effect becomes important in the limit $\omega_c\tau \gg 1$. The classical result for a 2D system is the same result as was previously obtained for the 3D system (see Part I, §8.2). Yet the experimental results for the 2D electron gas in a modulation–doped GaAs/Ga$_{1-x}$Al$_x$As interface (Fig. 6.1) exhibit the quantum Hall effect, where V_H or ρ_{xy} shows a series of flat plateaux as a function of magnetic field rather than a simple linear dependence in B (Eq. 6.11). The reason for the steps in ρ_{xy} (or R_H) as a function of B is due to the density of states of the 2D electron gas in a magnetic field, as discussed below.

6.3   The 2D Electron Gas

We refer to the phenomenon shown in Fig. 6.1 as the quantum Hall effect because the values of R_H exhibit a plateau whenever

$$R_H = \frac{h}{\ell e^2} \qquad \ell = 1, 2, 3, \ldots \qquad (6.12)$$

where ℓ is an integer. Figure 6.1 shows the results of Hall measurements on a modulation–doped GaAs/Al$_x$Ga$_{1-x}$As heterostructure. Here ρ_{xx} and ρ_{xy} are shown as a function of magnetic field for a heterostructure with a fixed density of carriers. These experiments are done at a low temperature (4.2 K), and the plateaux for ρ_{xy} can be observed very clearly, especially in the limit of small ℓ. (The plural of plateau is plateaux.) The results shown in Figure 6.1, indicate that R_H for the 2D electron gas is quantized. Detailed measurements show that R_H is given by Eq. 6.12 to an accuracy of better than 0.1 ppm (parts per million). This quantization is reported to be independent of the sample geometry, the temperature, the scattering mechanisms, or other parameters, including the physical system giving rise to the 2D electron gas. The exactness of these results and their apparent independence of experimental parameters are very intriguing and, as we discuss below, are ultimately due to a fundamental physical principle. A schematic diagram summarizing the general behavior of the 2D electron gas is given in Fig. 6.3 for ρ_{xy}, ρ_{xx} and σ_{xx} vs B, and also included in this diagram is the comparison with the behavior of a 3D electron gas.

Referring to the 2D conductivity $\overleftrightarrow{\sigma}$ and resistivity $\overleftrightarrow{\rho}$ tensors defined in Eqs. 6.2 and 6.3, we can write $\overleftrightarrow{\rho}$ and $\overleftrightarrow{\sigma}$ in the region of the plateaux as

$$\overleftrightarrow{\rho} = \begin{pmatrix} 0 & -R_Q/i \\ R_Q/i & 0 \end{pmatrix} \qquad (6.13)$$

and

$$\overleftrightarrow{\sigma} = \begin{pmatrix} 0 & i/R_Q \\ -i/R_Q & 0 \end{pmatrix} \qquad (6.14)$$

Figure 6.3: Qualitative behavior for σ_{xx}, ρ_{xx} and ρ_{xy} of a two–dimensional electron gas with a fixed carrier density as a function of the magnetic field. The dotted lines represent the classical curves for a 3D electron gas. The effect of spin degeneracy is not included in these curves.

76
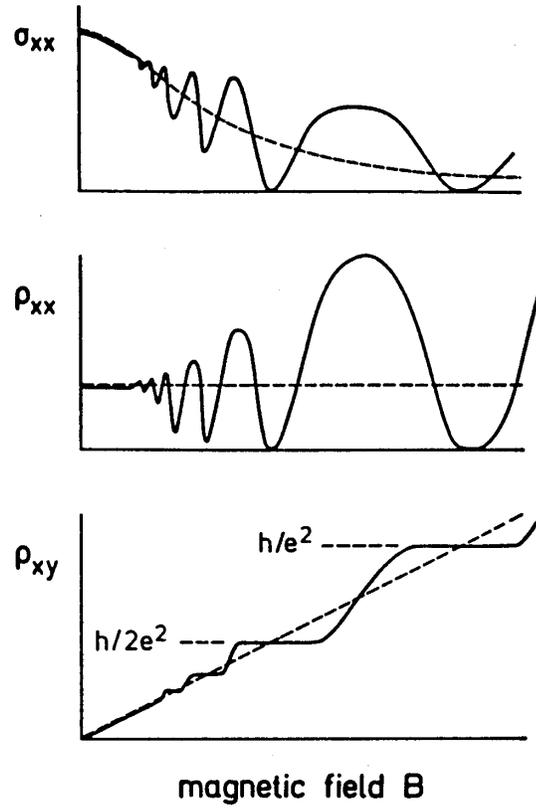
where $R_Q = h/e^2$, and where $\rho_{xx} = \rho_{yy} = 0$ and $\sigma_{xx} = \sigma_{yy} = 0$. At these plateaux the power dissipation P_{diss} vanishes because

$$P_{\text{diss}} = \vec{j} \cdot \vec{E} = \vec{j} \cdot \overleftrightarrow{\rho} \cdot \vec{j} = \frac{1}{i} \begin{pmatrix} j_x & j_y \end{pmatrix} \begin{pmatrix} 0 & -R_Q \\ R_Q & 0 \end{pmatrix} \begin{pmatrix} j_x \\ j_y \end{pmatrix} = \frac{1}{i} \left[-R_Q j_x j_y + R_Q j_y j_x \right] = 0.$$
(6.15)

Thus at the plateaux we have no power dissipation and $\rho_{xy} = R_Q/e$ independent of material, impurity level, sample geometry, and ρ_{xy} is just dependent on the fundamental constants h and e.

To explain the quantized Hall effect, let us first consider the carriers of the two dimensional electron gas to be <u>free</u> electrons at $T = 0$, but subjected to an applied magnetic field B normal to the plane of the 2D electron gas. The Landau quantization for B normal to the film surface gives completely quantized sub–band energies (for a simple band)

$$E_{n,\ell} = E_n + (\ell + 1/2)\hbar\omega_c \pm g^* \mu_B B = E_n + E_\ell$$
(6.16)

where $\omega_c \equiv eB/m^*c$ is the cyclotron frequency and g^* is the effective g–factor as also for the 3D case, but now E_n pertains to the z–dependent bound state energy levels of the 2D electron gas. For the simplest case, the carrier density is arranged to be low so that only the lowest bound state ($n = 1$) is occupied. The number of states <u>per unit area</u> is found by noting that the energy is independent of the harmonic oscillator center.

Since the energy levels do not depend on the central position of the harmonic oscillator y_0, we can sum on all the k_x states to obtain the k_x degeneracy (see Eq. 4.28) per unit area

$$g_{2D} = \frac{eB}{ch}.$$
(6.17)

This degeneracy factor is the same for each Landau level and is proportional to the magnetic field B and depends only on fundamental physical constants (i.e., e, c, h). In addition there is a degeneracy factor of 2 for the electron spin if the electron spin is not considered explicitly in writing the energy level equation.

Since there is no k_z dispersion for the 2D electron gas, the density of states in a magnetic field in two–dimensions consists of a series of singularities (δ-functions) as shown in Fig. 6.4b in contrast to the continuum of states in 3D, also shown in the figure. Multiplying (eB/ch) by $\hbar\omega_c$ gives the number of 2D states in zero magnetic field that coalesce to form each Landau level. This number increases proportionally to the magnetic field as does also the Landau level separation. If at a given magnetic field there are ℓ' filled Landau levels, the carrier concentration (neglecting spin) is given by $n_{2D} = \ell'(eB/2\pi\hbar c)$, where n_{2D} is the carrier density associated with a given bound state $n = 1$. Thus the Hall resistance R_H in 2D becomes

$$R_H = \frac{B}{n_{2D}ec} = \frac{h}{\ell' e^2} = \frac{R_Q}{\ell'}$$
(6.18)

for ℓ' filled magnetic energy levels. Thus we can see that the unique property of the density of states of a 2D electron gas in a magnetic field (see Fig. 6.4) leads to a Hall conductance at $T = 0$ that is quantized in multiples of e^2/h.

Carrier filling in 2D is fundamentally different from that in 3D. As the Fermi level rises in 3D, because of the k_z degeneracy, all the Landau levels with subband extrema below E_F

Figure 6.4: Schematic density of states in a magnetic field for: (a) three–dimensions, where the energy is referred to the bottom of the band ($E = 0$) and (b) two–dimensions, where the energy is referred to the lowest bound state energy E_1. The energy is plotted in units of the cyclotron energy $\hbar\omega_c$. Dotted curves represent the density of states without a magnetic field. We note that in the 2D case the density of states in zero field is $m/\pi\hbar^2$, indicated by the dashed line. The filling per Landau level ℓ in a magnetic field is the degeneracy factor $g_{2D} = eB/(2\pi\hbar c)$ or eB/hc.
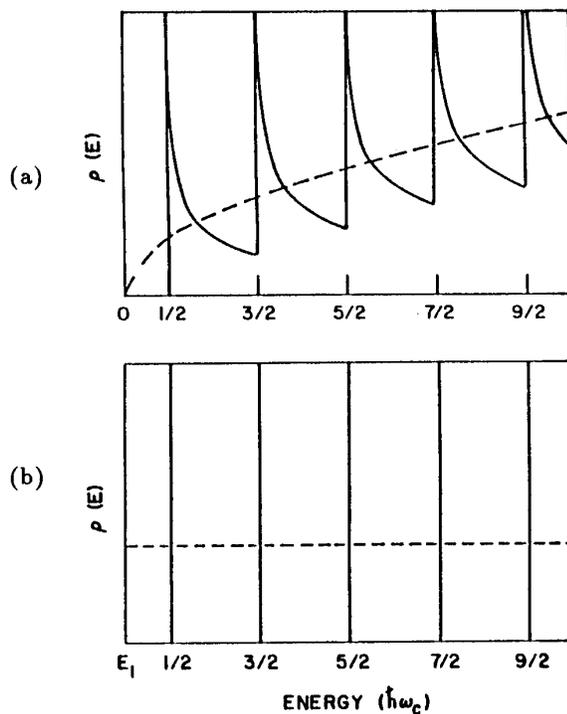
will fill. To the extent that the electron density is low enough so that only one bound state is occupied, each magnetic subband fills to the same number of carriers at a given B field. In the region of the plateaux all Landau levels for $\ell \leq \ell'$ are filled and all Landau levels for $\ell > \ell'$ are empty so that for $k_B T \ll \hbar\omega_c$, very little carrier scattering can occur.

The electrons in the semiconductor heterostructure, however, are not free carriers: their behavior is influenced by the presence of the periodic ionic potential, impurities, and scattering phenomena (see Fig. 6.5). Therefore the simple explanation given above for a perfect crystal needs to be extended to account for these complicating effects. In Fig. 6.5 the two–dimensional density of states in a magnetic field is shown schematically in the presence of disorder. The δ–functions of Fig. 6.5(a) are now replaced by a continuous function $D(E)$ as shown in Fig. 6.5(b). The figure shows that the magnetic field range over which conduction occurs is broadened. The figure further shows that in the tails of each Landau sub–band there exist regions of localized states (the shaded areas). The electrons associated with the mobility gap are in localized states that do not contribute to conduction. Much research has been done to show that the simple model described above accurately describes ρ_{xy} and ρ_{xx} for the 2D electron gas within the region of the plateaux in actual semiconductor devices.

Let us consider the diagram for the 2D density of states in a magnetic field shown in Fig. 6.6 for a single Landau level. Suppose the magnetic field is just large enough so that the indicated 2D Landau level is completely filled and E_F lies at $\nu = 1$, where ν represents the fractional filling of the 2D Landau level. Then as the magnetic field is further increased, the Fermi level falls. So long as the Fermi level remains within the region of the localized states, then $\sigma_{xx} = 0$. Thus when E_F lies in the shaded region, E_F is effectively in an
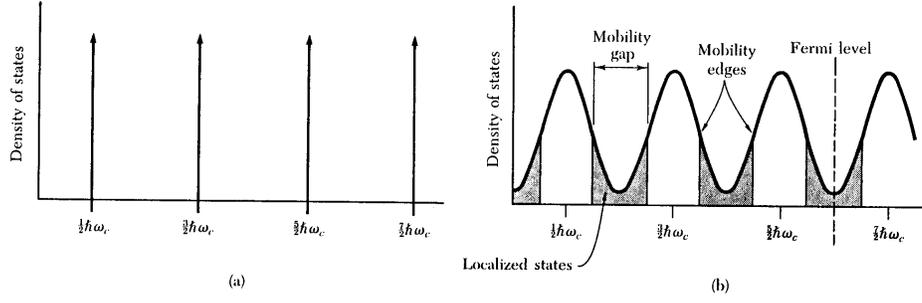
Figure 6.5: Schematic representation of the 2D density of states in a magnetic field (a) without disorder and (b) with disorder. The shaded regions correspond to localized states.

energy gap where $\sigma_{xx} \equiv 0$ and the Hall conductance σ_{xy} remains on a plateau determined by $\ell' e^2/h$. As B increases further, E_F eventually reaches the unshaded region where σ_{xx} no longer vanishes and E_F passes through the mobile states (see Fig. 6.6), causing σ_{xy} to jump from $\ell' e^2/h$ to $(\ell' - 1)e^2/h$ as E_F passes through the mobile states. When the magnetic field is large enough for E_F to reach the localized states near $\nu = 0$, then σ_{xx} again vanishes and σ_{xy} now remains at the plateau $(\ell' - 1)e^2/h$.

From these arguments we can conclude that the steps in ρ_{xy} and the zeros in ρ_{xx} are caused by the passage of a 2D Landau level through the Fermi level. When the effect of the electron spin is included, spin splitting of the Landau levels is expected in the quantum Hall effect measurements. To see spin splittings effects the measurements must be made at sufficiently low temperatures (e.g., $T = 0.35$ K). Spin splitting effects of the $\ell = 1$ Landau level ($1 \downarrow$ and $1 \uparrow$) have been clearly seen. The observation of spin splitting in the Quantum Hall Effect thus requires high fields, low m_c^*, high mobility samples to achieve $\omega_c \tau \gg 1$ and low temperatures $k_B T \ll \hbar \omega_c$ to prevent thermal excitation between Landau levels.

6.4 Effect of Edge Channels

In the simple explanation of the Quantum Hall effect, it is necessary to assume both localized states ($\sigma_{xx} = 0$) and extended states ($\sigma_{xx} \neq 0$). In taking into account the so-called edge channels, it is possible to explain more clearly why the quantization is so precise in the Quantum Hall Effect for real systems.

Referring to the derivation of the Landau levels for motion in a plane perpendicular to the magnetic field (see §4.4), we assume that only the lowest band state $n = 1$ is occupied and we neglect the interaction of the electron spin with the magnetic field. The wave function for an electron in the 2D electron gas can then be written as

$$\Psi_{2D}(x, y) = e^{ik_x x} \phi(y) \tag{6.19}$$

where $\phi(y)$ satisfies the harmonic oscillator equation

$$\left[\frac{p_y^2}{2m_c^*} + \frac{1}{2} m_c^* \omega_c^{*2} (y - y_0)^2 \right] \phi(y) = \left[\frac{p_y^2}{2m_c^*} + V(y) \right] \phi(y) = E_\ell \phi(y) \tag{6.20}$$

79

Figure 6.6: The density of states $[D(E)]$, d.c. conductivity (σ_{xx}), and the Hall conductivity (σ_{xy}) are schematically shown as a function of the fractional filling factor ν for a Landau subband. Shaded regions in the density of states denote the regions of localized carriers corresponding to an effective energy gap between magnetic subbands.

80
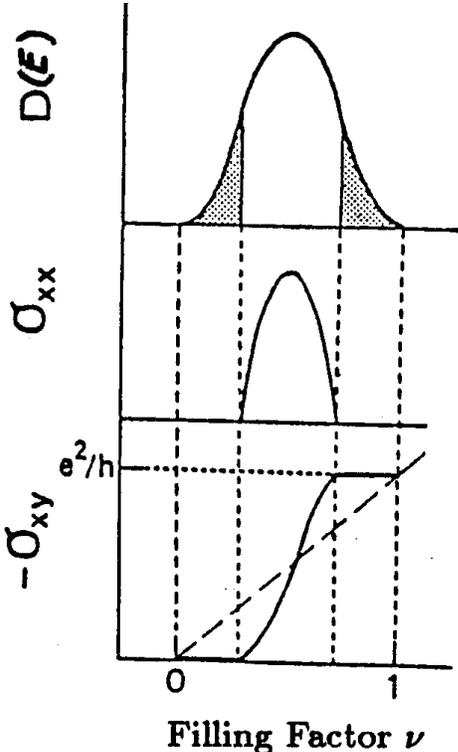
in which the harmonic oscillator center is given by

$$y_0 = \frac{\hbar k_x}{m_c^* \omega_c^*} = \lambda_B^2 k_x \tag{6.21}$$

and the harmonic oscillator energies are

$$E_\ell = (\ell + 1/2)\hbar\omega_c^*. \tag{6.22}$$

The characteristic magnetic length

$$\lambda_B = \sqrt{\frac{\hbar c}{eB}} = \frac{250\text{\AA}}{\sqrt{B(\text{tesla})}} \tag{6.23}$$

relates to the real space orbit of the electron in a harmonic oscillator state (Eq. 5.11) and except for universal constants depends only on the magnetic field. Since the energy in Eq. 6.22 is independent of k_x, the electron velocity component x_x vanishes

$$v_x = \frac{1}{\hbar}\frac{\partial E}{\partial k_x} = 0 \tag{6.24}$$

and there is no net current along $\hat{x}$.

The argument that the energy is independent of k_x, however, only applies to those harmonic oscillator centers y_0 that are interior to the sample. But if y_0 takes on a value close to the sample edge, i.e., $y_0 \simeq 0$ or $y_0 \simeq L_y$, then the electron is more influenced by the infinite potential barrier at the edge than the harmonic oscillator potential $V(y)$ associated with the magnetic field. Electrons in these edge orbits will be reflected at the edge potential barriers and $V(y)$ is no longer strictly a harmonic oscillator potential. Since the potential $V(y)$ is perturbed, the energy will also be perturbed and the energy will then become dependent on k_x. Since the harmonic oscillator orbit size is $\lambda_B\sqrt{\ell+1}$, the energy of the 2D electron gas depends on k_x only for a distance of approximately $\lambda_B\sqrt{\ell+1}$ from the sample edge.

The effect of the sample edges can be understood in terms of the skipping orbits illustrated in Fig. 6.7. All the harmonic oscillator orbits with y_0 values within λ_B of the edge will contribute to the current density j_x by the argument in Fig. 6.7. The current I_ℓ contributed by the ℓth edge channel is

$$I_\ell = ev_{\ell,x}\left(\frac{dn}{dE_\ell}\right)\Delta\mu \tag{6.25}$$

where (dn/dE_ℓ) is the 1D density of states and $\Delta\mu$ is the drop in chemical potential along the edge channel. Now we can write

$$\frac{dn}{dE_\ell} = \frac{dn}{dk_x}\frac{dk_x}{dE_\ell} = \left(\frac{1}{2\pi}\right)\left(\frac{1}{\hbar v_{\ell,x}}\right) = \frac{1}{hv_{\ell,x}} \tag{6.26}$$

where $v_{\ell,x}$ is the velocity of the electrons in the x direction due to the carriers in channel ℓ. Substitution of Eq. 6.26 into 6.25 yields $I_\ell = (e/h)\Delta\mu$, which is independent of ℓ, so that the total current is obtained by summing over the edge channels to yield

$$I_x = \ell_c\frac{e}{h}\Delta\mu \tag{6.27}$$

81
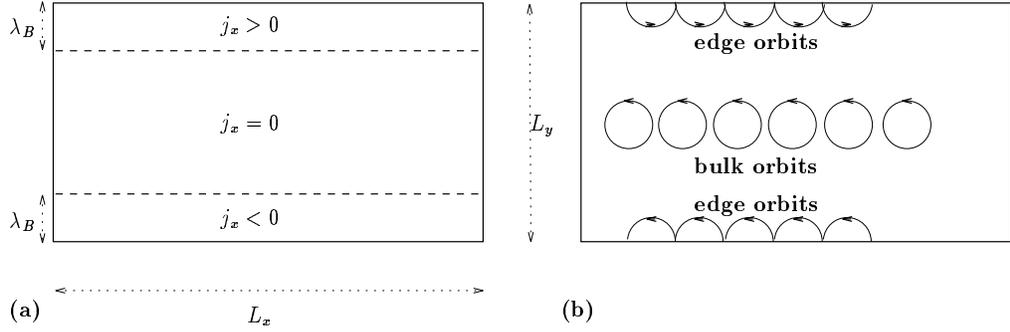
Figure 6.7: Location of the edge skipping orbits in a magnetic field. The edge regions shown in (a) are defined by the characteristic length $\lambda_B = (\hbar c/eB)^{1/2}$. Along each edge, (b) shows that all orbits give rise to current j_x in the same direction but the current direction is opposite for the two edges. The bulk orbits do not give rise to a current j_x.

Figure 6.8: Schematic diagram of current flow for edge channels. The dark circles denote the contacts between the edge channels and the electron reservoirs at electrochemical potential μ_2 and μ_1.
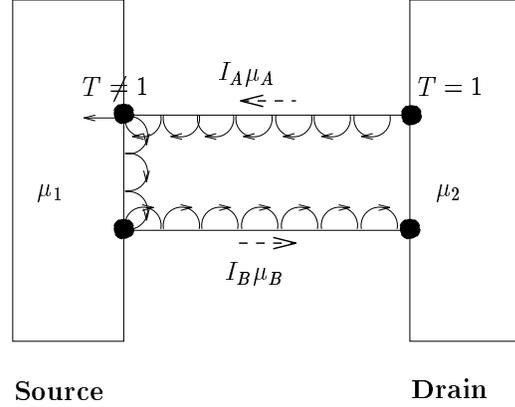
where ℓ_c is the number of edge channels. If the conditions $\lambda_B \ll \ell_\phi$ and $\lambda_B \ll \ell_e$ are satisfied, where ℓ_ϕ and ℓ_e are, respectively, the inelastic and elastic scattering lengths, electrons are not likely to scatter across the sample (backscattering) because of the electron localization in the variable y ($\psi \sim \exp[-y^2/\lambda_B^2]$). The opposing directions of j_x along the two edges guarantees that the continuity equation is satisfied.

Let us now consider the electrochemical potential μ, which has a constant value along each edge channel, because of the absence of back scattering, as noted above. Two edge channels are shown in Fig. 6.8. From Eq. 6.27 we obtain the total current I_x in the upper and lower edges. The quantity $\Delta\mu$ in Eq. 6.25 denotes the potential drop between two points where the transmission coefficient T is unity ($T \equiv 1$). Thus for the upper edge channel,

$$I_A = \ell_{cA}(e/h)(\mu_2 - \mu_A), \tag{6.28}$$

indicating that there is a reflection between the edge channel and μ reservoir and $T \neq 1$. For the lower channel

$$I_B = \ell_{cB}(e/h)(\mu_B - \mu_2). \tag{6.29}$$

the number of edge channels for the two edges is the same, so that $\ell_{cA} = \ell_{cB} = \ell_c$. We thus

obtain:

$$I_x = I_A + I_B = \ell_c(e/h)(\mu_B - \mu_A). \tag{6.30}$$

Since the Hall voltage V_y is given by the difference in electrochemical potential in the y direction of the sample, we obtain

$$eV_y = \mu_B - \mu_A \tag{6.31}$$

so that

$$I_x = \ell_c(e^2/h)V_y. \tag{6.32}$$

The Hall resistance R_H then becomes

$$R_H = \frac{V_y}{I_x} = \frac{h}{e^2\ell_c} = \frac{R_Q}{\ell_c} \tag{6.33}$$

where $R_Q = h/e^2$ is the fundamental unit of resistance and ℓ_c is a quantum number denoting the number of edge channels. The edge channel picture thus provides another way to understand why the quantum Hall effect is associated with a fundamental constant of nature.

6.5 Applications of the Quantized Hall Effect

Because of the high precision with which the Hall resistance is quantized at integer fractions of h/e^2, we obtain

$$\ell' R_H = \frac{h}{e^2} = R_Q = 25,812.200 \ \Omega \quad \ell' = 1, 2, 3, \ldots. \tag{6.34}$$

This quantity called the Klitzing (after the man who discovered the Quantum Hall Effect experimentally) has become the new IEEE resistance standard since 1990 and is known to an accuracy of $\sim 3 \times 10^{-8}$. When combined with the high precision with which the velocity of light is known, $c = 299,792,458 \pm 1.2\text{m/s}$, the quantum Hall effect has become the primary technique for measuring the fine structure constant:

$$\alpha \equiv \frac{e^2}{c\hbar}. \tag{6.35}$$

The fine structure constant must be known to high accuracy in tests of quantum electrodynamics (QED). The results for α from the QHE are not only of comparable accuracy to those obtained by other methods, but this determination of α is also independent of the QED theory. The QHE measurement thus acts as another verification of QED. It is interesting to note that the major source of uncertainty in the QHE result is the uncertainty in the calibration of the standard resistor used as a reference.

6.6 Fractional Quantum Hall Effect (FQHE)

When a two–dimensional electron gas is subjected to a sufficiently low temperature and an intense magnetic field ($B\|z$–axis), of magnitude greater than necessary to achieve the lowest quantum state in the quantum Hall effect, all electrons could be expected to remain in their lowest Landau level and spin state. In this limit, however, the possibility also

exists, that the electrons will further order under the influence of their mutual interactions. Such ordering phenomena have been seen in GaAs/Ga$_{1-x}$Al$_x$As and other quantum well structures, where an apparent succession of correlated electron states has been found at fractional occupations, ν, of the lowest Landau level. This ordering effect is called the fractional quantum Hall effect (FQHE).

Just as for the quantum Hall effect discussed in § 6.3, the fractional quantum Hall effect is characterized by minima in the electrical resistance and plateaux in the Hall resistance for current flow in the two–dimensional layers (x–direction). Whereas the integral quantum Hall effect occurs because of gaps in the density of mobile electron states at energies between the 2D Landau levels (see Fig. 6.4), the fractional quantization is interpreted in terms of new gaps in the spectrum of electron energy levels appearing predominantly at magnetic fields higher than the plateau for the $\ell = 0$ integral quantum Hall effect and associated with electron-electron interactions.

The fractional quantum Hall effect (FQHE) was first observed in the extreme quantum limit, for fractional filling factors ν

$$\nu = \frac{n_{2D}hc}{eB} < 1, \tag{6.36}$$

where the 2D carrier density n_{2D} is given by

$$n_{2D} = \nu \left(\frac{eB}{hc} \right). \tag{6.37}$$

This regime can be achieved experimentally at low carrier densities n_{2D}, high magnetic fields B, and very low temperatures T. The observations of the FQHE thus requires the Landau level spacing $\hbar\omega_c$ to exceed the zero field Fermi level

$$\hbar\omega_c = \frac{\hbar eB}{m_c^* c} > E_F \tag{6.38}$$

where the Fermi level for a single spin orientation is given by

$$E_F = \frac{2\pi n_{2D}\hbar^2}{m^*}. \tag{6.39}$$

This condition is equivalent to requiring the magnetic length or cyclotron radius to be less than the inter–particle spacing $n_{2D}^{-1/2}$, where n_{2D} is the 2D electron density.

To observe electron ordering, it is desirable that electron–electron interactions be large and that electron–impurity interactions be small. This requires the minimization of uncertainty broadening of the electron levels and inhomogeneous broadening caused by potential fluctuations and electron scattering. Thus the observation of the fractional quantum Hall effect is linked to the availability of very high mobility samples containing a 2D electron gas in the lowest bound state level. The best samples for observing the FQHE are the modulation–doped GaAs/Al$_x$Ga$_{1-x}$As interfaces, as shown in Fig. 6.9. In the fabrication the n–doped regions have been confined to a single atomic layer (i.e., δ–doping), far from the quantum well to achieve high carrier mobility.

The highest mobility materials that have been reported for modulation–doped MBE samples have been used for observation of the FQHE. Measurements are made on photolithographically–defined Hall bridges using microampere currents and Ohmic current and

Figure 6.9: Schematic diagram of a modulation–doped n–type semiconductor GaAs/Al$_\text{x}$Ga$_\text{1−x}$As heterostructure and of its energy band structure. CB and VB refer to conduction band and valence band edges; E_{g1} and E_{g2} are, respectively, the energy gaps of the Al$_\text{x}$Ga$_\text{1−x}$As and GaAs regions, while ΔE is the energy corresponding to the zero–magnetic–field filling of the lowest quantum subband of the two–dimensional electron gas, and E_F is the Fermi energy. W is the step height (band offset energy) between the GaAs conduction band and the Al$_\text{x}$Ga$_\text{1−x}$As conduction band at the interface. The two-dimensional electron gas lies in the GaAs region close to the undoped Al$_\text{x}$Ga$_\text{1−x}$As (see lowest diagram). The dopants used to introduce the n-type carriers are located in the region called n-doped AlGaAs.
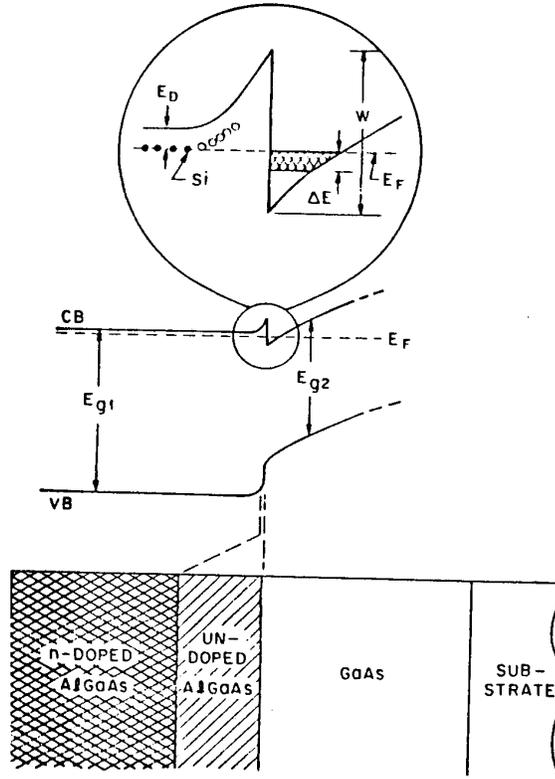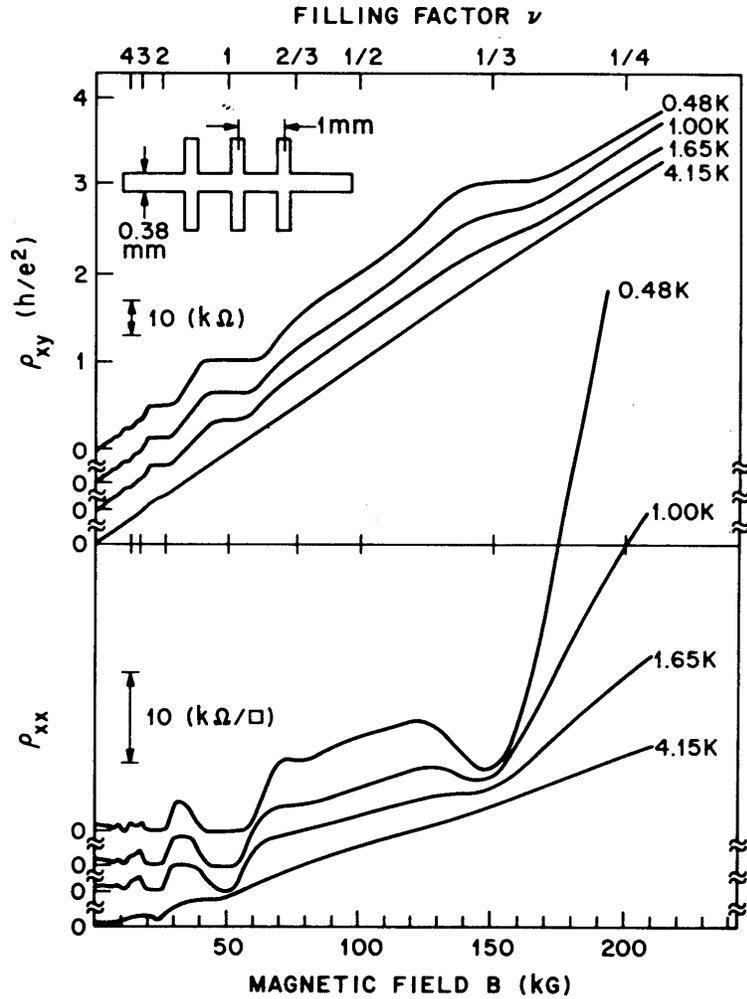
Figure 6.10: First observation of the FQHE in a $GaAs/Al_xGa_{1-x}As$ modulation–doped heterostructure with an areal carrier density of $n = 1.23 \times 10^{11}$ electrons/cm^2 and an electron mobility of $\mu = 90{,}000$ cm^2/Vsec. The Hall resistance ρ_{xy} assumes a plateau at fractional filling $\nu = 1/3$ indicating a fractional quantum number $\ell = 1/3$. [D.C. Tsui, H.L. Störmer and A.C. Gossard, *Phys. Rev. Lett.* 48, 1559 (1982)].

potential contacts. Experimental results for the resistivity and Hall resistance versus magnetic field in the fractional quantum Hall effect regime are shown in Fig. 6.10. Minima develop in the diagonal (in–plane) resistivity ρ_{xx} at magnetic fields corresponding both to integral filling and to certain fractional fillings of the Landau levels. The Hall resistivity ρ_{xy} develops plateaux at the same integral and fractional filling factors. The classical value of the Hall resistance ρ_{xy} for n carriers per unit area is $\rho_{xy} = B/(nec)$ and B/n is interpreted as the magnetic flux per carrier which is the flux quantum $\phi_0 = ch/e$ divided by the Landau level filling ν, so that $B/n = ch/e\nu$ at filling factor ν.

The value of ρ_{xy} is $h/\nu e^2$ at filling factor ν. Plateaux were first measured at $\nu = 1/3$ (see Fig. 6.10) with ρ_{xy} equal to $h/\nu e^2$ to within one part in 10^4.

In addition to quantization at quantum number $1/3$, quantization has been observed at a number of other fractions $\nu = 2/3, 4/3, 5/3, 2/5, 3/5, 4/5, 2/7$ and others (see Fig. 6.11), suggesting that fractional quantization exists in multiple series, with each series based on the inverse of an odd integer. With the highest mobility materials, a fractional quantum Hall effect has recently been observed for an even integer denominator.

Only a certain specified set of fractions exhibit the fractional quantum Hall effect, corresponding to the relation

$$\nu = \cfrac{1}{p + \cfrac{\alpha_1}{p_1 + \cfrac{\alpha_2}{p_2 + \ldots}}} \tag{6.40}$$

where the integers p is odd, p_i is even, and $\alpha_i = 0, \pm 1$. For example, $p = 3$, $p_i = 0$ and $\alpha_i = 0$ for all i yields a fractional filling factor of $1/3$, where the most intense fractional quantum Hall effect is observed. For $p = 3$, $p_1 = 1$ and $\alpha_1 = 1$ and all other coefficients taken to be zero gives $\nu = 2/3$. Equation 6.40 accounts for all the observed examples of the fractional quantum Hall effect except for the case of the recently observed case of $\nu = 5/2$ mentioned above.

To explain the characteristics of the fractional quantum Hall effect, Laughlin proposed a many-electron wavefunction to account for the electron correlations responsible for the fractional quantum Hall effect:

$$\psi_m(z_1, z_2, z_3, \ldots z_N) = \mathcal{C} \prod_{i<j}^{N} (z_i - z_j)^m \exp\left(-\frac{1}{4} \prod_{k}^{N} |z_k|^2 \right) \tag{6.41}$$

where $m = 1/\nu$ and ν is the filling factor. Research at the fundamental level is still being carried out to understand the fractional quantum Hall effect and related phenomena in more detail.
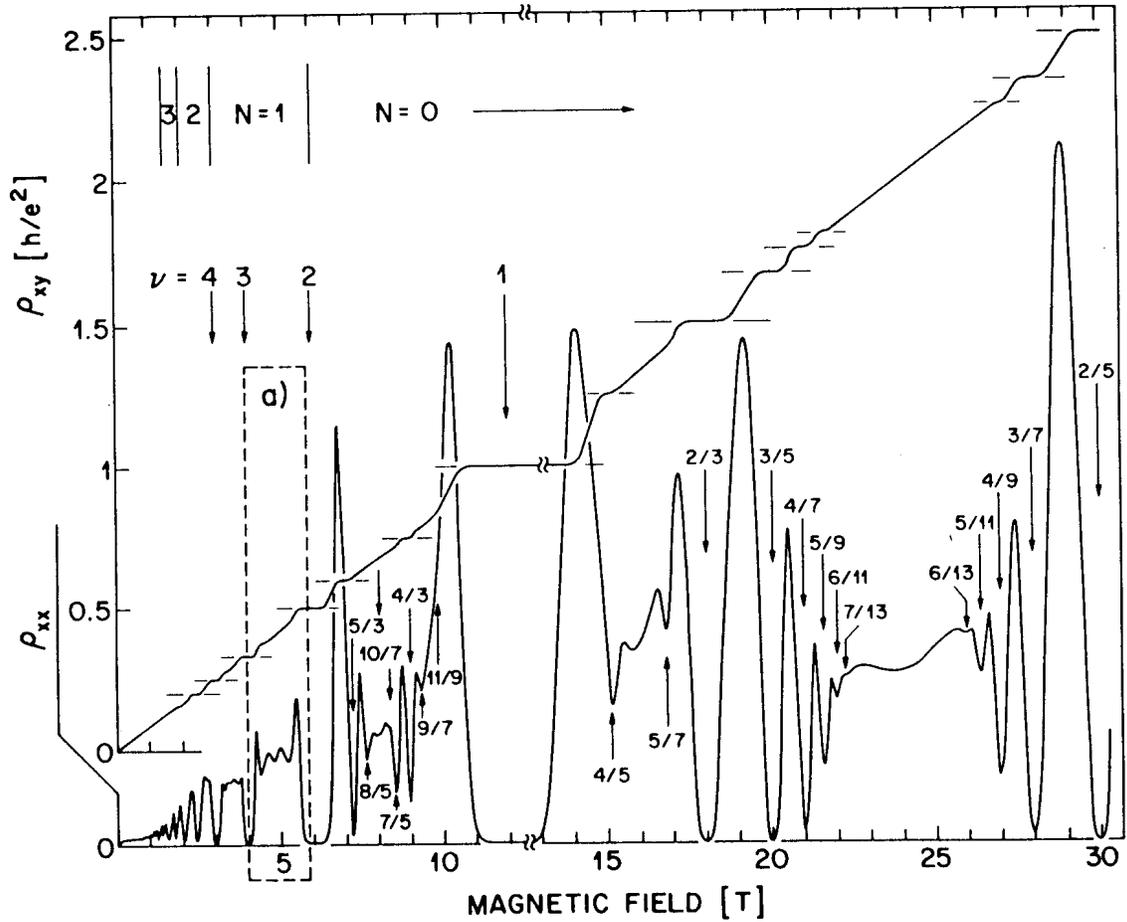
Figure 6.11: Present high-field, low-temperature ($T \sim 0.1$K) data on the FQHE (fractional quantum Hall effect) taken from a high mobility ($\mu \sim 1.3 \times 10^6$cm^2/V sec) quantum well sample of GaAs/Ga$_{1-x}$Al$_x$As. The familiar IQHE (integer quantum Hall effect) characteristics appear at filling factors of $\nu = 1, 2, 3, \ldots$. All fractional numbers are a result of the FQHE. Fractions as high as 7/13 are now being observed. [R. Willett, J.P. Eisenstein, H.L. Störmer, D.C. Tsui, A.C. Gossard, and J.H. English *Phys. Rev. Lett.* <u>59</u>, 1776 (1987)].

Chapter 7

Magnetic Ordering

References

- Ashcroft and Mermin, *Solid State Physics*, Chapters 32 & 33.

- Kittel, *Introduction to Solid State Physics*, 6th Ed., Chapter 15.

7.1 Introduction

Our discussion of magnetism up to this point has been concerned with weak magnetic interactions, corresponding to energies of less than 1 meV for magnetic fields of ~ 10 tesla. We shall now consider strong magnetic interactions where the magnetic moments on neighboring atomic sites interact with each other collectively and produce a magnetic ordering in the crystal. Various magnetic orderings are possible:

$$\uparrow\uparrow\uparrow\uparrow \qquad \text{ferromagnet}$$

ferromagnet – the magnetic moments (spins) all line up parallel to one another, and

$$\uparrow\downarrow\uparrow\downarrow \qquad \text{antiferromagnet}$$

antiferromagnet – equal magnetic moments (spins) on nearest neighbor sites which tend to line up antiparallel.

More complicated arrangements are possible like a

$$\Uparrow\downarrow\Uparrow\downarrow\Uparrow \qquad \text{ferrimagnet}$$

ferrimagnet which has a basic antiparallel arrangement of the magnetic moments (spins) but the magnitudes of the moments in the two directions are unequal, giving rise to a net magnetization. Various spiral arrangements of the moments can occur and canted arrangements of the moments are also common in real materials. These various forms of magnetism will be discussed in the next few lectures.

All these forms of magnetism have the following common features:

- At high temperatures they are all paramagnetic
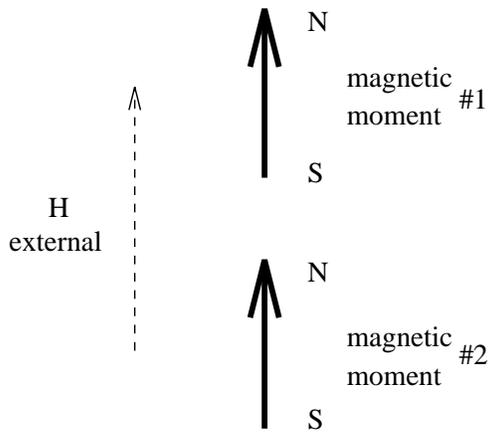
Figure 7.1: Schematic of dipole alignment in a magnetic field.

- Below an ordering temperature T_c, they all have ordered magnetic moments (spins).

We shall discuss the ferromagnetic ordering first because it is simplest, though similar arguments can be made for the other magnetically ordered systems. We will start in the paramagnetic regime with which we already have some familiarity.

7.2   The Weiss Molecular Field Model

In the magnetically ordered regime, we say that under the action of an external magnetic field $\vec{H}$, the total magnetization that is achieved depends not only on this applied field but on a <u>molecular</u> field $\vec{H}_M$ generated by the magnetization of the medium itself (see Fig. 7.1). $\vec{H}_{\text{total}}$ is called the mean field:

$$\vec{H}_{\text{total}} = (\vec{H} + \vec{H}_M). \tag{7.1}$$

The molecular field $\vec{H}_M$ is assumed to be proportional to the magnetization M:

$$\vec{H}_M = \lambda_M \vec{M} \tag{7.2}$$

and can be considered to arise from the other dipole moments in the medium (see Fig. 7.1). In the usual derivation of the Curie law (see §3.4), we assume that the magnetic field due to the other paramagnetic ions is small compared with the external magnetic field and we ignore $\vec{H}_M$ completely. For ferromagnetic systems $\vec{H}_M$ is very large, in fact much larger than the magnetic fields that are achieved in the laboratory.

For a strongly magnetic material in the paramagnetic region, the total magnetic field $\vec{H}_{\text{total}} = (\vec{H} + \vec{H}_M)$ tends to line up the magnetic moments along $\vec{H}_{\text{total}}$, while the thermal energy tends to randomize the motion. The derivation given for the magnetization (see Eq. 3.52) still holds except that the magnetic induction $\vec{B}$ includes the effect of both the applied field and the molecular field. From Eq. 3.52

$$M = N g \mu_B j \; B_j(x) \; ; \qquad x = \frac{g \mu_B j B}{k_B T} \tag{7.3}$$

90

where N is the atomic density and we now write

$$x = \frac{g\mu_B j \hat{\mu}(H + H_M)}{k_B T}; \qquad B = \hat{\mu}(H + H_M). \tag{7.4}$$

At high temperatures ($x \ll 1$), the susceptibility will be shown to follow the Curie–Weiss law. In this limit,

$$B_j(x) \sim x\left(\frac{j+1}{3j}\right) \tag{7.5}$$

$$M \simeq \left(\frac{Ng^2\mu_B^2(j+1)j\hat{\mu}}{3k_B T}\right)(H + H_M) = \left(\frac{C}{T}\right)(H + H_M) \tag{7.6}$$

where the Curie constant is:

$$C = \frac{Ng^2\mu_B^2 j(j+1)\hat{\mu}}{3k_B}. \tag{7.7}$$

Writing $H_M = \lambda_M M$, we obtain

$$M\left[1 - \frac{C\lambda_M}{T}\right] = \left(\frac{C}{T}\right)H \tag{7.8}$$

But $M = \chi H$ so that

$$\chi = \frac{C}{T}\frac{1}{(1 - \frac{C\lambda_M}{T})} = \frac{C}{T - C\lambda_M} \tag{7.9}$$

and we obtain the <u>Curie–Weiss Law</u>

$$\chi = \frac{C}{T - T_c} \tag{7.10}$$

which is valid for $T \gg T_c$ and in which the constant $C\lambda_M$, which is independent of T, defines the Curie temperature

$$T_c = C\lambda_M. \tag{7.11}$$

The Curie–Weiss law is valid only in the high temperature limit and is well satisfied for the common ferromagnetic materials in that limit. As an example, consider iron for which the ordering temperature is $1043K$ or $770°C$. The paramagnetic region occurs for T greater than the magnetic ordering temperatures and the Curie–Weiss law holds for temperatures much larger than $770°C$. Since the Curie–Weiss law does not hold at T_c, we do not expect the ordering temperature to be identical with T_c, the temperature at which the $\chi \to \infty$ on the Curie–Weiss picture. Nevertheless, a qualitative estimate for the magnitude of the molecular field can be made by identifying T_c with the ordering temperature.

7.3 The Spontaneous Magnetization

According to the molecular field model for a ferromagnet, the expression for the magnetization M in the paramagnetic region is (see Eq. 7.3):

$$M = Ng\mu_B j\, B_j(x) \tag{7.12}$$

where the argument x of the Brillouin function is

$$x = \frac{g\mu_B j\hat{\mu}(H + \lambda_M M)}{k_B T} \tag{7.13}$$

in which $H_M = \lambda_M M$ is written for the molecular field. Clearly this equation has a solution $M = 0$ for $H = 0$ and this solution exists for all temperatures which says that there is no net magnetization unless there is an applied magnetic field.

However, in ferromagnetic materials, a molecular field $H_M = \lambda_M M$ is present and a solution of this equation is possible even in zero magnetic field, provided that $\lambda_M M$ is large enough compared with $k_B T$. We will now see how to determine the value of M for which spontaneous magnetization occurs. That is, with no external field present, a small fluctuation in the local magnetization causes the neighboring moments to align, yielding further magnetization until an ordered state is formed and in this sense, the disordered state is unstable.

To find the spontaneous magnetization we set $H = 0$ in the Brillouin function which enters Eq. 7.12

$$M = Ng\mu_B j\, B_j(x') \tag{7.14}$$

where x' denotes the variable x when $H = 0$:

$$x' = \frac{g\mu_B j\hat{\mu}\lambda_M M}{k_B T}. \tag{7.15}$$

The simplest method to find a solution to Eq. 7.14 is the graphical method where we plot $Ng\mu_B jB_j(x') \equiv f(M)$ as a function of M. For a given material the initial slope increases as the temperature decreases, and for a given temperature the slope will only depend on the parameters of the particular magnetic material under consideration. The larger H_M (that is, the larger λ_M), the larger the initial slope. This curve for $f(M)$ must intersect the line $M = M$ if a solution to $M = Ng\mu_B jB_j(x') = f(M)$ exists. The solution to Eq. 7.14 is the intersection point in Fig. 7.2 which defines M_S, the spontaneous magnetization, and M_S is present with no applied magnetic field. This means that the intersection of the 45° straight line $M = M$ with the curve $f(M)$ will occur at higher values of the magnetization as T increases. However, since the Brillouin function $B_j(x')$ tends to saturate at high values of the argument x', the magnetization tends to reach a limiting value as $T \to 0$ which we will write as $M_S(0)$ and call the saturation magnetization. As the temperature increases, the initial slope of the right hand side of the equation decreases and $M_S(T)$ decreases and eventually goes to zero at a critical temperature T_c'. For $T = T_c'$ the initial slope of $f(M)$ is exactly unity. Thus for a given λ_M, the temperature T has to be lowered below a certain minimum value T_c' before spontaneous magnetization can occur. We use the prime on T_c' to distinguish T_c' from the Curie temperature T_c which enters the Curie–Weiss law. The temperature T_c' represents more closely our understanding of the transition to the ordered state. A plot of the observed temperature dependence of the spontaneous magnetization for nickel is given in Fig. 7.3. A qualitative fit of Eq. 7.14 to the experimental points is obtained, but the agreement is not quantitatively correct neither at low temperatures nor at high temperatures. A more sophisticated treatment of the internal magnetic field in a solid is required to provide a quantitative fit to the observed spontaneous magnetization curve.

Figure 7.2: Graphical solution of the equation for the Curie–Weiss model. The left-hand side of Eq. 7.14 is plotted as a straight line m with unit slope. The right-hand side of Eq. 7.14 involves the function $\tanh(m/t)$ which is plotted vs m where the reduced magnetization m is given by $m = M/(Ngj\mu_B)$. In the figure, plots are given for three different values of the reduced temperature $t = k_B T/N\mu_B^2 \lambda_M = T/T_c'$ for $s = 1/2$ and $g = 2$. The three curves correspond to the temperatures $2T_c'$, T_c', and $0.5T_c'$. The curve for $t = 2$ intersects the straight line m only at $m = 0$, as appropriate for the paramagnetic region (where the solution corresponds to zero external applied magnetic field). The curve for $t = 1$ (or $T = T_c'$) is tangent to the straight line m at the origin; this temperature marks the onset of ferromagnetism. The curve for $t = 0.5$ is in the ferromagnetic region and intersects the straight line m at about $m = 0.94N\mu_B$. As $t \to 0$ the intercept moves up to $m = 1$, so that all magnetic moments are lined up at absolute zero.

93
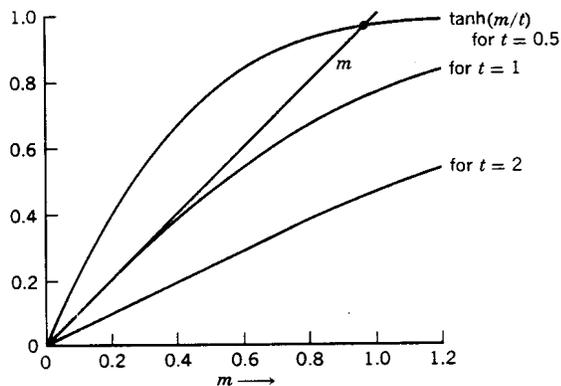
Figure 7.3: Phase diagram for a ferromagnetic system showing magnetization vs. T. The points are for Ni and the line is from mean field theory for $S = 1/2$.
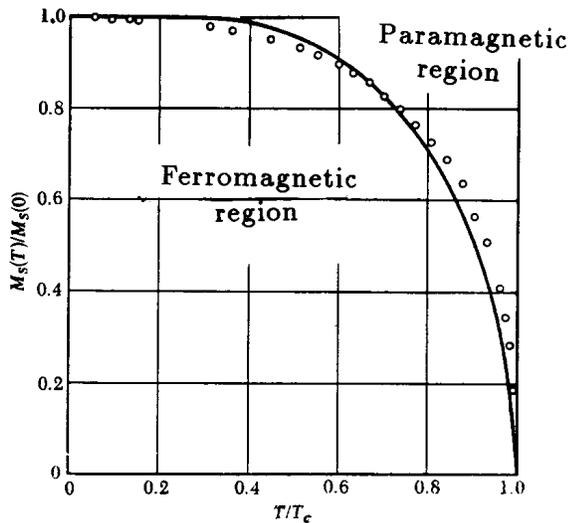
In Table 7.1, we summarize a few of the pertinent parameters for a few ferromagnetic materials. These ferromagnetic materials typically involve transition metal atoms and rare earth atoms with unfilled d or f shells. In Table 7.1, we see, in addition to the values for the spontaneous magnetization at 300 K and the saturation magnetization at 0 K and the transition temperature, values for n_B is the number of Bohr magnetons/atom. This number is defined through the saturation magnetization at $T = 0$ K and the ion density N

$$M_S(0) = n_B N \mu_B \tag{7.16}$$

since $B_j(\infty) = 1$ and therefore $M_S(0) = N g j \mu_B$ and

$$n_B = gj. \tag{7.17}$$

Inspection of Table 7.1 shows that by the definition of n_B in Eq. 7.17, n_B is not an integer.

For materials based on rare earth constituents, the number of Bohr magnetons per atom n_B calculated from $n_B = gj$ tends to be in good agreement with experiment. For example, gadolinium metal has Gd^{3+} ions in an $^8S_{7/2}$ configuration so that $g = 2$ and $j = 7/2$ and $n_B = 7$ are in good agreement with the experimental value of 7.10 given in Table 7.1. Similarly Dy is in a $^6H_{15/2}$ configuration yielding $j = 15/2$, $\ell = 5$ and $s = 5/2$ and $g = 4/3$, so that $n_B = gj = 10$ in good agreement with the value of 10.0 in Table 7.1.

In the case of the transition metals, the orbital angular momentum is largely quenched, so that $n_B \approx 2s$. The relation $n_B \approx 2s$ is only approximately obeyed because band theory applies to transition metals, and the Fermi level is determined by the condition that the total number of electrons for the $3d$ and $4s$ bands is integral. However, the occupation of each band individually corresponds to a non-integral number of electrons. For example, a simple model (due to Stoner) for the occupation of the $3d$ and $4s$ bands of metallic nickel was proposed many years ago to explain the non-integral number of Bohr magnetons/atoms (see Fig. 7.4). In this figure, we see occupation of the $4s$ and $3d$ bands of Ni in the paramagnetic and ferromagnetic phases using the Stoner model.

94

Table 7.1: Magnetic parameters for a number of ferromagnetic materials. Here n_B is the number of Bohr magnetons per atom and M_S is the spontaneous magnetization in units of gauss.

material	$M_S(300K)$	$M_S(0K)$	$n_B(0K)$	T_c (K)
Fe	1707	1740	2.22	1043
Co	1400	1446	1.72	1400
Ni	485	510	0.606	631
Gd	–	2010	7.10	292
Dy	–	2920	10.0	85
Cu_2MnAl	500	(550)	(4.0)	710
MnAs	670	870	3.4	318
MnBi	620	680	3.52	630
Mn_4N	183	–	1.0	743
MnSb	710	–	3.5	587
MnB	152	163	1.92	578
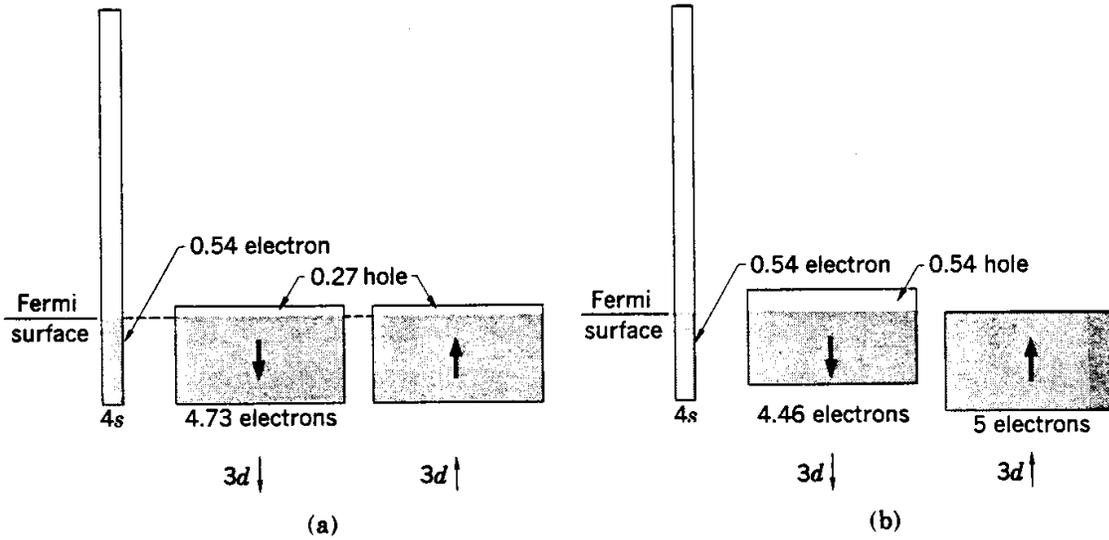
Figure 7.4: Schematic band filling diagram for (a) paramagnetic and (b) ferromagnetic nickel. (a) Band filling in nickel above the Curie temperature. The net magnetic moment is zero, as there are equal numbers of holes in both the $3d \downarrow$ and $3d \uparrow$ bands. In the ferromagnetic state (b) the bands have shifted so that there is an excess of spin up electrons and thus a net magnetization arising from the 0.54 hole in the $3d \downarrow$ band. In the ferromagnetic state, the energies of the $3d \uparrow$ and $3d \downarrow$ sub-bands are separated by an exchange interaction. The $3d \uparrow$ band is filled while the $3d \downarrow$ band contains 4.46 electrons and 0.54 holes. The $4s$ band is usually thought to contain approximately equal numbers of electrons in both spin directions, and therefore it is not necessary to specify any spin sub-bands. The net magnetic moment of $0.54\mu_B$ per atom arises from the excess population of the $3d \uparrow$ band over the $3d \downarrow$ band. It is often convenient to speak of the magnetization as arising from the 0.54 holes in the $3d \downarrow$ band.

96

Values for the spontaneous magnetization allow us to calculate the magnitude of the molecular field. Let us take the values in Table 7.1 for Fe and take $g = 2$, $j = 1$. For $3d$ transition metals, the orbital moment is quenched. From Table 7.1 we obtain $n_B = gj = 2.2$ for Fe. By setting the slope $(\partial f(M)/\partial M) = 1$, we define T'_c from Eq. 7.6 and solve for λ_M and make use of the relation $M_s = Ngj\mu_B$,

$$\lambda_M = \frac{3k_B T_c}{Ng^2 \mu_B^2 j(j+1)\hat{\mu}} = \frac{3k_B T_c}{M_s g \mu_B (j+1)\hat{\mu}} \tag{7.18}$$

which for Fe becomes $\lambda_M \sim 5000$. With $H_M \sim \lambda_M M_S$ ($M_S(0) = 1740$ gauss), we therefore obtain $H_M \sim 10^7$ gauss for the internal field in iron. This magnitude is much larger than any applied field we can generate in the laboratory. Thus, it is a good approximation for many magnetic materials to forget about H in comparison with H_M in computing H_{total} in the ferromagnetic state.

Let us think about that large magnitude of H_M more closely. The old picture of the Weiss molecular field (see §7.2) in terms of magnetic moments would give a dipole field of μ_B/a^3 which might be as much as 10^4 gauss at the position of the nearest magnetic moment, but hardly more than that. That is to say, the concept of magnetic dipoles as the mechanism responsible for the generation of an internal magnetic field of 10^7 gauss (10^3 Tesla) is inconsistent with the magnitude of the magnetic dipole-dipole interaction. To account for this strong magnetic field we need an electrostatic interaction of much larger magnitude than the magnetic dipole-dipole interaction. That is, microscopically the Weiss molecular field theory does not provide a satisfactory mechanism for generating H_M. Therefore, the Weiss molecular field theory provides a simple, useful, classical model for magnetism, but no explanation on a microscopic level for the origin of magnetism.

Such a microscopic model is provided by the Heisenberg Hamiltonian which was proposed about 25 years ago after the introduction of the molecular field theory by Weiss on the basis of quantum mechanics.

7.4 The Exchange Interaction

Ferromagnetism is a cooperative phenomenon – an isolated electron or ion cannot become ferromagnetic. To achieve the high internal fields required by the molecular field theory, an electrostatic interaction must be introduced. Such an interaction arises through so-called exchange effects which are associated with the Pauli principle and with the spin of the electron. We will now discuss the origin of the exchange interaction in atomic systems and then relate this exchange interaction to magnetism.

To understand the origin of the exchange interaction, consider the Hamiltonian for a 2-electron system

$$\mathcal{H} = \frac{p_1^2}{2m} + \frac{p_2^2}{2m} - \left(\frac{Ze^2}{r_1}\right) - \left(\frac{Ze^2}{r_2}\right) + \left(\frac{e^2}{|\vec{r}_1 - \vec{r}_2|}\right) = \mathcal{H}_1 + \mathcal{H}_2 + V_{12} \tag{7.19}$$

where

$$\mathcal{H}_1 = \frac{p_1^2}{2m} - \left(\frac{Ze^2}{r_1}\right) \tag{7.20}$$

$$\mathcal{H}_2 = \frac{p_2^2}{2m} - \left(\frac{Ze^2}{r_2}\right) \tag{7.21}$$

$$V_{12} = \frac{e^2}{|\vec{r}_1 - \vec{r}_2|}. \tag{7.22}$$

The one-electron Hamiltonians $\mathcal{H}_1(\vec{r}_1)$ and $\mathcal{H}_2(\vec{r}_2)$ can be solved directly each yielding an energy eigenvalue E_0, the energy for an electron in the field of a nucleus of charge Z.

On the other hand, the interaction term V_{12} expresses the Coulomb repulsion between the two electrons and cannot be simply written in terms of the one-electron wavefunctions which diagonalize $\mathcal{H}_1$ and $\mathcal{H}_2$. The Coulomb energy would be found approximately by perturbation theory using for our unperturbed states the eigenfunctions of $\mathcal{H}_1$ and $\mathcal{H}_2$ which are written as $\psi_1(\vec{r}_1)$ and $\psi_2(\vec{r}_2)$. We thus write the so-called Coulomb energy

$$C_{12} = \int \psi_1^*(\vec{r}_1)\psi_2^*(\vec{r}_2)\left(\frac{e^2}{|\vec{r}_1 - \vec{r}_2|}\right)\psi_1(\vec{r}_1)\psi_2(\vec{r}_2)d^3r_1 d^3r_2. \tag{7.23}$$

In writing down the states for a 2-electron system, we recognize that the two electrons are identical and indistinguishable. We are also required to satisfy the Pauli Exclusion Principle which states that the 2-electron wave function must be totally antisymmetric under the interchange of the 2 electrons (this is equivalent to saying that we cannot put two electrons in exactly the same state). In writing the wave function for an electronic system, we normally write the total wave function as a product of a spatial wave function with a spin function. In this situation, we have two options in making an antisymmetric state:

1. the spin function is symmetric and the spatial function is antisymmetric, or

2. the spin function is antisymmetric and the spatial function is symmetric.

The <u>symmetric two electron spin function</u> can be made in one of three ways:

$$\chi^S(1,1) = \alpha(1)\,\alpha(2) \tag{7.24}$$

$$\chi^S(1,-1) = \beta(1)\,\beta(2) \tag{7.25}$$

$$\chi^S(1,0) = \frac{1}{\sqrt{2}}[\alpha(1)\beta(2) + \alpha(2)\beta(1)] \tag{7.26}$$

where α denotes the spin up function and β the spin down function. The notation (1) and (2) in Eqs. 7.24–7.26 refers to spin coordinates for electrons 1 and 2, respectively. Electrons (1) and (2) are identical and cannot be distinguished in any other way. Thus the symmetric spin function is a <u>triplet</u> state which goes with the antisymmetric spatial wave function

$$\psi_{12}^A = \frac{1}{\sqrt{2}}[\psi_1(1)\psi_2(2) - \psi_1(2)\psi_2(1)] \tag{7.27}$$

where the (1) and (2) refer to $\vec{r}_1$ and $\vec{r}_2$ for electrons 1 and 2 and the subscript on ψ refers to the quantum numbers labeling the one-electron eigen-states of the unperturbed Hamiltonians $\mathcal{H}_1$ and $\mathcal{H}_2$.

On the other hand, the antisymmetric spin function can only be constituted in one way

$$\chi_{12}^A = \frac{1}{\sqrt{2}}[\alpha(1)\beta(2) - \alpha(2)\beta(1)] \tag{7.28}$$

98

and this forms a product with the symmetric spatial function

$$\psi_{12}^S = \frac{1}{\sqrt{2}}[\psi_1(1)\psi_2(2) + \psi_1(2)\psi_2(1)]. \tag{7.29}$$

Although the Hamiltonian in Eq. 7.19 does not contain any explicit dependence on the electron spin, the energy of the system will be different if we calculate the expectation value for the Coulomb repulsion energy V_{12} in the symmetric or antisymmetric spatial state. Explicitly this difference arises from

$$\frac{1}{2}\int[\psi_1^*(1)\psi_2^*(2) \pm \psi_1^*(2)\psi_2^*(1)]V_{12}[\psi_1(1)\psi_2(2) \pm \psi_1(2)\psi_2(1)]d^3r_1 d^3r_2 = C_{12} \pm J_{12} \tag{7.30}$$

where J_{12} is the so-called exchange energy defined as:

$$J_{12} \equiv \int \psi_1^*(1)\psi_2^*(2)[e^2/|\vec{r}_1 - \vec{r}_2|]\psi_1(2)\psi_2(1)d^3r_1 d^3r_2 \tag{7.31}$$

and $J_{12} = J_{21}$. If $J_{12} > 0$, the triplet state (with a symmetric spin function and an antisymmetric spatial function) lies lower. Here the spins are lined up and $S = 1$. For the singlet state we have $S = 0$. We then can write:

$$\vec{S} = \vec{S}_1 + \vec{S}_2 \tag{7.32}$$

so that

$$S^2 = (\vec{S}_1 + \vec{S}_2) \cdot (\vec{S}_1 + \vec{S}_2) = S_1^2 + S_2^2 + 2\vec{S}_1 \cdot \vec{S}_2. \tag{7.33}$$

Consider the eigenvalues for Eq. 7.33. For the triplet state, Eq. 7.33 yields

$$2\vec{S}_1 \cdot \vec{S}_2 = s(s+1) - s_1(s_1+1) - s_2(s_2+1) = 2 - (3/4) - (3/4) = \frac{1}{2} \tag{7.34}$$

and for the singlet state we write

$$2\vec{S}_1 \cdot \vec{S}_2 = 0 - (3/4) - (3/4) = -(3/2). \tag{7.35}$$

Therefore we can write

$$\left(\frac{1}{2}\right) + 2\vec{S}_1 \cdot \vec{S}_2 = 1 \tag{7.36}$$

for the spin symmetric (triplet) state, and

$$\left(\frac{1}{2}\right) + 2\vec{S}_1 \cdot \vec{S}_2 = -1 \tag{7.37}$$

for the spin antisymmetric (singlet) state, which allows us to write the expectation value for the Coulomb potential V_{12} as

$$\Delta E = C_{12} - \left(\frac{1}{2}\right)J_{12} - 2\vec{S}_1 \cdot \vec{S}_2 J_{12}. \tag{7.38}$$

The term $[-2\vec{S}_1 \cdot \vec{S}_2]J_{12}$ is called the Heisenberg Hamiltonian.

To see how to generalize the exchange interaction to more than one electron we write the wave function in the form of a determinant (called the Slater determinant) in which the

columns label the kinds of wave functions (e.g., a ls state with spin up) and the rows label the coordinates for each electron $\vec{x} = \vec{r}, \vec{\sigma}$, including both spatial and spin coordinates. The two electron wave function is thus written as

$$\psi(\vec{x}_1, \vec{x}_2) = \frac{1}{\sqrt{2}} \begin{vmatrix} \psi_1(\vec{x}_1) & \psi_1(\vec{x}_2) \\ \psi_2(\vec{x}_1) & \psi_2(\vec{x}_2) \end{vmatrix} \tag{7.39}$$

The determinantal form of this two electron wave function guarantees that two electrons in the same state give a null wave function. Two electrons in the same state would result in two identical rows in the determinant, thereby yielding a zero value. Expansion of the Slater determinant in Eq. 7.39 gives

$$\psi(\vec{x}_1, \vec{x}_2) = \frac{1}{\sqrt{2}}[\psi_1(\vec{x}_1)\psi_2(\vec{x}_2) - \psi_1(\vec{x}_2)\psi_2(\vec{x}_1)] \tag{7.40}$$

which gives rise to four antisymmetric wave functions (which we will denote by a subscript index). In particular we will show that this determinant is equivalent to the $\psi^A \chi^S$ and $\psi^S \chi^A$ wave functions given in Eqs. 7.24–7.29.

For example, if both electrons have the same spin functions α_1 and α_2 (both spin up or $\uparrow\uparrow$), then Eq. 7.40 becomes

$$\psi_1(\vec{x}_1, \vec{x}_2) = \left(\frac{1}{\sqrt{2}}\right)[\psi_1(\vec{r}_1)\alpha_1\psi_2(\vec{r}_2)\alpha_2 - \psi_1(\vec{r}_2)\alpha_2\psi_2(\vec{r}_1)\alpha_1]$$

$$= \alpha_1\alpha_2\left(\frac{1}{\sqrt{2}}\right)[\psi_1(\vec{r}_1)\psi_2(\vec{r}_2) - \psi_1(\vec{r}_2)\psi_2(\vec{r}_1)] \equiv \chi^S(1,1)\Psi^A \tag{7.41}$$

in which $\chi^S(1,1)$ denotes the symmetric spin state with $s = 1$ and $m_s = 1$. Similarly if both electrons are in the symmetric spin down state β_1 and β_2, then $s = 1$ and $m_s = -1$ so that in this case $\psi(\vec{x}_1, \vec{x}_2)$ in Eq. 7.40 becomes

$$\psi_2(\vec{x}_1, \vec{x}_2) = \beta_1\beta_2\left(\frac{1}{\sqrt{2}}\right)[\psi_1(\vec{r}_1)\psi_2(\vec{r}_2) - \psi_1(\vec{r}_2)\psi_2(\vec{r}_1)] \equiv \chi^S(1,-1)\Psi^A \tag{7.42}$$

More interestingly, when each electron is in a different spin state $\alpha_1\beta_2$ or $\beta_1\alpha_2$, then we can make the two possible linear combinations from $\psi(\vec{x}_1, \vec{x}_2)$, namely

$$\left(\frac{1}{2}\right)[\psi_1(\vec{r}_1)\alpha_1\psi_2(\vec{r}_2)\beta_2 - \psi_1(\vec{r}_2)\alpha_2\psi_2(\vec{r}_1)\beta_1] \pm \left(\frac{1}{2}\right)[\psi_1(\vec{r}_1)\beta_1\psi_2(\vec{r}_2)\alpha_2 - \psi_1(\vec{r}_2)\beta_2\psi_2(\vec{r}_1)\alpha_1] \tag{7.43}$$

in which the $+$ sign in Eq. 7.43 gives rise to a symmetric spin state with $s = 1$ and $m_s = 0$

$$\psi_3(\vec{x}_1, \vec{x}_2) = \left(\frac{1}{\sqrt{2}}\right)[\alpha_1\beta_2 + \alpha_2\beta_1]\left(\frac{1}{\sqrt{2}}\right)[\psi_1(\vec{r}_1)\psi_2(\vec{r}_2) - \psi_1(\vec{r}_2)\psi_2(\vec{r}_1)] \equiv \chi^S(1,0)\Psi^A \tag{7.44}$$

and the $-$ sign in Eq. 7.43 gives rise to an antisymmetric spin state with $s = 0$ and $m_s = 0$

$$\psi_4(\vec{x}_1, \vec{x}_2) = \left(\frac{1}{\sqrt{2}}\right)[\alpha_1\beta_2 - \alpha_2\beta_1]\left(\frac{1}{\sqrt{2}}\right)[\psi_1(\vec{r}_1)\psi_2(\vec{r}_2) + \psi_1(\vec{r}_2)\psi_2(\vec{r}_1)] \equiv \chi^A(1,0)\Psi^S. \tag{7.45}$$

For n electrons the Slater determinant (see Eq. 7.39) is written as

$$\Psi(\vec{x}_1 \ldots, \vec{x}_n) = \frac{1}{\sqrt{n!}} \begin{vmatrix} \psi_1(\vec{x}_1) & \psi_1(\vec{x}_2) & \ldots & \psi_1(\vec{x}_n) \\ \psi_2(\vec{x}_1) & \psi_2(\vec{x}_2) & \ldots & \psi_2(\vec{x}_n) \\ \vdots & \vdots & & \vdots \\ \psi_n(\vec{x}_1) & \psi_n(\vec{x}_2) & \ldots & \psi_n(\vec{x}_n) \end{vmatrix} \tag{7.46}$$

and this determinantal form of the wave function guarantees that no two electrons are in the same set of quantum states.

We now show that the Heisenberg Hamiltonian accounts for the large molecular fields which are encountered in ferromagnetic, antiferromagnetic and ferrimagnetic systems. The Heisenberg Hamiltonian is written as

$$\mathcal{H} = -2 \sum_{i,j}{}' J_{ij} \vec{S}_i \cdot \vec{S}_j \tag{7.47}$$

where the sum is over pairs of electrons. Suppose that we are only considering nearest neighbor interactions and all the neighbors are identical; assume that there are z such neighbors. Then Eq. 7.47 becomes

$$\mathcal{H} = -2z J_{ij} \vec{S}_i \cdot \vec{S}_j. \tag{7.48}$$

We will now show how the Heisenberg Hamiltonian gives rise to a relation for the mean or molecular field of the Weiss theory. The spin $\vec{S}_j$ can be identified with a magnetic moment $\vec{\mu}_j$ by the relation

$$\vec{\mu}_j = g\mu_B \vec{S}_j. \tag{7.49}$$

This magnetic moment sees a field $\vec{B}_j = 2\sum_i' J_{ij} \vec{S}_i / g\mu_B$ since $\mathcal{H} = -\sum_j \vec{\mu}_j \cdot \vec{B}_j$. If all the nearest neighbors are identical, then the effective magnetic field can be written as:

$$\vec{B}_j = \frac{2z J_{ij} \vec{S}_i}{g\mu_B}. \tag{7.50}$$

We will now identify this magnetic field with the molecular field. The spontaneous magnetization at $T = 0$ is achieved by writing

$$\vec{M}_S = N\vec{\mu}_j = Ng\mu_B \vec{S}_j \tag{7.51}$$

where N is the atomic density and $\vec{\mu}_j$ is the moment on each atom. Thus the molecular field can be written as

$$\hat{\mu} \lambda_M \vec{M}_S = \vec{B} = \frac{2z J_{ij} \vec{S}_i}{g\mu_B} = \frac{2z J_{ij} \vec{M}_S}{g\mu_B N g\mu_B} \tag{7.52}$$

so that

$$\vec{B} = \frac{2z J_{ij} \vec{M}_S}{Ng^2 \mu_B^2}. \tag{7.53}$$

From Eq. 7.52 we obtain

$$\lambda_M = \frac{2z J_{ij}}{Ng^2 \mu_B^2 \hat{\mu}}. \tag{7.54}$$

which provides us with an identification between λ_M and J_{ij}. Since the molecular field theory gives an independent value of λ_M, the exchange integral J_{ij} for spins on neighboring lattice sites can be estimated from the measured Curie temperature. From Eqs. 7.7 and 7.11 we have

$$\lambda_M = \frac{T_c}{C} = \frac{3k_B T_c}{N g^2 \mu_B^2 j(j+1)\hat{\mu}} \tag{7.55}$$

where C is the Curie constant (see Eq. 7.7) so that the exchange interaction from Eq. 7.54 and T_c from Eq. 7.55 can be related

$$J_{ij} = \frac{N g^2 \mu_B^2 \lambda_M \hat{\mu}}{2z} = (3/2)\frac{k_B T_c}{zj(j+1)}. \tag{7.56}$$

For iron, we have a BCC structure so that $z = 8$ for the magnetic species. From Table 7.1 we have $T_c = 1043\ K$ and because of the orbital quenching we can take $j = 1$. Thus we would estimate for the exchange interaction energy

$$J_{ij} \sim \frac{3}{2}\ \frac{0.024(1043/300)}{8(1)(2)}\ \text{eV} \sim 0.008\text{eV} \tag{7.57}$$

which is a reasonable value for an exchange interaction.

The Heisenberg Hamiltonian can be used to obtain the saturation magnetization directly and this type of analysis is carried out in great detail in a semester length course on magnetism. To the level of approximation given here, we identify $\lambda_M M_S$ with the internal field, usually called the Weiss Molecular Field, and the corresponding theory is called the Weiss Molecular Field Theory, which is the simplest approximation.

In the next order of approximation, we say that each spin is surrounded by a shell of nearest neighbor spins. We will treat the Heisenberg interaction explicitly for these spins, but will replace the effect of all the other spins acting on the nearest neighbors through an effective field $\vec{B}_{eff}$. The Hamiltonian for this next order approximation is then

$$\mathcal{H} = -2J\vec{S}_i \cdot \sum_{j=1}^{z} \vec{S}_j - g\mu_B \vec{B}_{eff} \cdot \sum_{j=1}^{z} \vec{S}_j - g\mu_B \vec{B} \cdot \vec{S}_i \tag{7.58}$$

where $\vec{S}_i$ is the central spin and the first term represents the effect of nearest neighbors which is treated explicitly. The second term in Eq. 7.58 represents the effect of all the spins in the nearest neighbor shell $\vec{S}_j$ on the outer shell of spins and is treated in terms of an effective field $\vec{B}_{eff}$. The last term in Eq. 7.58 represents the effect of the external field on $\vec{S}_i$. In this way the Heisenberg interaction is treated for a cluster (a central atom and its nearest neighbors) in an explicit manner and the interaction of the cluster with the external world is treated through an effective field. This effective field is determined through a consistency condition as for example requiring the magnetic moment on the central atom to be the same as that on the nearest neighbor sites. This method is known as the Bethe-Peierls-Weiss Method. It is also a mean field method except that here we treat a whole cluster of spins by the Heisenberg interaction, not only the central spin as in the Weiss molecular field theory.

In carrying out practical calculations involving the Heisenberg Hamiltonian, one often introduces an approximation to make the Heisenberg interaction a scalar interaction. This

Figure 7.5: Ordered arrangements of spins of the Mn^{2+} ions in MnO, as determined by neutron diffraction. The lattice for MnO is a NaCl structure, though the O^{2-} ions are not shown in the figure. The chemical and magnetic unit cells are indicated in the figure.

Magnetic
unit cell

Chemical
unit cell
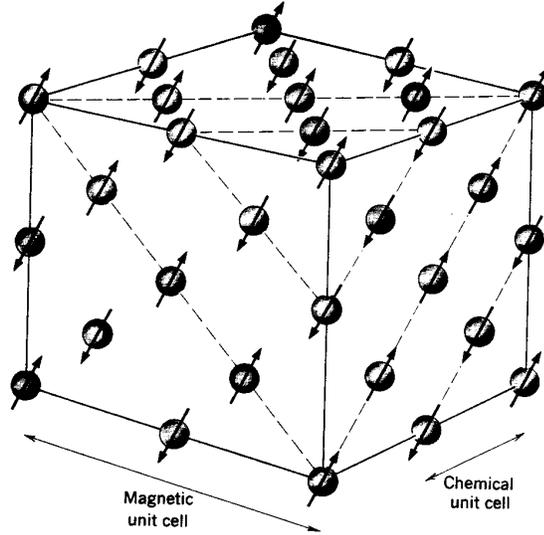
is called the <u>Ising model</u>. The Heisenberg Hamiltonian can be written in terms of vector components as

$$\mathcal{H} = -2\sum{}' J_{ij}\vec{S}_i \cdot \vec{S}_j = -2\sum{}' J_{ij}(S_{xi}S_{xj} + S_{yi}S_{yj} + S_{zi}S_{zj}) \tag{7.59}$$

where the prime on the summation indicates a sum over electron pairs. The assumption that is made to obtain the Ising model is that the x and y components S_x and S_y average to zero. That is, only along the axis of quantization do we expect a time average value for $\vec{S}_i \cdot \vec{S}_j$ to be different from zero. This approximation is a gross oversimplification, but it makes the mathematics much easier and is usually used as a first order approximation. That is, according to the <u>Ising model</u>, the Heisenberg Hamiltonian is written as a scalar interaction

$$\mathcal{H} = -2\sum{}' J_{ij}S_{zi}S_{zj} \tag{7.60}$$

where the z direction is along the magnetization direction. Another case of interest is the xy model for which the spins are constrained to lie in the xy plane normal to the axis of quantization.

7.5   Antiferromagnetism and Ferrimagnetism

We would now like to make some comments on the molecular field theory as applied to <u>ferrimagnetic</u> and <u>antiferromagnetic</u> systems. In a ferromagnet, the exchange energy is positive $J > 0$ so that the ground state is an ordered state with all the spins lined up. In an antiferromagnet, $J < 0$, the spins are lined up antiparallel in the ordered state as shown in Fig. 7.5 for MnO (which crystallizes in the NaCl structure). To describe an antiferromagnet, it is convenient to introduce two sublattices: an A sublattice for the spin↑ sites and a B sublattice for the spin ↓ sites, for example. In terms of these sublattices we

103

will now discuss the Curie–Weiss law on the basis of the molecular field theory presented in §7.2 for ferromagnetic systems.

Having introduced the antiferromagnet in terms of this 2-sublattice picture, it is a simple extension to define the ferrimagnet as a material where the size of the individual magnetic moments on the 2 sublattices, though opposite in sign, are of different magnitudes. Consider magnetite which is Fe_3O_4 and crystallizes in the spinel structure where 1/3 of the iron atoms are on tetrahedral A sites, and the other 2/3 on octahedral B sites. Different exchange integrals J_{AA}, J_{AB}, J_{BB} govern the interactions between Fe atoms depending on which sublattices each of the Fe atoms is located. This physical situation can be represented in terms of the molecular fields $\vec{H}_A$ and $\vec{H}_B$ which depend on the magnetization $\vec{M}_A$ and $\vec{M}_B$ for each of the sublattices:

$$\vec{H}_A = -\lambda_{M_{AA}}\vec{M}_A - \lambda_{M_{AB}}\vec{M}_B \tag{7.61}$$

$$\vec{H}_B = -\lambda_{M_{BA}}\vec{M}_A - \lambda_{M_{BB}}\vec{M}_B \tag{7.62}$$

The minus signs indicate that the molecular fields are antiparallel to the applied field. The minus sign is associated with antiferromagnetic interactions ($J < 0$) between ions on the A and B sublattices and on the same sublattices (A and A) or (B and B).

By reciprocity $\lambda_{M_{BA}} = \lambda_{M_{AB}}$. The interpretation of these relations is that the molecular field $\vec{H}_A$ is determined by both the nearest neighbor interaction with sublattice B and by the next nearest neighbor interaction with sublattice A. In contrast, for a ferromagnet we have $\vec{H}_A = \vec{H}_B$, there are no sublattices, and we have only one molecular field constant λ_M, even though we may consider interactions beyond the nearest neighbor interaction. For a simple antiferromagnet, we have two sublattices and if we consider only nearest neighbor interactions, then the molecular fields are simply written as

$$\vec{H}_A = -\lambda_{M_{AB}}\vec{M}_B, \qquad \vec{H}_B = -\lambda_{M_{AB}}\vec{M}_A. \tag{7.63}$$

Reciprocity still requires that the coupling of sublattice A to that of B be consistent with that of B to A, and hence the same molecular field constant $\lambda_{M_{AB}}$ appears in both equations of Eq. 7.63.

Returning now to a ferrimagnet, the arguments presented following Eq. 7.14 can be applied to each sublattice independently. For the individual sublattices, the analysis of §7.2 yields a Curie law:

$$M_A = \left(\frac{C_A}{T}\right) H_{A\,total} = \left(\frac{C_A}{T}\right)(H - \lambda_{M_{AA}}M_A - \lambda_{M_{AB}}M_B) \tag{7.64}$$

$$M_B = \left(\frac{C_B}{T}\right) H_{B\,total} = \left(\frac{C_B}{T}\right)(H - \lambda_{M_{AB}}M_A - \lambda_{M_{BB}}M_B) \tag{7.65}$$

where

$$C_A = \frac{N_A g^2 \mu_B^2 j(j+1)\hat{\mu}}{3k_B}, \tag{7.66}$$

and likewise for C_B. Here H is the applied magnetic field, C_A and C_B are the Curie constants for sublattices A and B, the $\lambda_{M_{AB}}$ coefficients represent the internal field arising from nearest neighbor interactions and the $\lambda_{M_{AA}}$ and $\lambda_{M_{BB}}$ coefficients represent contributions from second neighbor interactions on the same sublattice. Equations 7.64 and 7.65 represent two

coupled linear equations which have a non-trivial solution when the coefficient determinant for the variables M_A and M_B vanishes. This condition determines the ferrimagnetic Curie temperature

$$\begin{vmatrix} T_c + C_A \lambda_{M_{AA}} & \lambda_{M_{AB}} C_A \\ \lambda_{M_{AB}} C_B & T_c + \lambda_{M_{BB}} C_B \end{vmatrix} = 0. \tag{7.67}$$

This is a quadratic equation which can always be solved exactly to obtain T_c. The susceptibility is related to the total magnetization and is defined by the equation:

$$\chi = \frac{M_A + M_B}{H}. \tag{7.68}$$

This relation can also be evaluated explicitly by solving the simple coupled equations. The result is rather messy for the case of a ferrimagnet.

However, for the antiferromagnetic case, the result is quite simple. Assuming that only the nearest neighbor interaction contributes to the magnetization, we can write $\lambda_{M_{AA}} = 0$, $\lambda_{M_{BB}} = 0$, $C_A = C_B = C$

$$\begin{vmatrix} T_c & \lambda_{M_{AB}} C \\ \lambda_{M_{AB}} C & T_c \end{vmatrix} = 0 \tag{7.69}$$

or $T_c = \lambda_{M_{AB}} C$. For simplicity, let us write $\lambda_{M_{AB}} = \lambda_M$ in Eq. 7.69. Therefore

$$M_A = \left(\frac{C}{T}\right)(H - \lambda_M M_B) \tag{7.70}$$

$$M_B = \left(\frac{C}{T}\right)(H - \lambda_M M_A) \tag{7.71}$$

$$M_B = \left(\frac{C}{T}\right)[H - \left(\lambda_M \frac{C}{T}\right)(H - \lambda_M M_B)] \tag{7.72}$$

$$M_B(1 - \lambda_M^2 C^2 / T^2) = \left(\frac{C}{T}\right)\left(1 - \lambda_M \frac{C}{T}\right)H \tag{7.73}$$

$$M_B\left(1 + \lambda_M \frac{C}{T}\right) = \frac{CH}{T} \tag{7.74}$$

$$M_B = \frac{CH}{(T + \lambda_M C)} \tag{7.75}$$

where

$$T_c = \lambda_M C \quad \text{and} \quad C = \frac{N g^2 \mu_B^2 j(j+1)\hat{\mu}}{3 k_B}. \tag{7.76}$$

Similarly

$$M_A = \frac{CH}{(T + \lambda_M C)} \tag{7.77}$$

so that

$$M = M_A + M_B = 2\frac{CH}{(T + \lambda_M C)} \tag{7.78}$$

yielding

$$\chi = \frac{2C}{(T + T_c)} \tag{7.79}$$

105

Figure 7.6: Temperature dependence of the magnetic susceptibility in paramagnets, ferromagnets, and antiferromagnets. Below the Néel temperature of an antiferromagnet, the spins have antiparallel orientations; the susceptibility attains its maximum value at T_N where there is a well-defined kink in the curve of χ versus T. The phase transition is also marked by peaks in the heat capacity and the thermal expansion coefficient. The dashed extrapolated curve for the antiferromagnetic case is not physical below T_N.
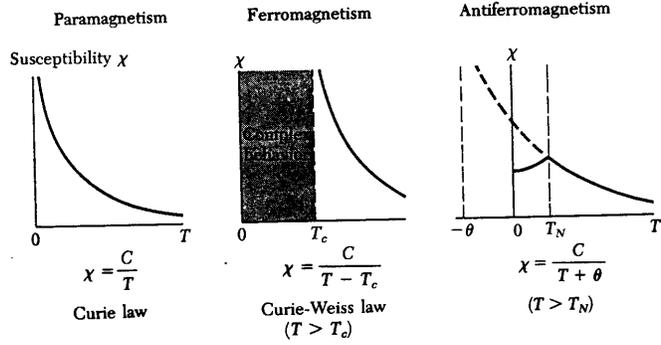
where

$$T_c = \lambda_M C. \tag{7.80}$$

Equation 7.79 is in the form of the Curie–Weiss law where the susceptibility diverges for $T = -T_c$ (see Fig. 7.6).

If we plot χ vs. T for an antiferromagnet, we distinguish:

1. The paramagnetic region above the antiferromagnetic ordering temperature T_N, the Néel temperature. The Curie–Weiss law given in Eq. 7.79 holds for $T \gg T_N$.

2. The temperature $-T_c$ below $T = 0$ K at which the extrapolated susceptibility function diverges as shown in Fig. 7.6. In this figure we show the susceptibility in the paramagnetic regime for ferromagnetic, antiferromagnetic and paramagnetic materials.

From this discussion we see that the susceptibility relation for antiferromagnetic materials is very similar to that for ferromagnetic materials. In both cases there is a temperature $T_{critical}$ below which there is an onset of the magnetic state. For the ferromagnetic case, T_c and $T_{critical}$ would be the same if the Curie law were to be valid all the way down to the transition temperature; but since significant departures from the Curie law occur, there are two different temperature parameters to be considered as shown in Fig. 7.7 for nickel (a ferromagnet). While these two parameters are quite close for a ferromagnetic material, the situation for antiferromagnets is quite different. Here T_c and T_N are <u>not</u> simply related by $|T_c| \sim |T_N|$, where T_N is the Néel temperature, denoting the onset of antiferromagnetism. Sometimes these two quantities are of the same magnitude – e.g., MnF_2 has $T_N = 67$ K and $T_c = 82$ K. They can also be quite different – e.g., FeO has $T_N = 198$ K and $T_c = 570$ K.

In discussing ferromagnetism, we have found two quantities to be of particular significance – the critical temperature and the saturation (or spontaneous) magnetization. For the antiferromagnetic case, we still have a critical temperature, though no saturation magnetization. Since half of the spins point in one direction and half point the opposite way,

106

Figure 7.7: Plot of the reciprocal susceptibility per gram vs T of Ni (points) in the neighborhood of the Curie–Weiss temperature ($T_c = 358$K), and the dashed curve shows an extrapolation of the Curie–Weiss law from high temperatures. Here ρ denotes the mass density.
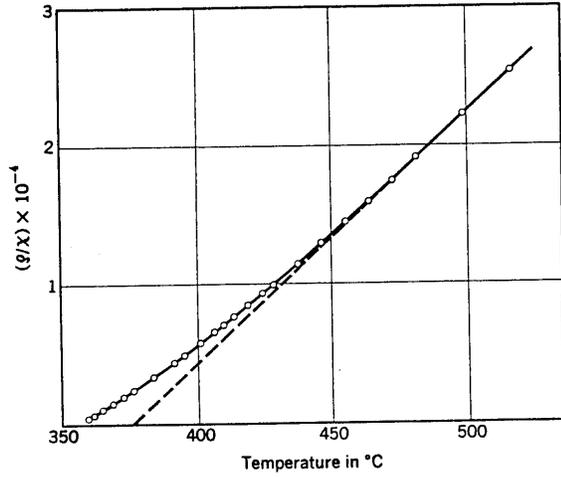
Figure 7.8: Schematic calculation of the effect of an applied field H on the magnetization, where $\vec{H}$ is (a) perpendicular and (b) parallel to the sublattice magnetizations M_A and M_B at 0 K, in the mean field approximation.
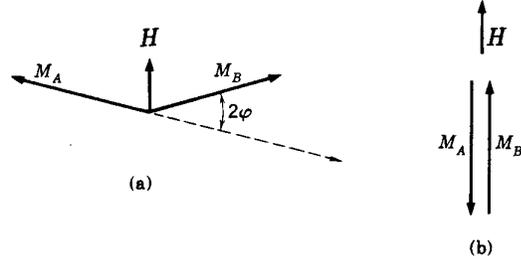
we have $M_A = M_B$ (which can be considered as the order parameter is also called the staggered magnetization). Thus, there is no net magnetic moment per unit volume. There is, however, some susceptibility, but the susceptibility now depends upon the direction between the applied magnetic field $\vec{H}$ and the magnetization of the sublattices.

In the parallel orientation, where the applied field $\vec{H}$ is parallel to the sublattice magnetization (see Fig. 7.8b), we have $M_A = M_B$ at $T = 0$ K, and H has no effect on the magnetization because $H \ll M_A, M_B$. Thus, for this case, we have the result $\chi_B \to 0$ as $T \to 0$ K.

In the perpendicular orientation, where the applied field $\vec{H}$ is normal to the sublattice magnetization (see Fig. 7.8a), however, the effect of the magnetic field is to try to orient the sublattice magnetization along the applied field. If the molecular field constants are large, then a large applied field is needed, while if $\lambda_{M_{AB}}$ is smaller, then a modest applied field will be effective in creating a net magnetization. Thus

$$\chi_\perp \to \frac{1}{\lambda_{M_{AB}}} \tag{7.81}$$

as $T \to 0$ K and the susceptibility for an antiferromagnetic material in the ordered antiferromagnetic region has two branches as shown on the diagram in Fig. 7.9 for MnF$_2$, a

Figure 7.9: Magnetic susceptibility of MnF_2, parallel and perpendicular to the tetragonal axis.
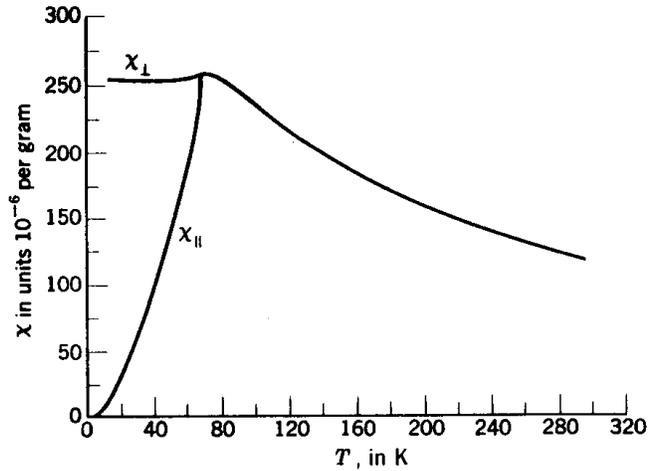
typical antiferromagnetic material.

At this point we might ask whether there is a simple way to tell whether a material will be ferromagnetic or antiferromagnetic from first principles. Generally speaking, this is difficult to predict, although some arguments can be given which tend to apply. To make a magnetic state, the exchange integral must be large and to accomplish this, we need orbitals that stick out from the atom sites (like d-orbitals). These electronic orbitals give rise to bonding as well, since the electrons tend to spend more time in the region between two atoms than away from these atoms. If the electrons on neighboring atoms tend to be in the same spatial location, it is energetically favorable for them to have their spins antiparallel. If we have atoms with d-shells that are less than half-full we can arrange to have the spins on neighboring atoms antiparallel. Thus, if the d-shells are less than half-filled, antiferromagnetic ordering is preferred. On the other hand, if we have atoms with d-shells that are more than half-filled, we cannot always arrange the spins to be antiparallel on neighboring sites, because most of the states are already filled in making the atomic configuration. Thus the spins on neighboring atoms tend to be aligned parallel to each other and more than half-filled shells tend to favor ferromagnetism. From measurement of the Curie–Weiss law and the sign of T_c in the paramagnetic region (Eq. 7.79), we can usually distinguish between materials that will order magnetically, and if the ordering will be ferromagnetic or antiferromagnetic.

7.6   Spin Waves

In the ground state (or lowest energy state) at $T = 0\ K$, all the spins in a ferromagnet tend to be aligned parallel to one another (see Fig. 7.10a). At a finite temperature, some of the spins will become misaligned, as for example by thermal excitation, and an excited state is produced. We might imagine that the lowest energy excited state could be achieved by flipping one spin, and this is represented schematically by Fig. 7.10b. Let us now consider how much energy it takes to flip this spin. If we only include nearest neighbor exchange

108
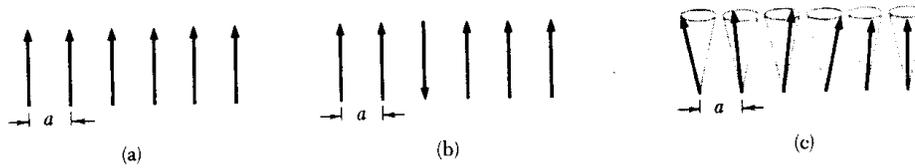
Figure 7.10: (a) Classical picture of the ground state of a simple ferromagnet; all spins are parallel. (b) A possible excitation; one spin is reversed. (c) The low-lying elementary excitations are spin-waves. The ends of the spin vectors precess on the surfaces of cones, with successive spins advanced in phase by a constant angle.
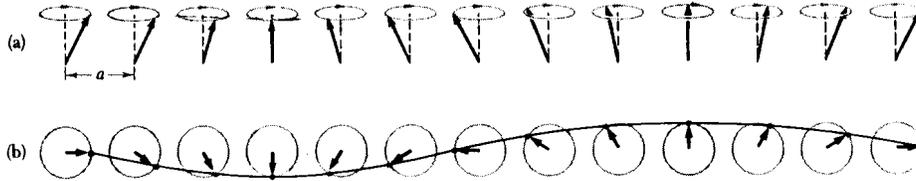
Figure 7.11: Schematic of a spin wave on a line of spins. (a) The spins viewed in perspective. (b) Spins viewed from above, showing one wavelength. The wave is drawn through the ends of the spin vectors.

interactions, the Heisenberg Hamiltonian becomes

$$\mathcal{H} = -2J \sum_{n=1}^{N'} \vec{S}_n \cdot \vec{S}_{n+1}. \tag{7.82}$$

When written in this form, we note that J has the units of energy so that $\vec{S}$ is dimensionless and for this reason the spin angular momentum is $\hbar\vec{S}$. For the ground state energy $E_{G.S.}$ for the N aligned spins (each with spin $1/2$) we can write

$$E_{G.S.} = -2(N-1)JS^2 \tag{7.83}$$

where $(N-1)$ is the number of spin pairs. To flip one spin (some interior spin) we change the interaction energy between two pairs from $-2JS^2$ to $+2JS^2$, so for each pair we effect a change of $4JS^2$ and for the two pairs we produce a net increase in energy of $8JS^2$. It is clear that when the spin flip is made gradually, the net increase in energy can be smaller. Thus a wave-like spin flip occurs, called a spin wave and is shown schematically in Fig. 7.11 for two views of the spin wave. We will now show that the dispersion relations for spin waves in a ferromagnetic system are of the form $\omega \sim k^2$ (for small k) whereas for lattice vibrations $\omega = vk$ (where v is the velocity of sound). Of course, for the electron system, the dispersion relations for a simple metallic band are also of the form $\omega \sim k^2$

$$E(\vec{k}) = \frac{\hbar^2 k^2}{2m^*}. \tag{7.84}$$

109

A simple derivation of the spin-wave dispersion relation is given in Kittel ISSP and is reproduced here. The identification of the Heisenberg Hamiltonian is made by looking at the pth site. Here we have a spin $\vec{S}_p$ with a magnetic moment given by

$$\vec{\mu}_p = g\mu_B \vec{S}_p \tag{7.85}$$

in which $\vec{S}_p$ has been written in dimensionless units. Spin p sees a magnetic field due to its neighbors on either side:

$$\vec{H}_p = \left(\frac{2J}{g\mu_B}\right)(\vec{S}_{p-1} + \vec{S}_{p+1}). \tag{7.86}$$

where $\vec{H}_p$ denotes the exchange field or molecular field and $\vec{H}_p = \lambda_M \vec{M}_p$. In the derivation we make use of the relation that the time rate of change of angular momentum is the torque $\vec{\mu}_p \times \vec{H}_p$ so that we obtain

$$\hbar\left(\frac{d\vec{S}_p}{dt}\right) = \vec{\mu}_p \times \vec{H}_p \tag{7.87}$$

which upon substitution of $\vec{H}_p$ from Eq. 7.86 and $\vec{\mu}_p$ from Eq. 7.85 yields:

$$\frac{d\vec{S}_p}{dt} = \left(\frac{g\mu_B}{\hbar}\right)\vec{S}_p \times \left[\frac{2J}{g\mu_B}(\vec{S}_{p-1} + \vec{S}_{p+1})\right] = \left(\frac{2J}{\hbar}\right)\vec{S}_p \times (\vec{S}_{p-1} + \vec{S}_{p+1}). \tag{7.88}$$

We will now write Eq. 7.88 in Cartesian coordinates with $\hat{z}$ chosen as the alignment direction for the spins in the ground state. Assuming that the spin wave represents a small perturbation, we assume that S_x and S_y are small in comparison to S_z so that products of the form $S_x^2, S_x S_y$ and S_y^2 will be neglected in comparison with $S_z^2, S_x S_z, S_y S_z$. We will also assume that $S \sim S_z$ resulting in linearized classical equations of motion (neglecting quantum mechanical properties of $\vec{S}$)

$$\frac{dS_p^x}{dt} = \left(\frac{2JS}{\hbar}\right)(2S_p^y - S_{p-1}^y - S_{p+1}^y) \tag{7.89}$$

$$\frac{dS_p^y}{dt} = -\left(\frac{2JS}{\hbar}\right)(2S_p^x - S_{p-1}^x - S_{p+1}^x) \tag{7.90}$$

$$\frac{dS_p^z}{dt} = 0. \tag{7.91}$$

Solutions to these equations of motion can be written in the traveling wave form:

$$S_p^x = ue^{i(pka-\omega t)} \tag{7.92}$$

and

$$S_p^y = ve^{i(pka-\omega t)} \tag{7.93}$$

where u and v are amplitudes for the spins in the x and y directions, respectively, k is a wave vector and a is a lattice constant. Substitution of these harmonic solutions into the differential equations (Eqs. 7.89 and 7.90) results in

$$-i\omega u = \left(\frac{2JS}{\hbar}\right)(2 - 2\cos ka)v \tag{7.94}$$

110

Figure 7.12: Dispersion relation for spin waves in a one dimensional ferromagnet considering only nearest-neighbor interactions.
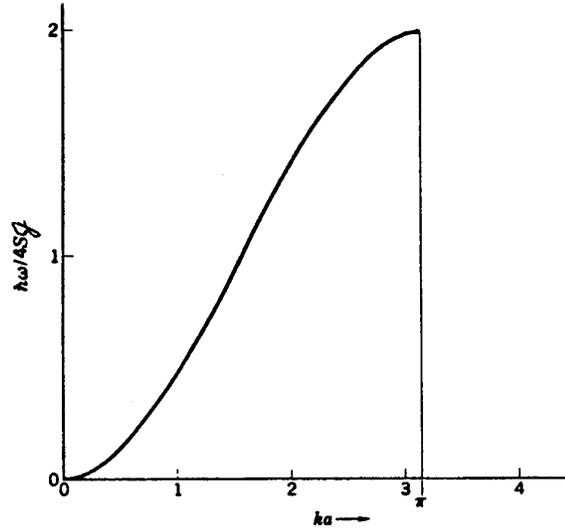
$$-i\omega v = -\left(\frac{2JS}{\hbar}\right)(2 - 2\cos ka)u \tag{7.95}$$

which has a solution when the coefficient determinant vanishes or

$$\begin{vmatrix} i\omega & \left(\frac{4JS}{\hbar}\right)(1 - \cos ka) \\ -\left(\frac{4JS}{\hbar}\right)(1 - \cos ka) & i\omega \end{vmatrix} = 0 \tag{7.96}$$

which gives the equation

$$\omega^2 = \left[\left(\frac{4JS}{\hbar}\right)(1 - \cos ka)\right]^2, \tag{7.97}$$

so that

$$\hbar\omega \simeq 2JSa^2k^2 \tag{7.98}$$

which is valid for $ka \ll 1$. A plot of the dispersion relation for a ferromagnetic spin wave is shown in Fig. 7.12. The initial slope is not constant as it is for the case of lattice vibrations. Instead, for ferromagnetic spin waves the dispersion curve comes into $k = 0$ with zero slope as shown in Fig. 7.12.

The interpretation of the wave vector for spin waves can be understood from the diagram in Fig. 7.13. For a given mode labeled by wave vector k, the angle between neighboring spins is seen to be $\phi = ka$. On the other hand, the situation for spin waves and for lattice vibrations is similar, in that quantum mechanics restricts the kinds of possible excitations. In particular, S_z can change only by integral units of $\hbar$ in creating a spin wave. This quantization condition results in the magnon, which (like the phonon) is a unit of possible excitation of the magnetic system. Thus we can write the excitation energy of magnons at wave vector $\vec{k}$ as

$$E_k = n_k \hbar \omega_k \tag{7.99}$$

111
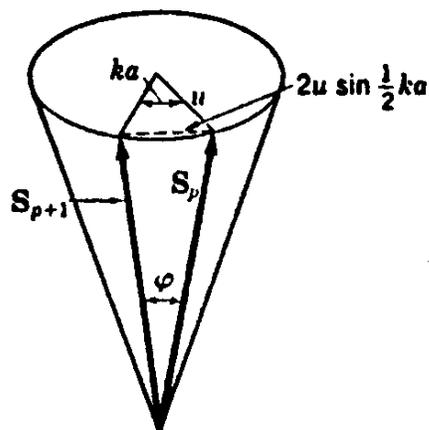
Figure 7.13: Construction relating the angle ϕ between two successive spin vectors to the spin wave amplitude u and phase angle ka. The length of the dashed line is $2u\sin(ka/2)$. If the length of a spin is S, then it follows that $S\sin(\phi/2) = u\sin(ka/2)$.

where n_k is the number of magnons at wave vector $\vec{k}$ and ω_k is the energy per magnon where ω_k and k are related by the dispersion relation

$$\omega_k = (4JS/\hbar)(1 - \cos ka). \tag{7.100}$$

A typical magnon spectrum for a ferromagnetic material is shown in Fig. 7.14. This spectrum was taken using neutron scattering techniques. Neutron diffraction techniques are very important in studying magnetic materials because the neutron itself has a magnetic moment which is sensitive to the ordering of the magnetic moments in the magnetic material. In contrast, x-rays are scattered predominantly by the electronic charges about each atomic site, and magnetic effects are only observed in higher order interactions. Thus the elastic scattering of neutrons gives information on the magnetic structure of the magnetic unit cell.

If we use as our neutron probe a beam of thermal neutrons with de Broglie wavelengths comparable to lattice dimensions, we can also observe the inelastic scattering of neutrons whereby a magnon is created (or absorbed) (see Fig. 7.15). The magnon spectrum in Fig. 7.14 was obtained using the inelastic neutron scattering technique. Inelastic light scattering processes also occur, and therefore magnon spectra can also be studied by the Raman effect. Because of the small k vector for light, the Raman effect is most sensitive to magnons with small wavevector (see Fig. 7.15). To find the mean energy due to spin wave excitations at a given temperature we must take a thermal average, as we did for phonons in finding the heat capacity. The number of magnons excited at a given temperature is given by the Bose factor

$$n_k = \frac{1}{(e^{\hbar\omega_k/k_B T} - 1)}. \tag{7.101}$$

where k_B is Boltzmann's constant

To find the total number of magnons excited at a temperature T, we have to perform a sum over states, which is more readily done as a function of frequency ω_k. Making use of the density of states function

$$\rho(\omega_k)\,d\omega_k = \frac{1}{(2\pi)^3}4\pi k^2\left(\frac{dk}{d\omega_k}\right)d\omega_k \tag{7.102}$$

112

Figure 7.14: Magnon dispersion curve of a FCC cobalt alloy (92% Co, 8% Fe) at room temperature as measured by neutron scattering.
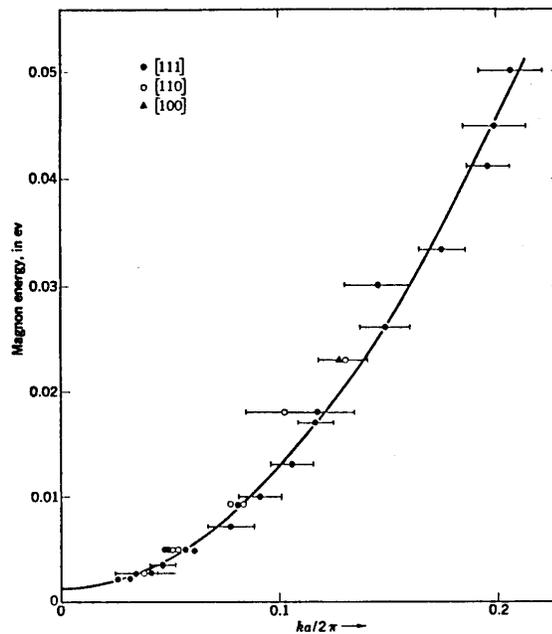
Figure 7.15: Schematic diagram for inelastic neutron scattering.

113
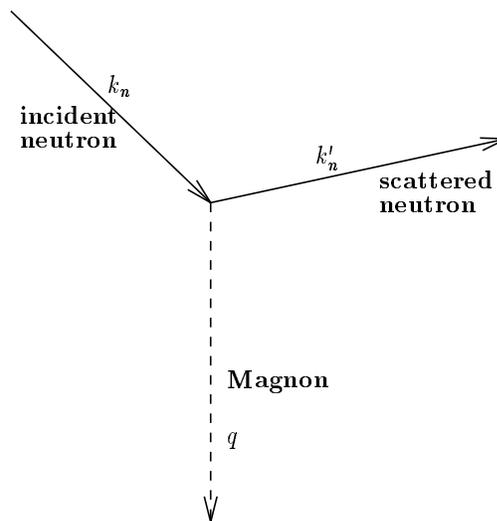
and the weighted magnon density is found from

$$\sum_k n_k = \int n_k \rho(\omega_k) d\omega_k. \tag{7.103}$$

From the spin wave or magnon dispersion relation given in Eq. 7.100, we have

$$\frac{d\omega_k}{dk} = \left(\frac{4JS}{\hbar}\right) a \sin ka \sim \frac{4JS}{\hbar} a^2 k \tag{7.104}$$

The small k approximation (for $ka \ll 1$) of Eq. 7.104 is useful because at temperatures where the spin wave theory applies, it is predominantly the small k magnons which are excited, so that

$$\omega_k = \left(\frac{4JS}{\hbar}\right)(1 - \cos ka) \sim \left(\frac{2JS}{\hbar}\right) k^2 a^2 \tag{7.105}$$

and

$$k \sim \left(\frac{1}{a}\right)\sqrt{\frac{\hbar\omega_k}{2JS}}. \tag{7.106}$$

Thus the total number of magnons excited at low temperature will be

$$\sum_k n_k \simeq \frac{1}{2}\pi^2 \int \frac{(\hbar k d\omega_k)}{(4JSa^2)(e^{\hbar\omega_k/k_B T} - 1)} \tag{7.107}$$

which becomes

$$\sum_k n_k = \left(\frac{\hbar}{8\pi^2 JSa^3}\right)\sqrt{\frac{\hbar}{2JS}} \int \frac{\omega_k^{\frac{1}{2}} d\omega_k}{e^{\hbar\omega_k/k_B T} - 1} \tag{7.108}$$

and writing

$$x = \frac{\hbar\omega_k}{k_B T} \tag{7.109}$$

we obtain

$$\sum_k n_k \cong (\frac{1}{4\pi^2})\left(\frac{k_B T}{2JSa^2}\right)^{3/2} \int_0^\infty x^{\frac{1}{2}} \frac{dx}{e^x - 1} \tag{7.110}$$

from which we conclude that the total number of magnons excited at a temperature T is proportional to $T^{3/2}$. This implies that the temperature dependence of the magnetization near $T = 0$ K (where all the spins are aligned in the ferromagnet) also shows a $T^{3/2}$ dependence and this $T^{3/2}$ dependence is verified experimentally.

Spin waves and magnons also are present in antiferromagnetic materials (see Kittel ISSP). Of particular interest is the difference in the magnon dispersion relation between ferromagnets and antiferromagnets. For an antiferromagnet the magnon dispersion relation is found to be (using the same argument as given above)

$$\omega_k = \frac{2|J|S}{\hbar} \sin ka \sim \left(\frac{2|J|S}{\hbar}\right) ka \tag{7.111}$$

so that the initial slope is expected to be finite in contrast to the magnon dispersion relation for ferromagnets, which is given by

$$\omega_k = \frac{4JS}{\hbar}(1 - \cos ka) \sim \left(\frac{2JS}{\hbar}\right) k^2 a^2 \tag{7.112}$$

114

Figure 7.16: Schematic diagram of electronic wave functions showing their anisotropy. Asymmetry of the overlap of electron distributions on neighboring ions [note difference between spin configurations (a) and (b)] is one mechanism for producing magnetocrystalline anisotropy. The spin-orbit interaction changes the orbital charge distribution when the spins are aligned.
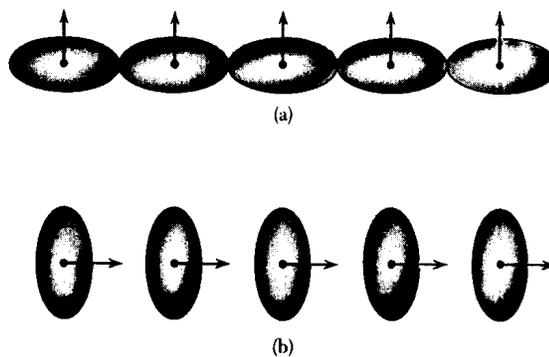
where the initial slope at $k = 0$ vanishes. Experimentally, the magnon dispersion relations for an antiferromagnet are also observed to have zero initial slope

$$\left(\frac{\partial \omega_k}{\partial k}\right)_{k=0} = 0. \tag{7.113}$$

This discrepancy with Eq. 7.111 is attributed to the anisotropy field interaction which is discussed in §7.7.

7.7 Anisotropy Energy

The magnetic moments in a magnetic material tend to line up preferentially along certain crystallographic directions. The exchange energy J_{ij} depends on the orbital overlap of electronic wavefunctions between electronic orbitals on different atomic sites. The spin-orbit interaction couples the orbital motion to the spin direction as indicated schematically in the diagram in Fig. 7.16. This propensity for the spins (or magnetic moments) to line up along specific crystallographic directions is expressed in terms of an anisotropy energy which is written in terms of anisotropy constants K_i and angular factors given in Eq. 7.114 in terms of the direction cosines. For example, for cubic materials the anisotropy energy density U_K is written as

$$U_K = K_1(\alpha_1^2 \alpha_2^2 + \alpha_2^2 \alpha_3^2 + \alpha_3^2 \alpha_1^2) + K_2 \alpha_1^2 \alpha_2^2 \alpha_3^2 + \cdots \tag{7.114}$$

in which α_i represents the direction cosine in the ith direction and K_1, K_2 are the magnetic anisotropy constants having units of energy density. Because of inversion symmetry, we can only have even powers of α_i and the cubic symmetry requires invariance under interchange of any α_i with any α_j. For cubic symmetry, the lowest order term in Eq. 7.114 would go as $\alpha_1^2 + \alpha_2^2 + \alpha_3^2 = 1$ and therefore is a constant independent of crystalline direction, and for this reason can be neglected. This leaves us with higher even powers of the direction cosines as indicated above. The anisotropy constants are temperature dependent and vanish when the Curie temperature is reached and the material goes paramagnetic (see Fig. 7.17). In magnetic device applications, it is necessary to consider both the exchange and anisotropy energies, as is elaborated in §7.8 and in Chapter 8.

115

Figure 7.17: Temperature dependence of the anisotropy constants for single crystal iron. The anisotropy constants are defined in the text.
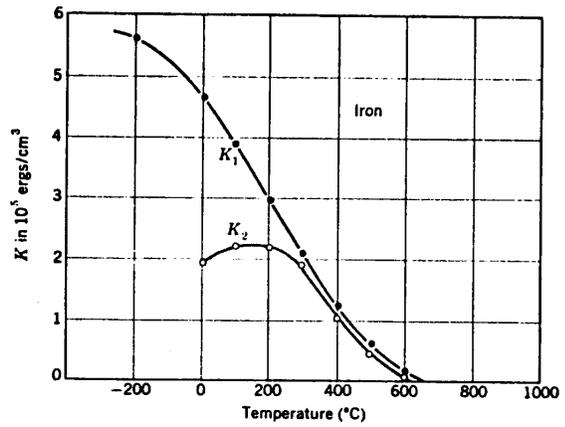
Figure 7.18: Various possible ferromagnetic domain structures in a single crystal of Fe where the preferred direction of magnetization is along (100). Note that in a magnetic field H, the favorably aligned domains grow at the expense of the unfavorable domains.
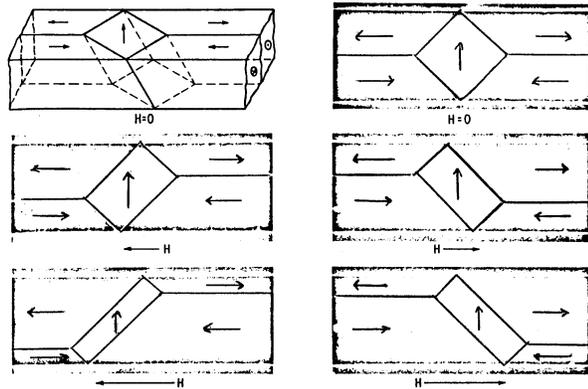
Figure 7.19: Schematic structure for domains in a sample of finite size. To keep magnetic flux within the sample, the domains near the surface will be magnetized parallel to the surface.
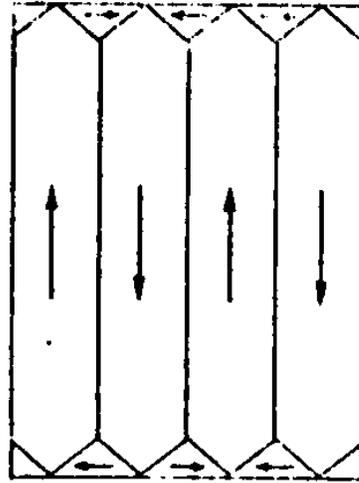
7.8 Magnetic Domains

Macroscopic samples of ferromagnetic materials are not uniformly magnetized, but break up into regions called <u>domains</u>. The magnetization for each domain will, in general, have a different orientation. This happens because of the magnetic dipole interaction between the spins is much weaker than the short-range exchange interaction which aligns neighboring spins. However, over longer distances, the magnetic dipole interaction forces neighboring regions to have opposite magnetization. The anisotropy energy determines the crystallographic direction of the magnetization within a domain, as illustrated in Fig. 7.18 for iron, where the preferred direction is along the (100) axes. When an external magnetic field is applied, the domains having moments along the magnetic field grow at the expense of the domains having moments in other directions, as is shown in Fig. 7.18 for application of a field along (100). The preferred directions for magnetization are called <u>easy axes</u>. Magnetization does sometimes occur along an axis other than an easy axis, and this can happen when domains are formed to keep the magnetic flux within the sample as for example in the end regions of the domain structure shown in Fig. 7.19 where the magnetization is along the x-axis in contrast with the dominant y-axis direction for the magnetization of the domain. We note that with this domain arrangement, the component of the magnetization vector along the domain boundary is continuous across this boundary and therefore there is no magnetic flux leakage outside of the magnetic material. When magnetization occurs along an axis other than the easy axis, a strain energy results and this effect is called <u>magnetostriction</u>. This effect is due to a magnetoelastic coupling between the spins and the lattice. Magnetostriction effects can be used to probe magnetic phase transitions in areas of basic science. The magnetoelastic coupling effect can also be used in signal processing applications.

In real materials, the separation between magnetic domains is gradual and not abrupt (as suggested by Figs. 7.18 and 7.19), and the transition occurs over many atomic planes. The transition region is called a <u>Bloch wall</u> and is shown schematically in Fig. 7.20. Evidence for magnetic domains comes from direct photographs using magnetic powders which tend to

117

Figure 7.20: Schematic structure of a Bloch wall separating magnetic domains. In iron the thickness of the transition region is about 300 lattice constants.
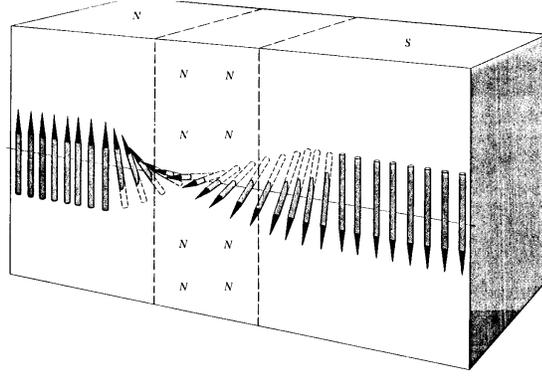
concentrate at the domain boundaries where strong magnetic fields exist (e.g., the proximity of a North and South magnetic pole). This magnetic powder technique was developed by Professor Bitter of MIT, who was also responsible for the basic design of high current magnets which led to the generation of magnetic fields in the 10 tesla (100 kG) range and the establishment of the National Magnet Laboratory Facility.

The size of a domain boundary (Bloch wall) can be estimated on the basis of a simple calculation. From Eq. 7.82 we have the Heisenberg Hamiltonian for a pair of spins

$$\mathcal{H} = -2J\vec{S}_i \cdot \vec{S}_j. \tag{7.115}$$

Assuming a small angle ϕ between spins $\vec{S}_i$ and $\vec{S}_j$ we can apply the Heisenberg Hamiltonian to the Bloch wall to obtain

$$\mathcal{H} = -2JS^2 \cos\phi \simeq -2JS^2\left(1 - \frac{\phi^2}{2}\right) = -2JS^2 + JS^2\phi^2. \tag{7.116}$$

This tells us that the energy is decreased by making ϕ as small as possible. We will denote the exchange energy E_{ex} by $E_{ex} = JS^2\phi^2$ which represents the energy we must supply when we do not line the two spins up perfectly. If we have N spins in a Bloch wall and the total angle of spin rotation is π, then $\phi = \pi/N$ so that the total exchange energy that must be supplied is

$$E_{ex} = NJS^2\pi^2/N^2. \tag{7.117}$$

On the other hand, because of the anisotropy energy, it is unfavorable for spins to be directed along crystalline directions other than the easy axes. Along the Bloch wall most of the spins are not directed along the easy axes, and therefore the anisotropy energy that must be supplied to support a Bloch wall is approximately proportional to the size (length) of the Bloch wall. If K is the anisotropy energy density, then the anisotropy energy per unit area is $(K)(Na)$, where Na is the length of a Bloch wall and a is the lattice constant. We then say that the energy per unit area that must be supplied to maintain a Bloch wall σ_W is

$$\sigma_W = \sigma_{ex} + \sigma_{anis}. \tag{7.118}$$

118

Substitution into Eq. 7.118 then yields:

$$\sigma_W = \left(\frac{JS^2\pi^2}{Na^2}\right) + KNa. \tag{7.119}$$

At equilibrium

$$\frac{\partial \sigma_W}{\partial N} = 0 = -\frac{JS^2\pi^2}{N^2a^2} + Ka \tag{7.120}$$

so that

$$N = \sqrt{\frac{JS^2\pi^2}{Ka^3}} \tag{7.121}$$

and upon substitution of values for J, S, K and a, we find $N \sim 300$ lattice constants for iron.

The equilibrium condition (Eq. 7.120) also gives the energy of the Bloch wall. Using the value of N at equilibrium we obtain for σ_W:

$$\sigma_W = \left(\frac{JS^2\pi^2}{a^2}\right)\sqrt{\frac{Ka^3}{JS^2\pi^2}} + Ka\sqrt{\frac{JS^2\pi^2}{Ka^3}} = 2\sqrt{\frac{KJS^2\pi^2}{a}} \tag{7.122}$$

which for iron is ~ 1 erg/cm^2 which is a very small energy, which tells us that Bloch walls in Fe can be moved easily by an external perturbation. This idea is used in various device applications.

One type of domain that is particularly important for device applications is a small domain formed in thin films of certain ferrimagnetic materials (e.g., orthoferrites such as $Y_3Fe_5O_{12}$) and these domains are called a magnetic bubble. When a magnetic field is applied normal to one of these thin films, it is possible to shrink the size of domains magnetized oppositely to the applied field direction to a size of several microns. These magnetic bubbles can be moved and manipulated with magnetic fields applied in the plane of the film. Because of their small size, they can be used for computer memory applications. Some advantages of magnetic bubbles for such applications involve long term stability of the memory element and durability of the material. Although much research went into computer memory applications for these magnetic bubbles, their application thus far has been limited.

In many commercial applications of ferromagnets, the coercive force is important. The coercive force is defined as the magnetic field $-H_c$ which is required to reduce the magnetization in the material to zero (see Fig. 7.21). For some applications we want H_c to be very small (soft magnetic materials), so that we can easily change the magnetization in the material; such materials for example are needed for transformer core materials. On the other hand, for other applications we need to have materials with a highly stable magnetization and hence a very high coercive force; such materials are used to build high field permanent magnets and are called hard magnetic materials. The magnitude of the coercive force varies over a very wide range – from much less than one gauss to values in excess of 10^4 gauss.

The coercive force is often pictured on a hysteresis diagram which relates the magnetization M to the applied field H. Such a diagram is shown in Fig. 7.21: curve OA gives the evolution of the original magnetization. Upon demagnetization, we reach M_r the remanent magnetization which is present when the external field is reduced to zero. As the external

119

Figure 7.21: Magnetization curve for a
ferromagnet showing a hysteresis loop.
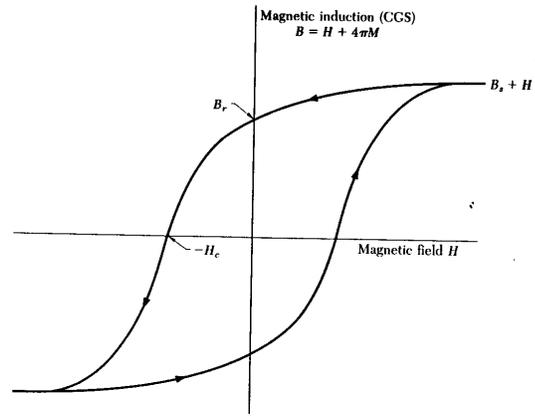
field is applied in the opposite direction, the magnetization is further decreased and eventually vanishes at $-H_c$ (the coercive force). The loop traced out by the magnetization M and applied field H cycle in Fig. 7.21 is called a hysteresis loop and the larger the coercive force, the larger is area enclosed in this loop. Very pure, single crystal, unstrained materials generally have narrow hysteresis loops while impure, small particle or amorphous magnetic materials tend to have wide hysteresis loops.

Chapter 8

Magnetic Devices

References

- E.W. Lee, *Magnetism: An Introductory Survey*, Dover, New York, 1970.

- S. Chikazumi, *Physics of Magnetism*, Wiley, New York 1966.

- R.S. Tebble and D.J. Craik, *Magnetic Materials*, Wiley–Interscience, New York 1969.

- R.J. Gambino, "Optical Storage Disk Technology", Mat. Res. Soc. Bull. **15**, 20 (1990).

- J.A.M. Greidanus and W. Bas Zeper, "Magneto-optical Storage Materials", Mat. Res. Soc. Bull. **15**, 31, (1990).

8.1   Introduction

In this chapter we briefly survey a number of magnetic devices. Many people are aware of the huge magnitude of the semiconductor industry. Far fewer people are aware of the fact that the magnetic device business is about 2/3 of the size of the semiconductor business. Therefore a brief review of some common magnetic and magneto–optic devices is in order.

8.2   Permanent Magnets

Permanent magnetic fields having strengths of the order of 10 kilogauss can be obtained using the remanent magnetization of so-called "hard" magnetic materials. These are characterized by (1) large permeabilities and (2) high coercive fields (H_c). Important to the development of radar as components in magnetron microwave amplifier tubes, the most widespread modern applications are small motors and loudspeakers. Alloys of aluminum, nickel and cobalt (Alnico) and other more recent cobalt alloys are in common use. In the last few years a new NdFeB ($Nd_2Fe_{14}B$ alloys) compound has been developed with a very high BH product.
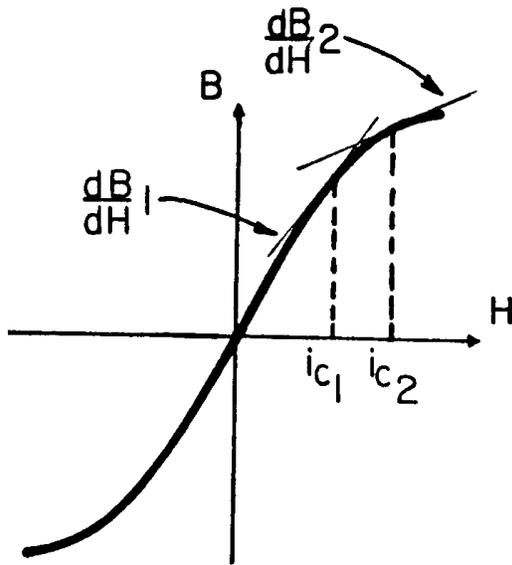
Figure 8.1: Slopes of the $B - H$ curve that is exploited in designing a magnetic amplifier.

8.3 Transformers

Reference:

- Magnetic Circuits and Transformers, M.I.T. Press, Cambridge, 1943

Transformers consist of two or more coils linked by a magnetic flux path in which the driving (or primary) coil induces currents in the driven (or secondary) coils. The important features of the material used to couple the coils magnetically are (1) large permeabilities for efficient coupling through minimization of "leakage" flux, (2) very small coercive fields H_c, and (3) linear magnetization curves having little hysteresis. Hysteresis causes both distortion and power loss. Large permeabilities and small H_c define "soft" magnetic materials. Pure iron is a good example of a soft magnetic material, especially when used in multi-layer or laminated construction in which the cross-section normal to the flux direction is composed of insulated stacks of thin plates. This construction prevents large induced circulating currents in the iron ("eddy" currents) and their attendant losses due to Joule heating.

8.3.1 Magnetic Amplifiers

Reference:

- H.F. Storm, Magnetic Amplifiers, John Wiley, NY, 1955

A transformer with a non-linear B-H curve may be used as a signal multiplier or magnetic amplifier if an additional coil, the control winding, is used to change the differential permeability at which the device is operating. In the diagram of Fig. 8.1, the local slope of the B-H curve is a function of the control current, i_c. The transfer characteristics of the

device will have the input and output currents related by

$$i_{out} \propto \left(\frac{dB}{dH}\right) i_{in} \tag{8.1}$$

and if

$$\frac{dB}{dH} = f(i_c) \approx f_0 i_c \tag{8.2}$$

so that the function $f(i_c)$ is linear in i_c, then

$$i_{out} \approx (f_0 i_{in}) i_c \tag{8.3}$$

where i_{out} is proportional to i_c and the product $(f_c i_{in})$ may represent a large gain factor.

8.4 Data Storage

8.4.1 Magnetic Core

Reference:

- T.C. Chen and A. Papoulis, *Domain Theory in Core Switching*, Proc. IRE, 1958, Vol 46, pp. 839–849.

Remanent magnetism may be used to provide a fast, reliable electrical recording technique. For digital storage materials, (1) large permeabilities, and (2) intermediate but well-controlled coercive fields are desirable. In particular, toroidal-shaped elements called cores in which the magnetization is circumferentially directed became the main stay of computer mass memory (although continuing advances in semiconductor technology have made this form of memory largely obsolete). A typical B-H curve for a core is given in Fig. 8.2. In practice, the cores are threaded in a matrix of wires, as shown below. Data is entered ("written") into the array by applying a current i to each of the horizontal and vertical wires called address lines. The magnitude of i is such that its H-field is insufficient to cause a change in the magnetization of a core, but the coincidence of currents from two wires at a single core is sufficient to magnetize it. With the current returned to zero, the magnetization is at position (1) on the $B - H$ curve. To reverse the magnetization ("erase" the core), a coincidence of currents - i are applied to the core, leaving the remanent magnetization at position (2) on the curve in Fig. 8.2. To determine ("read") the state of the core, a pair of currents i are addressed to the core; if the previous state of the core was (2), there will be a sudden change in the core magnetization, which will induce a current in the third wire threading the cores (see Fig. 8.3), the output or "sense" wire. This current is then amplified to usable levels. If the core had been in state (1), there would be no magnetization change, and hence no "sense" current. Note that a "read" operation destroys the original state of the core, so that it must be "rewritten" if it is needed in subsequent operations.

8.4.2 Data Storage: Magnetic Tape

Reference:

- H.G.M. Spratt, Magnetic Tape Recording, Temple Press Books, London, 1964
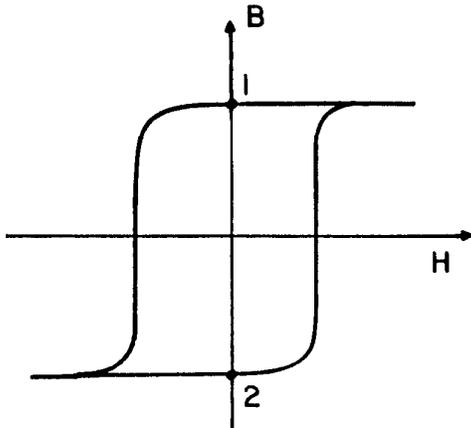
Figure 8.2: $B - H$ curve with a nearly rectangular hysteresis loop.

Figure 8.3: Schematic diagram of a magnetic core memory, showing the address wires on the x and y axes, and the "sense" wire threading the cores.

124
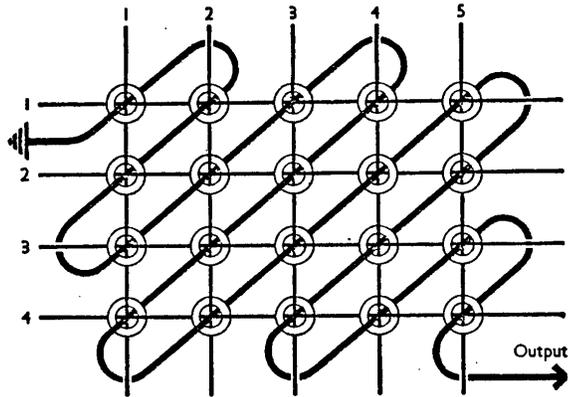
Figure 8.4: θ the angle between $\vec{H}_0$ and $\vec{H}_a$
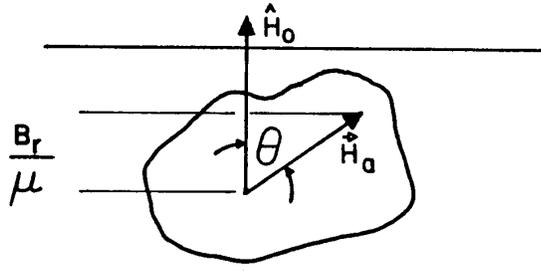
Magnetic tape is a continuous strip of flexible dielectric (such as mylar plastic) to which is bonded a thin layer of magnetic particles dispersed in an insulating base. The particles have

1. large permeability,

2. intermediate coercive field values, and

3. large anisotropy.

The anisotropy of the particles determines the direction of their remanent magnetization. That is, for large applied fields ($H_0 \gg H_a$) normal to the tape, the normal component of the remanent magnetization is

$$B_r = \hat{\mu}\hat{H}_0 \cdot \vec{H}_a = \pm\hat{\mu}|H_a|\cos\theta \qquad (8.4)$$

where $\hat{\mu}$ is the particle permeability, $\vec{H}_a$ its anisotropy field, and θ the angle between the applied field $\vec{H}_0$ and the anisotropy field $\vec{H}_a$, as in Fig. 8.4. This means that only the sign of the particle magnetization may be changed. The external magnetization of the tape will be an average over all possible θ, with the additional complication of variation in the shapes of the particles causing variations in their external fields. A typical $B_r - H$ curve for a magnetic tape is shown in Fig. 8.5, where B_r is the remanent induction of the tape after the removal of the field H. If the field H_0 applied by an electromagnet (the recording head) changes with time, and the tape is simultaneously translated along its length ℓ, then

$$B_r(\ell) = f[H_0(t)] \qquad (8.5)$$

and the recorded $B_r(\ell)$ can be subsequently detected by moving it under another coil (the playback head). For faithful reproduction we would like

$$f[H_0(t)] = f_0 H_0(t) \qquad (8.6)$$

which, from the shape of the $B_r - H$ curve, will clearly not be the case. A clever trick is used in nearly all modern audio recording to overcome this problem. The signal $H_0(t)$ is added to a high frequency ($\sim 100kHz$) bias field $H_B(t)$ which has sufficient magnitude to span the non-linear region in the $B_r - H$ curve as shown in Fig. 8.6 The remanent induction $\langle B_r(\ell) \rangle$ averaged over several cycles of the bias field will then be approximately

$$\langle B_r(\ell) \rangle \approx f_0 H_0(t) \qquad (8.7)$$

where f_0 is the local slope of the effective recording characteristic.

Figure 8.5: Typical $B_r - H$ curve for a magnetic tape.
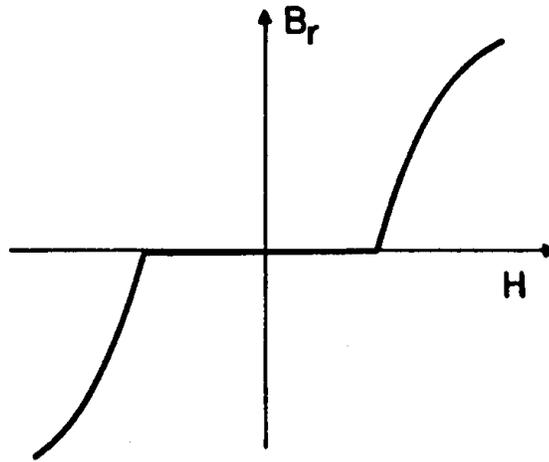
Figure 8.6: Use of bias field to improve recording fidelity for magnetic storage tape.
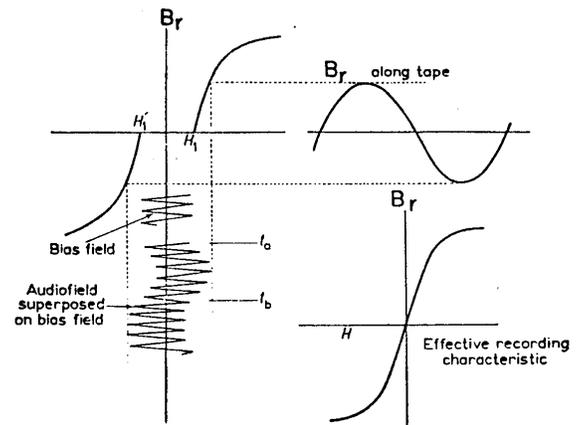
Figure 8.7: Geometry of a magnetic bubble film.

126
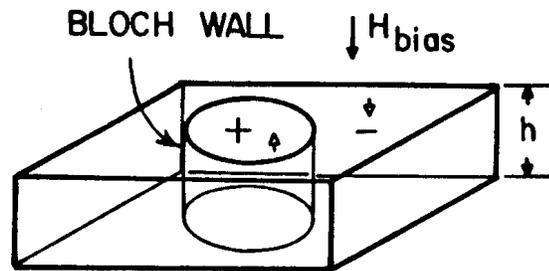
Figure 8.8: Schematic of TI bar structure used to propagate magnetic bubbles.
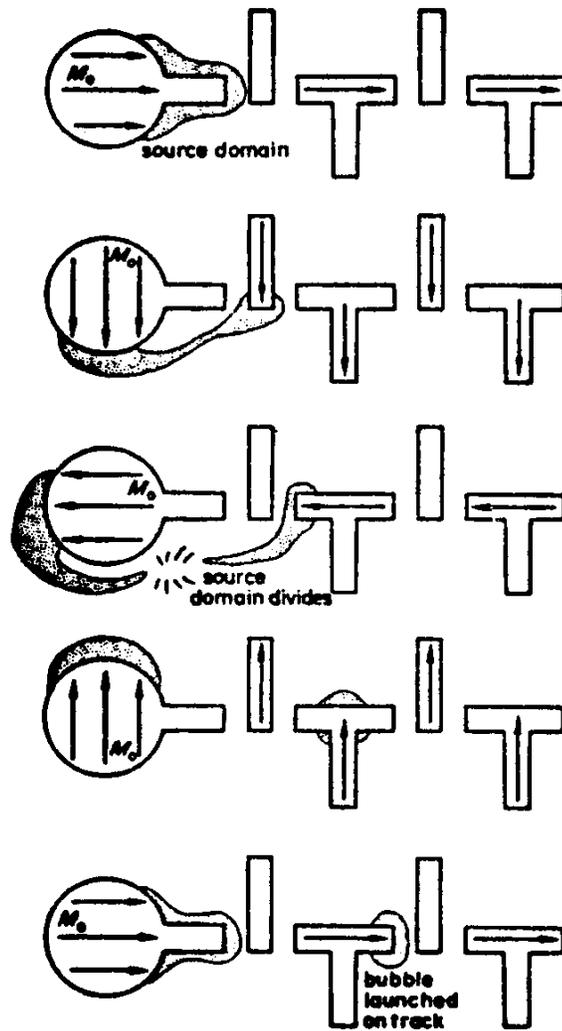
8.4.3 Magnetic Bubbles

References:

- T.H. O'Dell, **Magnetic Bubbles**, John Wiley, NY, 1974

- H. Chang, Ed.,**Magnetic Bubble Technology: Integrated-Circuit Magnetics for Digital Storage and Processing**, I.E.E.E. Press, 1976.

One interesting development in magnetic memory devices is that of magnetic bubble technology. Small ($\sim$ 1 micron diameter) circular domains in thin magnetic films can be generated, so that the magnetization of these domains is normal to the plane of the film and opposite to that of the surrounding material as shown in Fig. 8.7. The film material, usually one of the many insulating magnetic garnets, is arranged to have its easy magnetic

Figure 8.9: Schematic diagrams of (a) bubble (b) flux lines (c) forces for magnetic bubble recording media.
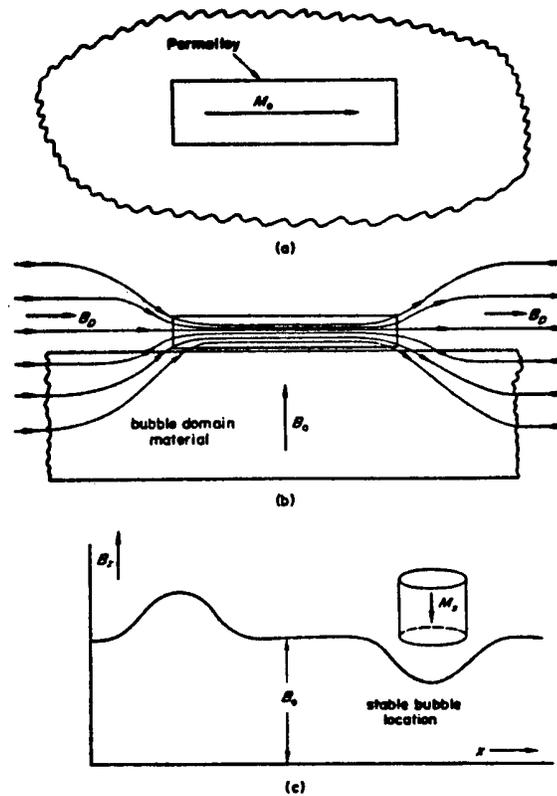
axis normal to the plane. Magnetic materials used for magnetic bubble memories should have

1. high uniaxial anisotropy energy in order to maintain the simple domain structure shown in Fig. 8.7;

2. low saturation fields, so that domains may be created with practical applied fields;

3. low value for H_c, so that the domains may be propagated with reasonably small field gradients, and

4. high domain wall mobility, allowing high propagation velocities and hence high data rates.

Bubbles may be created by sudden changes in the bias field of uniformly magnetized material. Hydrodynamic instabilities prevent the film magnetization from changing instantaneously, and domains form analogously to the formation of fluid droplets due to surface-tension. Once formed, a bubble domain may be stably located by placing it in an in-plane field gradient, induced, perhaps, by the presence of an overlying "soft" magnetic structure of high permeability, such as rectangular layers of permalloy (80% nickel/20% iron alloy) (see Fig. 8.9a). The high permeability layer concentrates the flux of the in-plane B-field (see Fig. 8.9b), yielding a magnetic well at one end of the bar which can stabilize

128

Table 8.1: Properties of bubble film materials.

MATERIAL	$h, (\mu m)$	$\hat{\mu}_0 M$, (T)	$\hat{\mu}_w$,(m/s) per T	τ^*,(ns)
$Gd_{2.3}Tb_{0.7}Fe_5O_{12}$	12.5	0.0142	1.08×10^4	82
$Y_{2.4}Eu_{0.6}Ga_{1.1}Fe_{3.9}O_{12}$	10.8	0.0210	$\approx 10^4$	≈ 50
$DyFeO_3$	42	0.0128	3.3×10^4	100
$Sm_{0.55}Tb_{0.45}FeO_3$	50.0	0.0126	9.0×10^4	44
$EuEr_2Ga_{0.7}Fe_{4.3}O_{12}$	5.7	0.0250	0.96×10^4	24

a bubble, as shown in Fig. 8.9c. If the field well can be moved, the bubble will follow. A simple scheme for accomplishing this is the so-called TI bar structure shown in Fig. 8.8. An in-plane magnetic drive induction B_D is applied which rotates in the plane at a constant angular frequency. The demagnetization effect of the permalloy bars is largest when they are parallel to B_D, so that the field well minimum will always lie at the ends of the bar sections which have the longest cross sections in the direction of the applied field. As the direction of B_D rotates, the field minima will propagate down the array carrying bubbles with them. Figure 8.8 shows four intermediate steps in this process, and demonstrates how bubbles are "copied" from a large source domain. The "copy" process can be inhibited by an in-plane field, applied by a current loop at the "neck" of the source domain. In this way, a serial pattern of bubbles and vacancies can be propagated down the array, forming a digital shift register. The bubbles may be detected by a sense coil in a manner similar to that of magnetic tape playback.

The speed of propagation is limited by the domain wall mobility, μ_w, which is related to v_b, the bubble velocity, by the magnetic drive induction B_D by

$$v_b = \mu_w B_D. \tag{8.8}$$

The properties of a number of possible bubble domain materials are listed in Table 8.1. Given are the film thickness h in microns, the saturation magnetization $\mu_0 M$ in tesla (1 tesla = 10^4 gauss), the wall mobility μ_w, and a time constant τ^* which characterizes the effective inertial response of bubbles in these materials.

$$\tau^* = \frac{h}{\mu_w \mu_0 M} \tag{8.9}$$

8.4.4　Magneto-optical Storage

Reference:

- Iwamura et al., *Electronic Letters* **15**, 830 (1979).

Magneto–optical storage of digital information exploits the optical properties of magnetic materials, in particular, their magneto–optical Kerr rotation and Faraday rotation. The media used is a thin magnetic film with the following characteristics:

Figure 8.10: Principle of magneto–optical read–out. The direction of the magnetization is detected by the rotation of a plane–polarized light wave upon reflection.
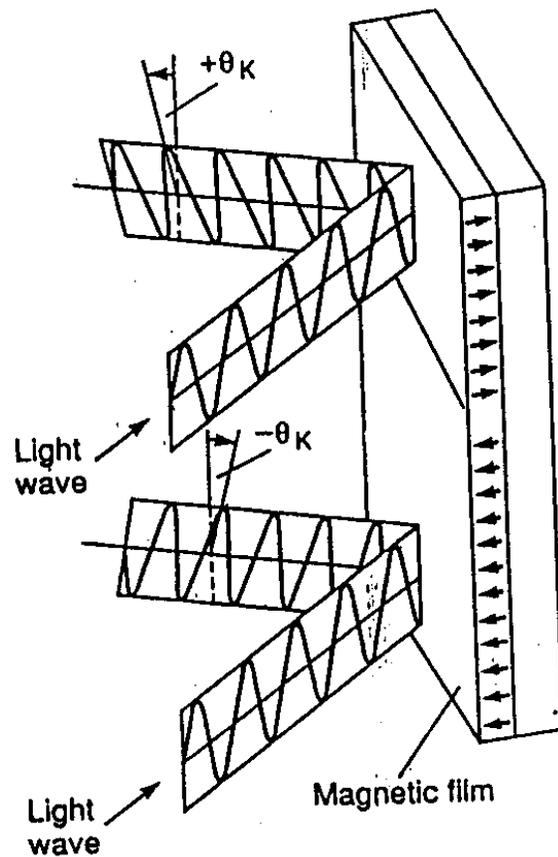
1. Large uniaxial anisotropy to insure that the magnetization is directed normal to the plane of the film;

2. A high room temperature coercive field to insure stable magnetic domains;

3. A rectangular hysteresis loop; and

4. Small grain (crystalline) size for regularly–shaped magnetic domains.

Data is stored on the magnetic film as circular domains approximately 1μm in diameter. The magnetization of a domain is either up or down with respect to the film, indicating a 0 or 1 bit. A bit is *read* (see Fig. 8.10) by examining the polarization of laser light reflected from such a domain. Polarized light will suffer a positive or negative Kerr rotation upon reflection, depending on whether the magnetization of the domain is up or down.

To *write* a bit of information, a magnetic field (see Fig. 8.11) is applied to the film in the desired direction. Focused laser light then raises the temperature of the domain to be written, causing the coercive field, $H_c(T)$, to drop to a value at which the applied field is strong enough to switch the magnetization of the domain. Note that the coercive field of the material at room temperature $H_c(T_{RT})$ is large enough, and the hysteresis loop rectangular enough so that all other domains are unaffected by the applied magnetic field.

130

Figure 8.11: Principle of the thermo-magnetic writing process. (a) A laser generates a temperature profile $T(x)$ in the perpendicularly magnetized layer M; consequently, the coercive field H_c decreases with temperature T as in (b). When a magnetic field of suitable magnitude is now applied, the magnetization direction will be reversed for this domain, while all other domains have a sufficiently high coercive field to maintain their direction of magnetization.
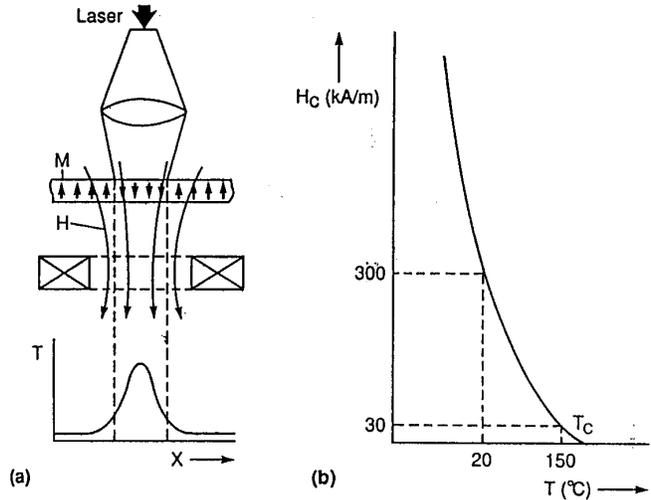
Using a similar principle, an optical circulator can be built (see Fig. 8.12). Shown in this figure is an optical circulator used in fiber–optic communication links which has the virtue of being unaffected by the polarization of the input light. Unpolarized light enters port 1 and is split by a polarization beam splitter into two orthogonally polarized beams. Referring to Fig. 8.12, rotator 1 is a Faraday rotator which rotates polarizations by $+45°$. Rotator 2 is birefringent rotator which also rotates the polarization by $+45°$ giving a total rotation of $90°$ to the polarized beams. This allows unpolarized light to exit at port 2 after being recombined at the second polarization beam splitter.

Unpolarized light entering port 2 will also be split into two orthogonal polarizations. But, the birefringent rotator (2) will rotate the polarizations by $–45°$. This gives a net rotation of $0°$ to the two beams allowing light to exit at port 3 rather than port 1. In this way, signals can be sent and received simultaneously along the same optical fiber.

8.5 Faraday Effect

Reference:

- R.E. Collins, *Foundations for Microwave Engineering*, McGraw–Hill, NY (1966).

The Faraday effect results from the presence of two different propagation constants β_+ and β_- for right– and left–circularly polarized radiation, respectively, in response to a magnetic field applied along the axis of propagation of the electromagnetic wave. This is equivalent to a rotation of the linear polarization about the $z-$axis (or propagation axis) with θ_ℓ, the angular rotation per unit length of propagation given by

$$\theta_\ell = (\beta_- - \beta_+)/2 \tag{8.10}$$

the evolution of the rotation angle is shown in Fig. 8.13 as the electromagnetic wave propagates through the medium. Note that the Faraday effect is non–reciprocal in the sense that

131
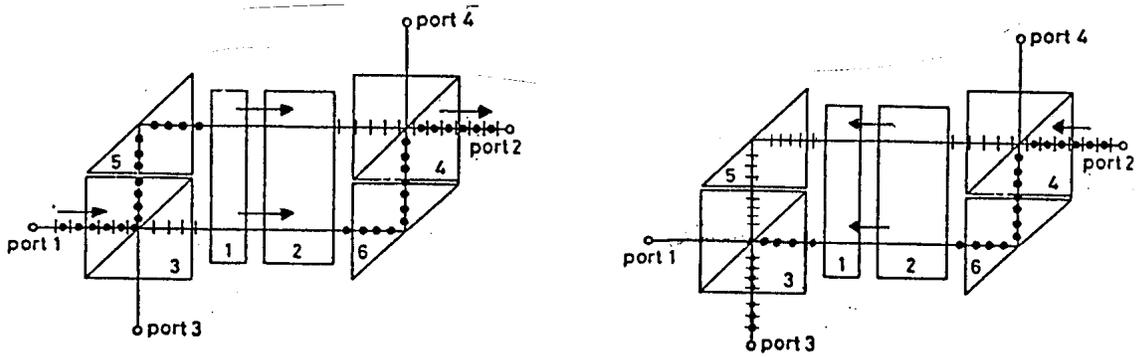
Figure 8.12: Polarization–independent optical circulator. Device #1 denotes a 45° YIG (Faraday) rotator, while device #2 denotes a 45° quartz (birefringent) rotator. Devices #3 and #4 denote polarization beam–splitting cubes and devices #5 and #6 denote right–angle prisms. The circulation scheme is Port 1 → Port 2; Port 2 → Port 3; Port 3 → Port 4; Port 4 → Port 1.

Figure 8.13: Angles defining rotation for the Faraday effect.
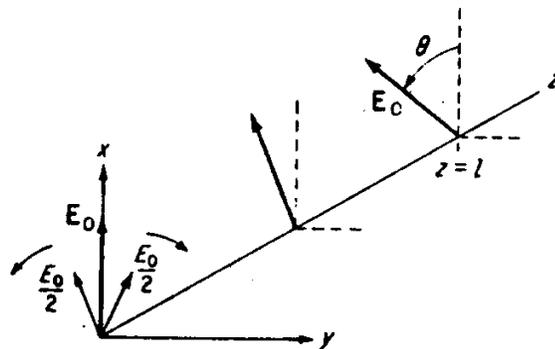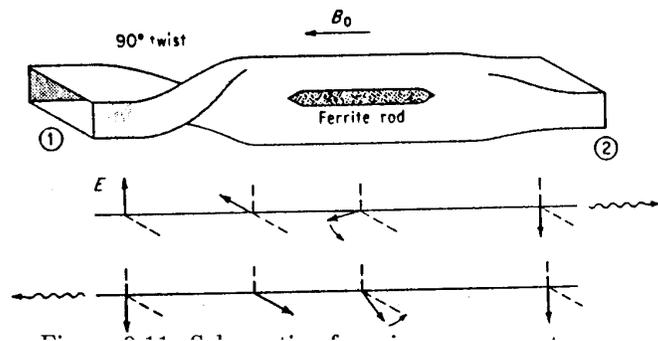
Figure 8.14: Schematic of a microwave gyrator
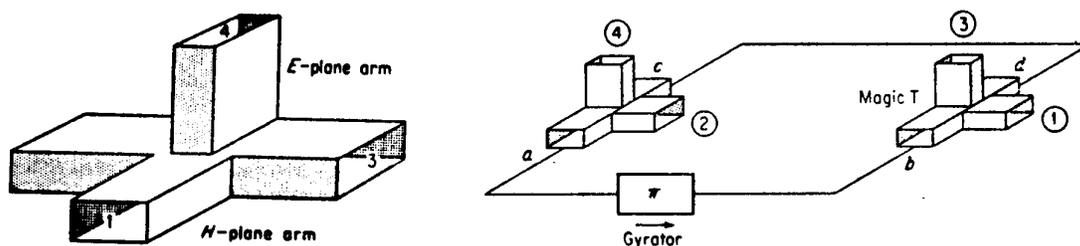
Figure 8.15: (a) A "magic T" microwave device (see text) (b) A four–port circulator consisting of a gyrator and two "magic T"s.

a wave passing through a thickness of material ℓ, then reflected, and returning through the thickness ℓ, would suffer successive rotations of the plane of polarization

$$\theta = \theta_\ell(2\ell) = (\beta_- - \beta_+)\ell \tag{8.11}$$

rather than being returned to its initial polarization state, $\theta = 0$. A number of different devices utilize this effect, including certain types of gyrators, circulators and isolators.

A gyrator (in microwave technology) is defined as a two–port device that has a relative difference in phase shift of 180° for transmission from port 1 to port 2 as compared with the phase shift from port 2 to port 1 (see Fig. 8.14). Going from $1 \rightarrow 2$ the polarization rotations of the 90° twist and the 90° rotation of the ferrite rod add, giving a total phase shift of 180°. However, going from $2 \rightarrow 1$, they cancel, for a net shift of 0° (see Fig. 8.14). The chief use of gyrators is as components in the construction of microwave circulators.

A circulator is a multiport device having the property that a wave incident in port 1 is coupled into port 2 only, port 2 is coupled only into port 3, etc. A four–port circulator is shown in Fig. 8.15b, fabricated from a gyrator and two so–called "magic T" junctions (see Fig. 8.15a). A magic–T microwave junction utilizes the E–field orthogonality of the TE_{10} waveguide modes of different orientations, together with proper wave impedance matching

elements, to effect the following coupling situation (see Eq. 8.12):

$$
\begin{pmatrix} A_{1o} \\ A_{2o} \\ A_{3o} \\ A_{4o} \end{pmatrix} = \frac{\sqrt{2}}{2} \begin{pmatrix} 0 & 1 & 1 & 0 \\ 1 & 0 & 0 & 1 \\ 1 & 0 & 0 & -1 \\ 0 & 1 & -1 & 0 \end{pmatrix} \begin{pmatrix} A_{1i} \\ A_{2i} \\ A_{3i} \\ A_{4i} \end{pmatrix}
\tag{8.12}
$$

The $A_{n,0}$ are the outgoing wave amplitudes at ports $n = 1, 2, 3, 4$ and the $A_{n,i}$ are the corresponding incoming amplitudes. The matrix denotes which linear combination of input amplitudes contribute to each output amplitude. For example

$$
A_{10} = \frac{1}{\sqrt{2}} \left(A_{2i} + A_{3i} \right)
\tag{8.13}
$$

or ports 2 and 3 couple to port 1 in phase, and

$$
A_{40} = \frac{1}{\sqrt{2}} \left(A_{2i} - A_{3i} \right)
\tag{8.14}
$$

ports 2 and 3 couple to port 4 out of phase.

A wave entering (1) is split into two in–phase components which add constructively and are coupled out through port (2). An input at (2) is split likewise, but one are is shifted $180°$ in this direction by the gyrator so that the sum interferes destructively for port (1) but constructively for port (3). Similarly, port (3) is coupled to (4), and (4) to (1). (For details of the properties of "magic–T's," (see Collins Ref., p. 282).

Non–reciprocal rotations of $45°$ can be used to build isolators, which have low loss in one direction, and very high loss in the other. Such devices are used to protect microwave equipment from damage due to power reflected from mis–matched antennas.

We illustrate here also a device application at optical frequencies. High–power pulse laser systems (as is used for laser fusion and isotope separation) are currently built in separate stages, starting with an oscillator and followed by subsequent amplifier stages. This is done so that each laser amplifier stage can be optimized for the power levels it must handle. An amplifier stimulated by extraneous radiation can be driven to catastrophic oscillation and destruction. Hence it is critically important that an amplifier be isolated from light generated or reflected by subsequent stages.

This can be done as shown in Fig. 8.16. The laser beam is plane–polarized at $45°$ to the vertical, and passes unattenuated through a polarization analyzer which is oriented at the same angle. The beam then goes through a $45°$ Faraday rotator, is brought to vertical polarization, and excites the next stage. Any reflected or regenerated light passes through the rotator again and is shifted by a further $45°$. The resulting polarization is orthogonal to the analyzer, and is therefore blocked.

8.6 Magnetic Multilayer Structures

8.6.1 Introduction

Magnetic multilayers are usually made of alternating layers of magnetic and non-magnetic species, with the non-magnetic substance referred to as the spacer. The layer thickness for both spacer and magnetic species roughly ranges from a few angstroms to a few hundred
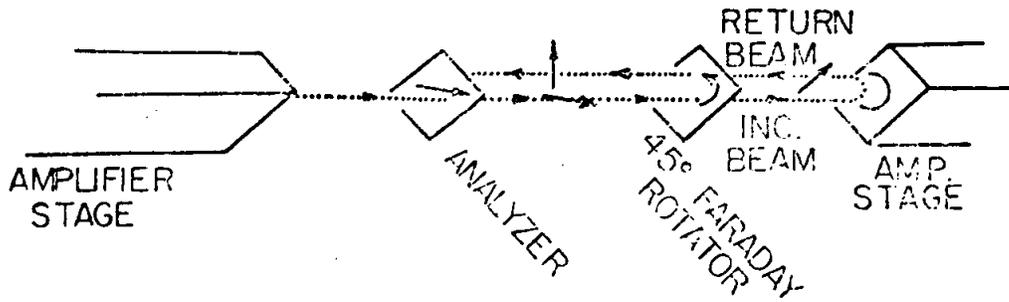
Figure 8.16: Schematic of an optical isolator.

angstroms. Due to the small dimension in the z-direction we may regard the research on magnetic multilayers as a subset of studies on thin films.

The physical phenomena to be studied include magneto-optics, magnetoresistance, magnetostriction, magnetostatics, magnetic exchange coupling, microwave properties and anisotropy at magnetic surfaces and interfaces. Not all these properties will show up in a single magnetic multilayer structure, which leads to the classifications of magnetic multilayers according to their different characteristics. One of these distinguishing characteristics is the electrical conductivity, i.e. magnetic multilayers can be divided into metallic magnetic multilayers and insulating magnetic multilayers. This choice of division is not arbitrary because magnetism is an electronically driven phenomenon, so that it is closely related to electrical conductivity.

8.6.2 Metallic Magnetic Multilayers

In this category, the most commonly used ferromagnets are Fe, Co, Ni, Ni-Fe, Fe-Co, Dy, Er, Gd, Ho and Tm. The most commonly used spacers are Cu, Ag, Au, Mg, Sn, V, Nb, Ta, Cr, Mo, W, Mn, Pd, Y and Lu. Notice that we have used the word *ferromagnets* to describe magnetic components of metallic magnetic multilayers. That is because most conducting magnetic materials are ferromagnets and most insulating magnetic materials are antiferromagnets.

Metallic magnetic multilayers exhibit two interesting properties: **oscillating interlayer coupling** and **giant magnetoresistance**[1]. Research demonstrating those two effects has focused on Fe, Co, and Ni separated by Cr, Ru, Re, Cu and Ag.

Interlayer Coupling

Adjacent ferromagnetic layers, which are separated by a non-magnetic metal spacer, have their magnetization vectors either parallel (ferromagnetic coupling) or antiparallel (antiferromagnetic coupling) to each other (see Fig. 8.17). Shown in Fig. 8.17 is a magnetic configuration whereby the magnetization vector lies in the plane of the layers, and the oscillation in the interlayer coupling is a function of spacer thickness. Typical oscillation periods reported in the literature are: $P_{Cu}= 10$ Å, $P_{Ru}= 11$ Å, and $P_{Cr}=18\text{-}20$ Å[2]. Furthermore, the experimental results also show that for sharp magnetic/spacer interfaces (MBE grown superlattices) the oscillation period is about two atomic layers, approximately three

Figure 8.17: Schematic representation of a magnetic metallic multilayer. (a) Successive magnetic layers are arranged with their magnetizations antiparallel. In this arrangement the electrical resistance of the film is high. (b) Parallel magnetization configuration results from applying a magnetic field to the magnetic arrangement in (a). The new arrangement has a lower electrical resistance. The film thus exhibits a negative magnetoresistance.
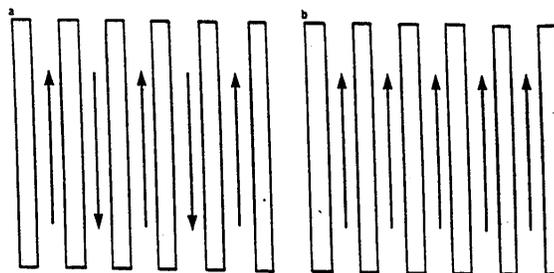
Figure 8.18: Magnetoresistance of a GaAs[Fe(30 Å)/Cr(9 Å)]$_{60}$ multilayer at 4.2 K. The current voltage drop and magnetic field are all in the plane of the layers.
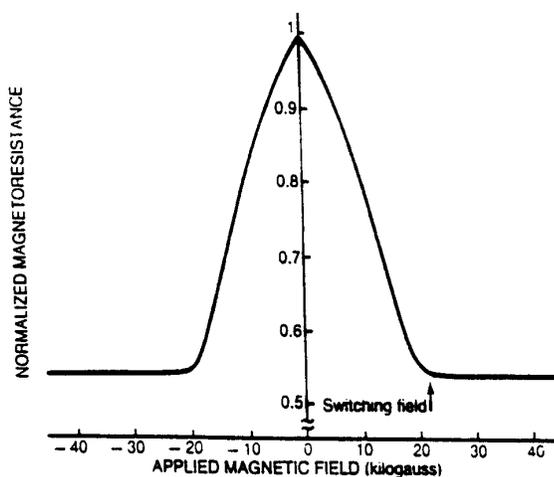
angstroms[3]. For all spacer materials, the oscillation (i.e., interlayer coupling) ceases to exist when the thickness of the spacer exceeds 50 Å[3,4]. Although the coupling mechanism is not completely understood yet, theoretical calculations based on different models such as the RKKY mechanism, Fermi surface nesting, and quantum-size effect give good fits to the experimental data[5,6].

Giant Magnetoresistance (GMR)

The giant magnetoresistance effect shows up in samples in which the magnetic alignment is antiparallel. As the external magnetic field is gradually increased from zero gauss, the magnetic moments of different layers tend to line up with the field. At the same time the electrical resistivity decreases (see Fig. 8.18). This negative magnetoresistance can be as large as 65% in samples that exhibit an initial resistance within a range useful for

practical applications. The resistivity of metallic magnetic multilayers can be calculated by solving the Boltzmann transport equation with spin-dependent scattering at the interfaces. Calculations show in general the scattering is weaker and less effective when the arrangement between successive ferromagnetic layers is parallel[7].

8.6.3   Insulating Magnetic Multilayers

As the name implies, the fundamental difference between metallic magnetic multilayers and insulating magnetic multilayers is their electrical resistivities. Different electrical conductivities lead to different kinds of magnetism. The magnetism of conducting magnetic materials can be described by the itinerant electron theory, whereas the magnetism of non-conducting magnetic materials can be better described by the local moment theory, i.e., mean-field theory. Therefore, it is intuitively simpler to consider interlayer couplings and general magnetic properties of insulating magnetic multilayers. Incidentally, magnets with localized moments are also called Heisenberg magnets.

Insulating magnetic multilayer structures that have been considered so far are FeF_2/CoF_2, $MnTe/ZnTe$, Fe_3O_4/NiO, CoO/NiO and $EuTe/PbTe$.

FeF_2/CoF_2 and CoO/NiO belong to the same family of magnetic multilayers that consist of two antiferromagnetic materials. Studies show that, while the superlattices retain the antiferromagnetic spin order of the constituents, the magnetic behavior near the phase transition reflects the influence of one material on the other[8,9]. Specifically, measurements of the spatially modulated order parameter in a 72 Å period sample [NiO(43 Å)/CoO(29 Å)] suggest that the Ni and Co moments order at separate temperatures shifted from the T_N's for bulk CoO and NiO (291 and 520 K respectively). In contrast, magnetic order develops simultaneously within the CoO and NiO layers, for two superlattices with 36 Å periods. The measured transition temperatures fall between the Neel temperatures for bulk CoO and NiO depending on the relative CoO and NiO layer thicknesses.

There is an ongoing study on the magnetic properties of EuTe/PbTe at Prof. M.S. Dresselhaus group at M.I.T. EuTe is an antiferromagnetic insulator and PbTe is a nonmagnetic semiconductor. The lack of free carriers in the spacer, PbTe, effectively rules out the possibility for successive EuTe layers interacting through PbTe by a RKKY-like mechanism. Thus EuTe/PbTe is truly a Heisenberg multilayer structure of the simplest kind. The magnetization results on EuTe/PbTe superlattices (SL) show that T_c has remained essentially the same as that of the bulk even when the thickness of EuTe is reduced to 3 atomic monolayers. EuTe is a type II antiferromagnet which has ferromagnetically ordered (111) planes and adjacent (111) planes are antiferromagnetically aligned (see Fig. 8.19). Thus, intuitively one would expect that a multilayer structure made of repeated periods with *three* or *five* (111) planes in one period would show a ferrimagnetic phase transition, whereas a multilayer structure with *four* (111) planes in one period would show an antiferromagnetic phase transition. This difference is observed in short-period EuTe/PbTe SLs (see Fig. 8.20).

8.6.4   References

1. For an introductory overview on metallic magnetic multilayers see L.M. Falicov, Metallic Magnetic Superlattices, PHYSICS TODAY 1992, Vol 45, Issue 10, pp 46-51.

2. S.S.P. Partin, Phys. Rev. Lett. **67**, 3598 (1991)
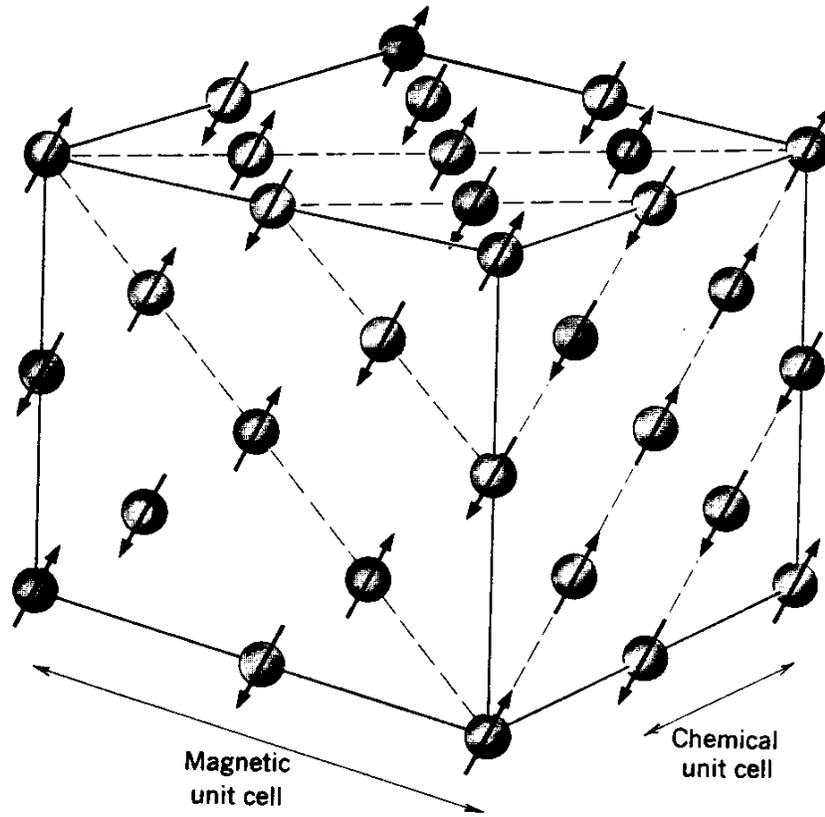
Figure 8.19: The EuTe structure showing both the chemical unit cell and the magnetic unit cell.
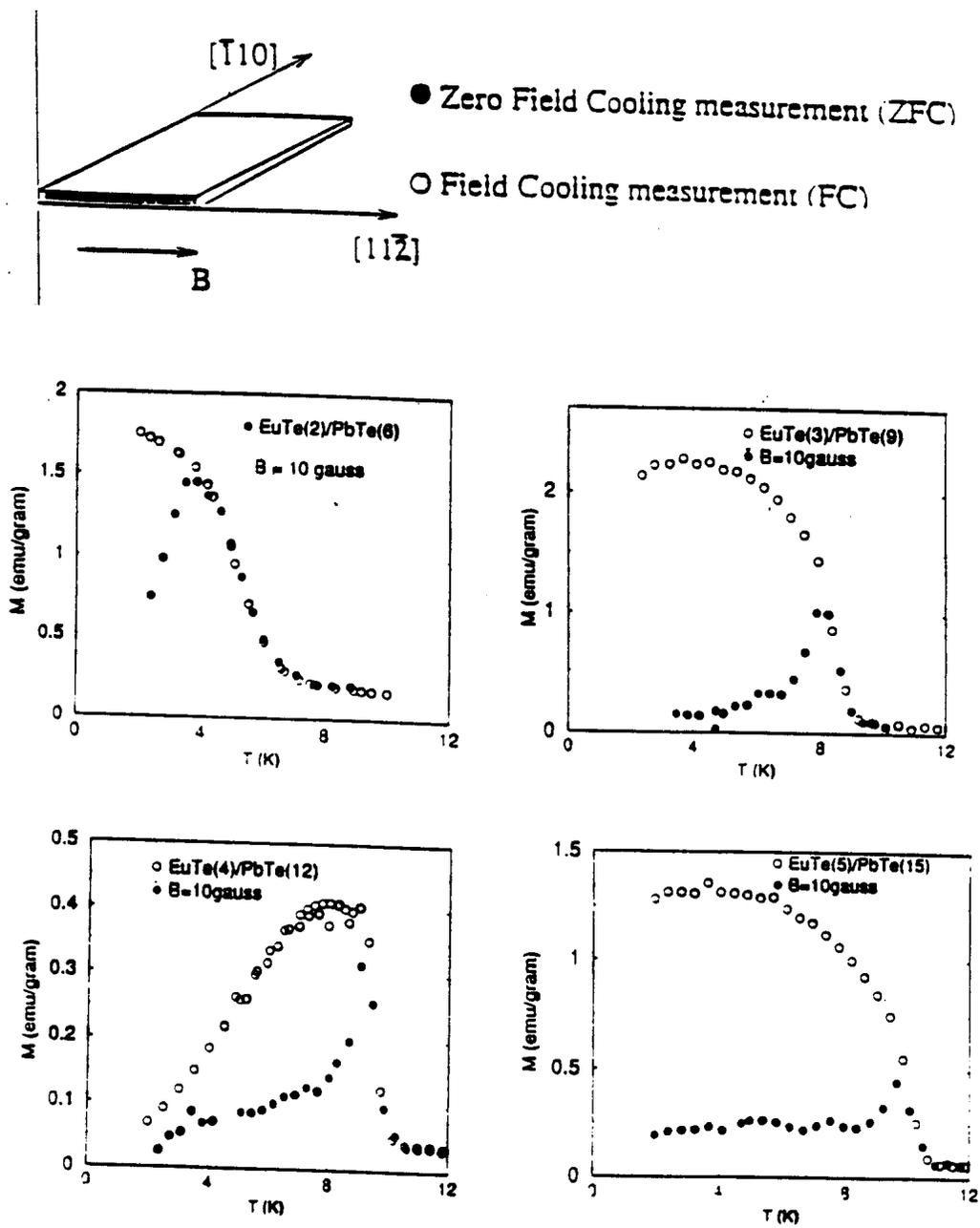
Figure 8.20: Magnetization curves for various EuTe/PbTe superlattices.

3. J. Unquris, *et al.*, Phys. Rev. Lett. **67**, 140 (1991)

4. T. Giebultowicz *et al.*, private communication.

5. Y. Wang *et al.*, Phys. Rev. Lett. **65**, 2732 (1992)

6. M.C. Munoz *et al.*, Phys. Rev. Lett. **72**, 2482 (1994)

7. R.E. Camely *et al.*, Phys. Rev. Lett. **63**, 664 (1989)

8. C.A. Ramos *et al.*, Phys. Rev. Lett. **65**, 2913 (1990)

9. J.A. Borchers *et al.*, Phys. Rev. Lett. **70**, 1878 (1993)